2019

Thermally stable, efficient, vapor-deposited inorganic perovskite solar cells

Harshavardhan Ashok Gaonkar
Iowa State University

Thermally stable, efficient, vapor-deposited inorganic perovskite solar cells
by

Harshavardhan Ashok Gaonkar

A dissertation submitted to the graduate faculty

in partial fulfillment of the requirements for the degree of

DOCTOR OF PHILOSOPHY

Major: Electrical Engineering (Microelectronics and Photonics)

Program of Study Committee:
Vikram L. Dalal, Major Professor
Rana Biswas
Ruth Shinar
Jaeyoun Kim
Mani Mina

The student author, whose presentation of the scholarship herein was approved by the program of study committee, is solely responsible for the content of this dissertation. The Graduate College will ensure this dissertation is globally accessible and will not permit alterations after a degree is conferred.

Iowa State University

Ames, Iowa

2019

DEDICATION

I would like to dedicate this work to my father, Ashok R. Gaonkar. His dedication, constant support, and tireless enthusiasm made me into the person I am today. He had a zeal for the pursuit of knowledge, which he imparted into me at a very young age. He was incredibly delighted when I decided to pursue a PhD in solar photovoltaics, and I am sure he would be extremely proud of me today. This work is also dedicated to my mother, Shaila Gaonkar, whose strength and love is a continuing source of inspiration to me.

TABLE OF CONTENTS

Page

LIST OF FIGURES

Page

ACKNOWLEDGMENTS

First and foremost, I would like to thank my research advisor and mentor, Professor Vikram Dalal. In 2016, he gave me the opportunity to work in his research group; little did I know back then that choosing to study under his tutelage would become one of the best decisions of my life. Professor Dalal continuously inspired me with his deep knowledge, amazing work ethic, and caring toward his students. With Professor Dalal's guidance I learned to work both hard and smart, to set my standards for myself high, and to push myself until I am able to achieve my goals. I will utilize the lessons I learned under his mentorship as I enter my career and throughout my life.

I would like to thank the members of my Program of Study Committee: Dr. Rana Biswas, Dr. Ruth Shinar, Dr. Jaeyoun Kim and Dr. Mani Mina for their guidance and encouragement during my doctoral research.

I would like to thank Dr. Ranjith Kottokkaran for sharing with me his immense experience and deep knowledge of vapor deposited perovskites and fabrication techniques. I looked forward to our daily discussions, from which I gained a deeper understanding of issues with fabrication and troubleshooting problems. Without him, the lab would not have been as lively.

I would like to thank Max Noack for the technical support and advice he gave me with scientific instrumentation and vacuum deposition systems. I feel that each of my conversation with Max resulted in me learning something new. Max was the go-to guy when anyone had an issue with a vacuum deposition system, and I appreciate his steadfast dedication to sharing expertise with those of us in the lab.

I would like to thank Junhao Zhu for tirelessly working by my side in our quest for thermally stable perovskites. Junhao was a fantastic teammate, and his work ethic and energy inspired me. Thank you for making my final months at MRC some of the most enjoyable.

I would like to thank the senior PhD student researchers in the group: Dr. Mehran Samiee, Dr. Istiaque Hossain, Dr. Pranav Joshi, Dr. Satvik Shah, Dr. Tanvir Muntasir and Dr. Liang Zhang, who taught me about semiconductor physics and device characterization. I appreciate their advice and guidance. I would also like to thank my more recent lab mates, including Jiayan Huo, Laila-Poly Parvin, Saba Sharikadze, Behrang Bagheri, and Nishthta Bhatnagar.

Finally, I would like to thank my parents, Ashok Gaonkar and Shaila Gaonkar. Their sacrifice, support and tireless encouragement made who I am today. I would also like to my girlfriend, Shelby Rae Stringfield, whose support and encouragement made my time in Ames, Iowa much more enjoyable.

I would like to thank National Science Foundation for supporting my work financially.

ABSTRACT

Perovskite solar cells have garnered a great deal of attention in the solar cell research community. Their attractive optical and electronic properties—such as their high absorption coefficient, long diffusion lengths, low defect densities, and low exciton binding energies—make perovskites an excellent choice for photovoltaics. The fact that their optical and electronic properties can be tuned through changing the perovskite composition provides researchers with a vast playing field.

The meteoric rise of the power conversion efficiencies of hybrid organic-inorganic perovskites, from 3.8% to 23.6% in less than a decade of research, has attracted huge interest from the academic community. Despite the superior efficiencies of hybrid organic-inorganic perovskite solar cells, their thermal instability, primarily caused by the volatility of the organic cation, remain a serious limitation in their deployment into real world conditions.

This report eschews the use of solution processing for the growth of the perovskite layer due to its inherent problems with reproducibility and scalability. Instead, the research described herein utilized a commercially viable and scalable vapor deposition technique by sequential layer-by-layer vacuum deposition of the perovskite layer using a custom-built vacuum deposition system.

The initial part of this report displays our work on replacing the thermally volatile organic cation with the inorganic cation, Cesium, to form fully inorganic cesium lead iodide ($CsPbI_3$) perovskites. We optimize the device performance of the cesium lead iodide perovskites solar cells to fabricate devices with a photoconversion efficiency of 11.2% using a p-i-n architecture with the structure ITO/PTAA/ $CsPbI_3$/PCBM/Al.

The second part of this report focuses on the partial substitution of the iodide anion with a bromide anion to improve the thermodynamic instability of the cesium lead iodide perovskite. We employ Indium doped Cadmium Sulphide as the electron transport layer and P3HT as the hole transport layer to fabricate n-i-p devices with a photoconversion efficiency of 11.7%.

Most importantly, we have demonstrated the thermal stability of these cesium lead mixed halide perovskites through X-Ray diffraction analysis, showing no compositional or phase degradation at 200°C for extended periods of time. Further, we have shown that our device performance exhibits no degradation during the thermal stability test at 200°C for over 72 hours.

Throughout this report, we study the effect of several key parameters of the perovskite fabrication process that control the intermixing of the perovskite layers and their effect on device efficiency and hysteresis. Further, we employed several characterization techniques to study important material parameters of the deposited perovskite material, such as the density of deep defects and the Urbach energy of the valence band tail states necessary for optimal device performance. The characterizations indicate the high quality of the material grown with our layer-by-layer vapor deposition technique with a density of deep defects in the $7x10^{15}/cm^3/eV$ range, an Urbach energy of 21meV, and a dielectric constant of 28.

CHAPTER 1. INTRODUCTION TO PHOTOVOLTAICS

Global energy demand is steadily increasing, growing by 2.3% in the last year alone to result in its fastest pace in a decade, hitting 14,000 million tonnes of oil equivalent (MTOE) [Fig 1.1]. The increase was driven by a robust global economy and an ever-increasing population. Consequently, global energy related CO2 emissions increased by 1.7% in 2018, equaling 37.1 Gigatonnes of CO2, a hitherto unforeseen level [Fig 1.2] [1,2]. The global energy demand is predicted to reach 17,000 million tonnes of oil equivalent by the year 2040[3]. Due to this ever-expanding global demand for energy, prominent methods of energy production that both rely on finite sources and cause negative environmental impacts—such as fossil fuels and coal—will inevitably become unsustainable, requiring urgent research on sustainable methods of renewable energy.

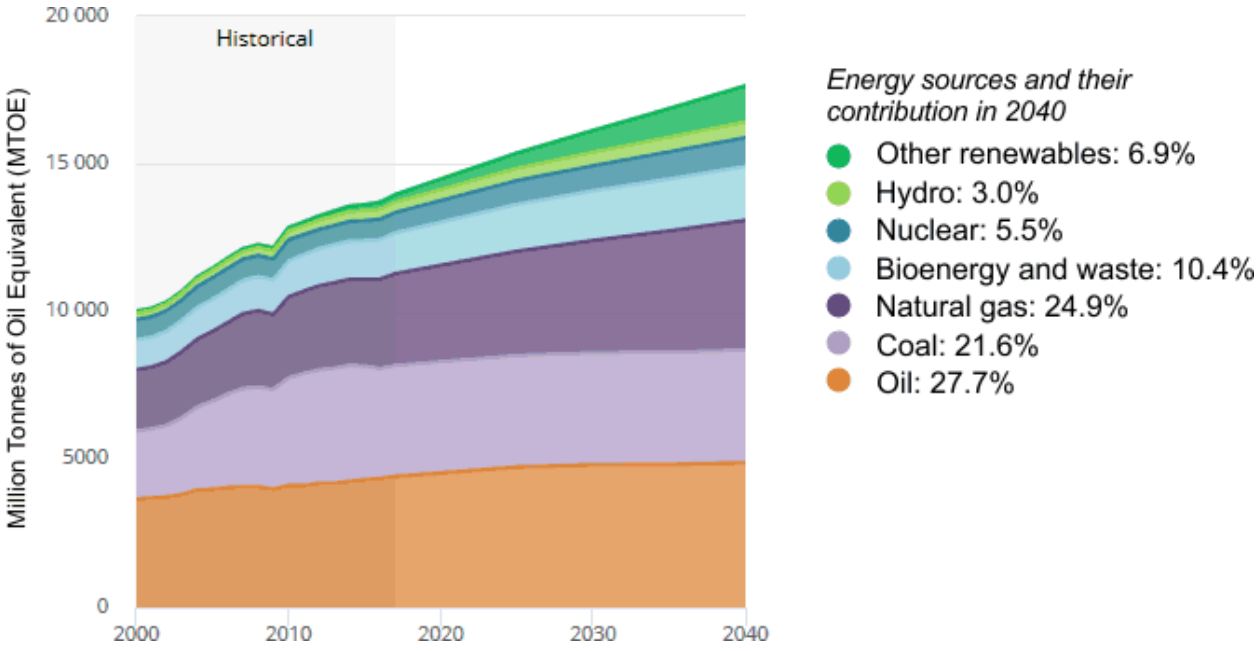

Figure 1.1: Global energy demand and predicted energy demand in million tonnes of oil equivalent

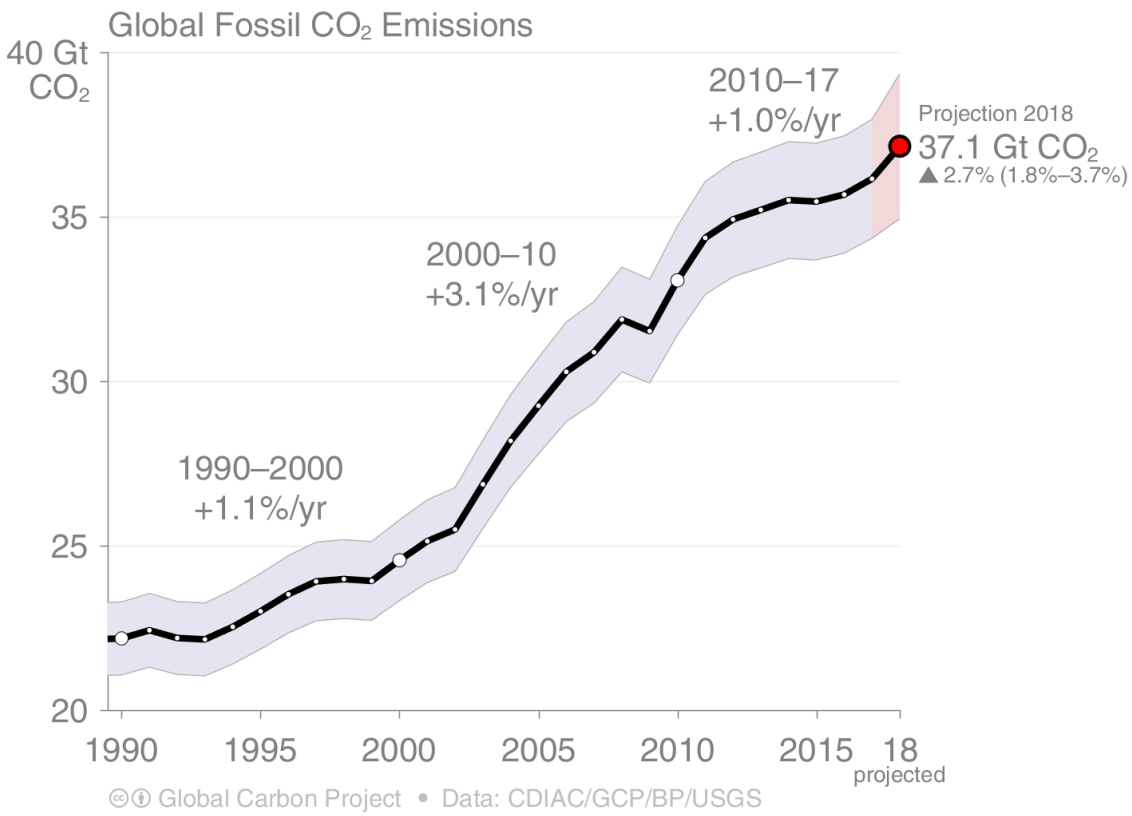

Figure 1.2: Global fossil fuel CO2 emissions

Solar energy is one of the most abundant forms of energy available with a theoretical potential of 23000 TW per year, dwarfing the world's current consumption of ~20TW per year [4]. Among the various ways in which we can harness solar energy, solar photovoltaics with a technical potential of 7500TW per year offer us one of the most promising options to meet the ever-increasing energy demands of future generations without causing a negative impact on the global climate.

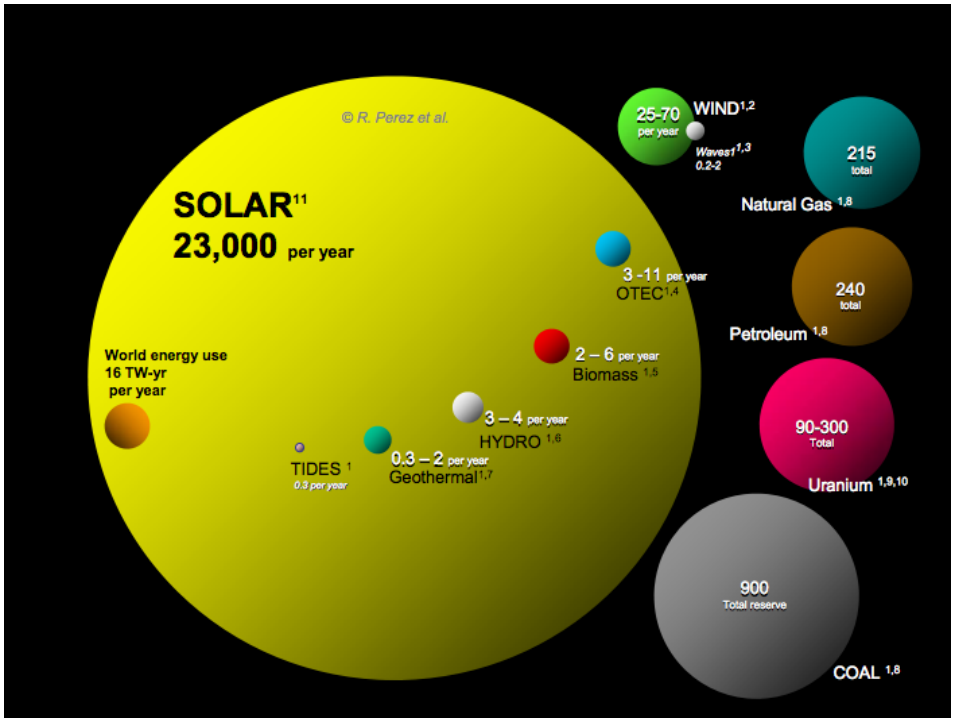

Figure 1.3: Theoretical potential of various energy sources in TW per year

Currently, a majority of the world's energy consumption comes from non-renewable sources. Solar photovoltaics contribute less than 2% to the world's energy demand due to the higher cost per energy unit of solar photovoltaics compared to conventional, non-renewable energy sources [Fig 1.4][5].

Figure 1.4: Cost per kWh of energy generation using various technologies in 2018

What is encouraging, however, is that cost per watt of solar photovoltaics is decreasing exponentially—from $76/Watt to less than $ 0.25/Watt in 2017 in the last 40 years [Fig 1.5][6]. This fall in photovoltaic energy costs is largely due to the advances in fabrication technologies and decreasing cost of materials.

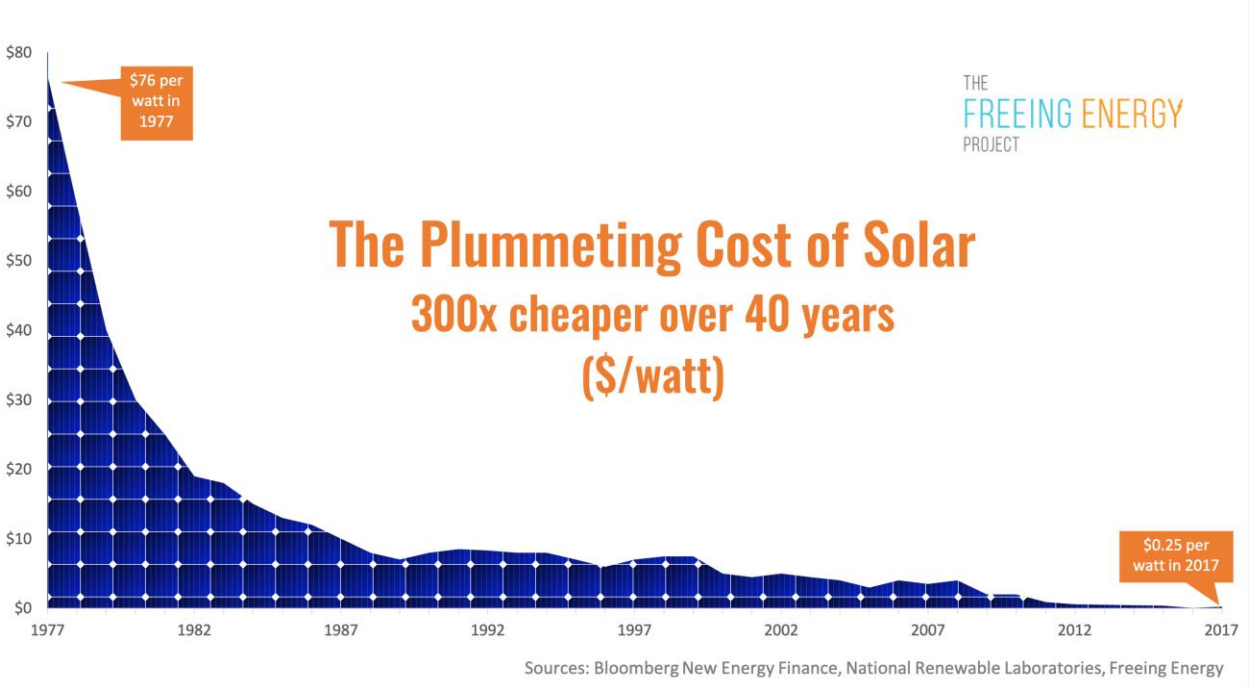

Figure 1.5: Plummeting cost of solar PV

Owing to the sharp decrease in costs of solar photovoltaics, the deployment of photovoltaics has exponentially risen with more than 100GW of solar photovoltaics expected to be added in 2019 [Fig 1.6] [1,7].

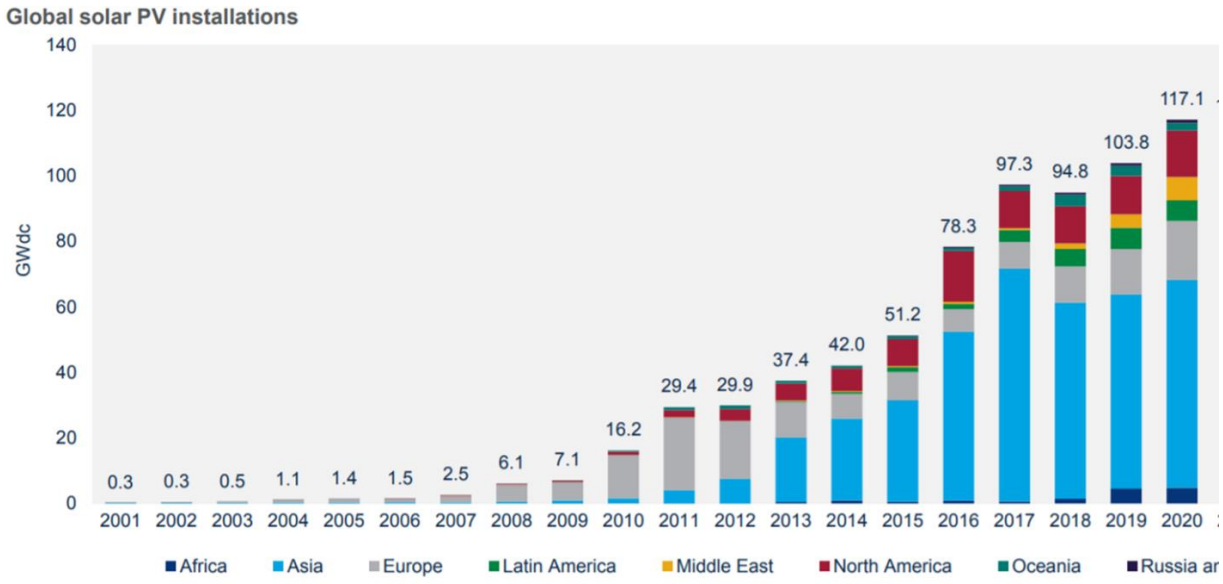

Figure 1.6: Rapid increase in global solar PV installations expected to hit over 100GW added in 2018

Though solar energy deployment is steadily rising, work still needs to be done to make access to solar energy feasible for the general public. A concerted attempt to reduce the cost of solar photovoltaics in needed to continue the advances made in the cost of solar energy. A significant portion of the solar research community is focused on the development of new photovoltaic materials that can be synthesized and deposited at low prices to make PV modules more affordable.

Outline of this thesis

Chapter 2 describes the fundamental operating principles of a photovoltaic device. We understand the four fundamental processes in the working of a solar cell. We also look at the working principle and the equivalent circuit of a solar cell.

Chapter 3 covers the various characterization techniques we use to understand the operational principles and troubleshoot problems in a solar cell.

Chapter 4 provides an introduction into perovskites solar cells. We cover the several advantages of working with perovskite materials as well as the challenges we need to overcome with perovskites for commercial deployment in the real world. Chapter 4 also introduces inorganic perovskites and their advantages over hybrid perovskites.

Chapter 5 covers the fabrication techniques used for perovskite solar cells with a strong emphasis on vapor deposited perovskites. The vapor deposition technique and the deposition system used in this thesis is described in detail.

Chapter 6 focuses on the fabrication and optimization of cesium lead iodide perovskites. We describe the various optimization of the fabrication process and characterization of the perovskite solar cells. Chapter 6 closes with the problems facing cesium lead iodide perovskites.

Chapter 7 is centered on cesium lead mixed halide perovskites and the strategies employed to improve stability of cesium lead iodide perovskites. We look at the device optimizations and the effect of several key fabrication parameters on device performance. Several important material parameters of the perovskite material are also discussed with a focus on how these material parameters affect device performance. The thermal stability of the mixed halide composition is also described.

Chapter 8 summarizes the entire report while presenting the future work needed for commercial deployment of these perovskite materials.

References

1. Global Energy & CO2 Status Report 2018, International Energy Agency
2. GLOBAL ENERGY GROWTH IS OUTPACING DECARBONIZATION, 2019, Global Carbon Project
3. World Energy Outlook 2018, International Energy Agency
4. Perez, Richard & Perez, Marc. (2009). A fundamental look at energy reserves for the planet
5. Renewable Energy Policy Network for the 21st Century, p. 30. (2017)
6. Free Energy; https://www.freeingenergy.com/why-does-the-cost-of-renewable-energy-continue-to-get-cheaper-and-cheaper/
7. US Energy Information Administration (EIA) in June 2015 jc-solarhomes.com/PV/low_cost_pv.htm

CHAPTER 2. FUNDAMENTALS OF SOLAR CELLS

Quite simply, a solar cell is a pn junction device that converts light energy from the sun into usable electrical energy. The basic structure of a p-n junction solar cell is illustrated in Fig 2.1. Photons are absorbed by the pn junction and give rise to electron hole pairs. The electron hole pairs drift/diffuse and are collected by the contact layers of the solar cell. These separated electrons and holes are extracted from the solar cell through the electron and hole transport layers and dissipate their energy in an external load before they recombine in the solar cell. Solar cells can be constructed with various structures. This report focusses on devices with a p-i-n or n-i-p structure throughout this thesis (Fig 2.2). Both these structures have an intrinsic (i) or lightly doped active layer sandwiched between a highly doped n^+ layer and a highly doped p^+ layer. The central difference between the p-i-n structure and the n-i-p structure is that the light impinges on the p^+ layer first in the case of a p-i-n device, while light impinges first on the n+ layer in a n-i-p device. The i-layer is usually a very lightly doped semiconductor material with a high absorption coefficient where most of the light absorption takes place. The highly doped n+ and p+ layers act to create a strong electric field in the i-layer. The electrons and holes undergo drift transport under the influence of this strong electric field and the electrons are collected in

the n+ layer and the holes in the p+ layer. As a result, the n+ and p+ layers are often termed the Electron Transport Layer (ETL) and the Hole Transport Layer (HTL).

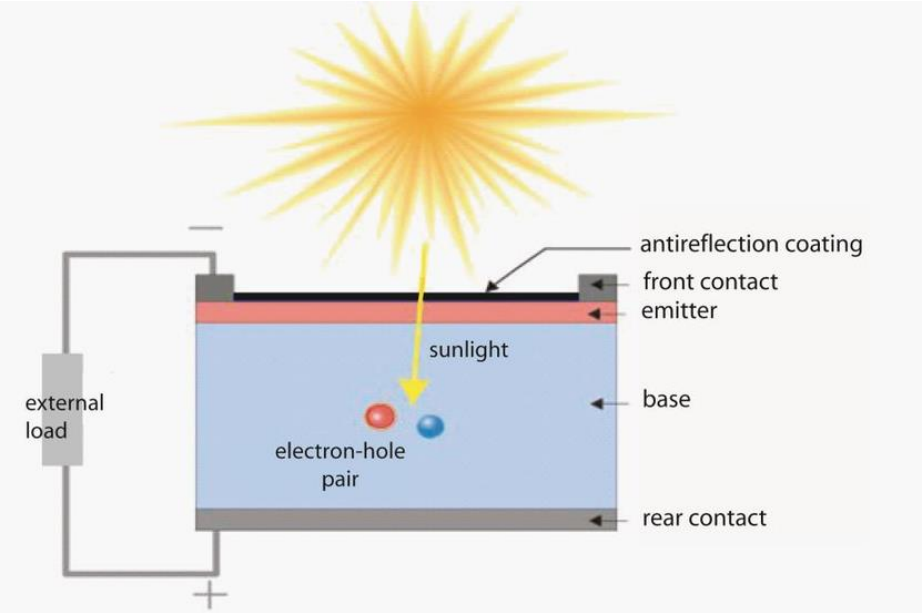

Figure 2.1: Cross section of a pn junction solar cell [1]

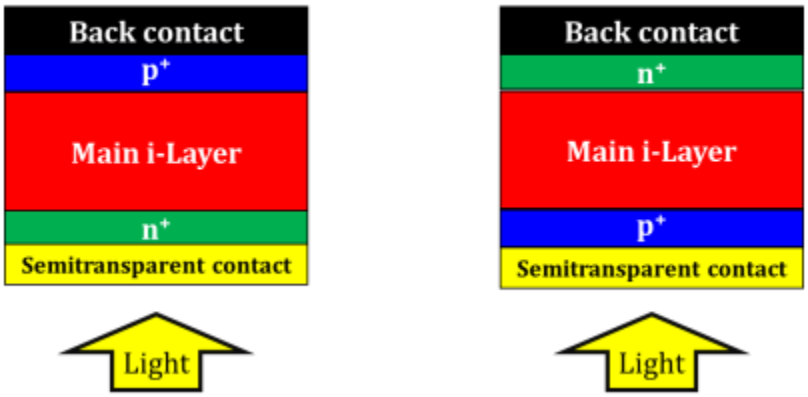

Figure 2.2: Device structure of a n-i-p(left) and p-i-n (right) solar cell

There are four fundamental processes that occur during the photovoltaic energy conversion process; understanding each of them is necessary to grasp how to make an efficient photovoltaic device. The processes are as follows [1]:

1. Absorption of incident photons
2. Generation of charge carriers (electron hole pairs)
3. Transport of photo-generated charge carriers
4. Collection of photo-generated charge carriers

Each of these fundamental processes will be discussed in detail over course of the following sections, as well as the recombination process that leads to a loss in the performance of a solar cell and the equivalent circuit model of a solar cell.

2.1 Absorption of incident photons

This is the first step in the conversion of solar energy into usable electrical energy. Absorption of photons in the active material of the solar cell are governed by the quantum energy of the incident photon and the energy levels of the absorber material. When a photon of energy **(E_{ph}=hv**) equal to or higher than the band gap (**E_g**) of the absorber material is incident on the material, the photon is absorbed, and the optical energy is used to elevate an electron from the valence band of the material to its conduction band. The difference in the energy (**$E_{ph} - E_g$**) then dissipates through collisions with the lattice as thermal energy and the electron relaxes to the bottom of the conduction band. This process is called a band-to-band transition and is shown in Fig 2.3.

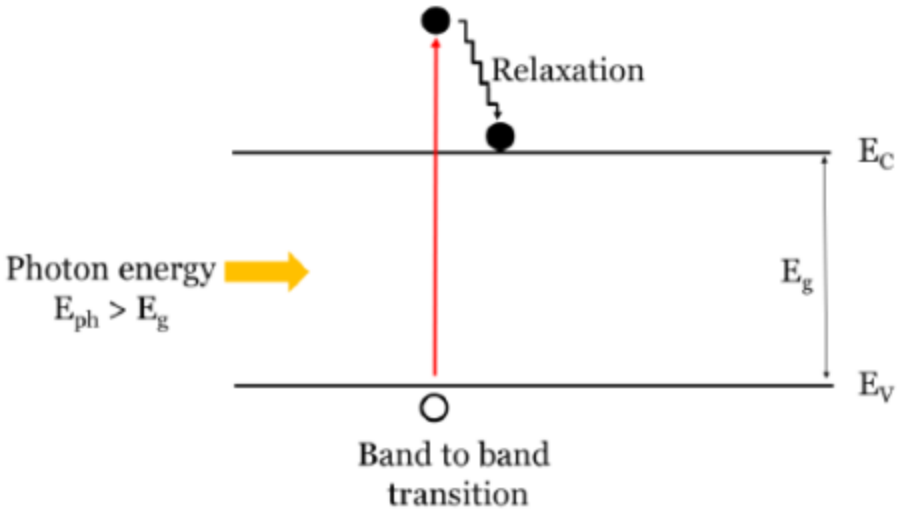

Figure 2.3: Absorption through band-to-band transitions [2]

If, however, the energy of the photon is insufficient, then the photon is unable to impart enough energy to electron in the valence band to transition it directly to the conduction band. Photons with sub-gap energies ($\mathbf{E_{ph} < E_g}$) can still excite electrons to the conduction band by transition through tail states in the conduction and valence bands and mid gap states [Fig 2.4]. These mid gap and tail states have densities orders of magnitude below the conduction and valence bands and thus the sub-gap transitions do not contribute much to charge carrier generation. Sub band gap transitions, however, provide a valuable insight into the distribution of the tail state and mid gap defects in the band structure of the material.

11

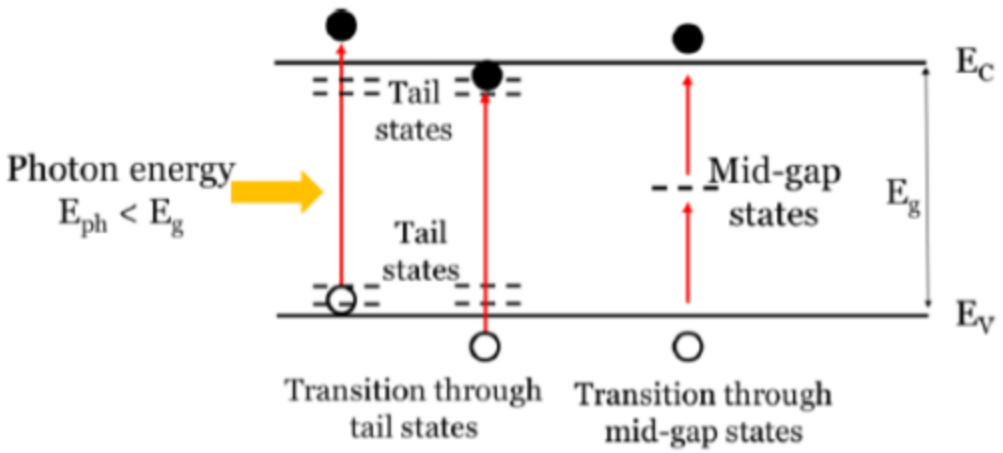

Figure 2.4:Sub-band gap absorption through tail states and mid gap defects [2]

The band gap of the absorber material can be classified into direct band gap material and indirect band gap material depending on the alignment of the minimal energy state of the conduction band and the maximal energy state of the valence band in momentum space [Fig. 2.5]. The band gap is called “direct” when the crystal momentum of the electrons and the holes is the same in the conduction and valence bands, or “indirect” when the crystal momentums are different. Both direct and indirect material are used as absorber layers in solar cells.

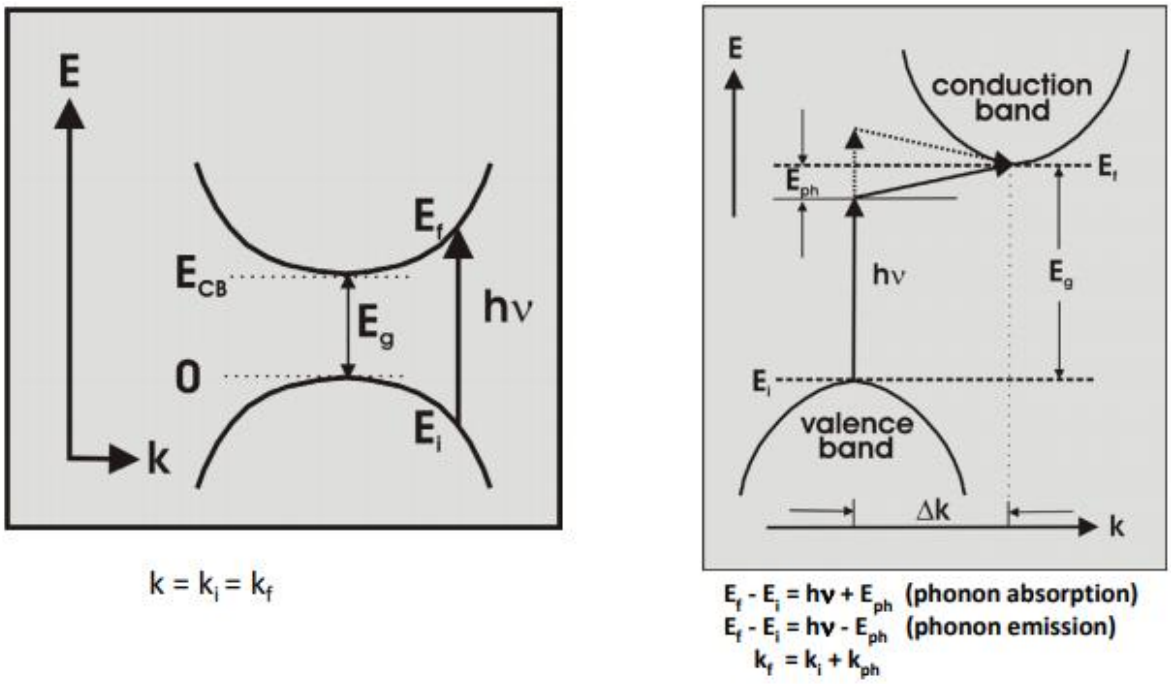

Figure 2.5: Band structures in direct (left) and indirect (right) band gap materials[2]

The absorption coefficient (α) determines how well a material absorbs the incident light. The absorption coefficient is defined by the Beer Lambert's Law:

$$I = I_0 e^{-\alpha x}$$

As light passes through the material, the intensity of the light decreases exponentially with distance where I_0 is the initial intensity before absorption, I is the intensity at a distance x inside the material, and α is the absorption coefficient. The absorption coefficient, which is a function of the wavelength of the light, represents one of the most important parameters when deciding on the photovoltaic material. A higher absorption coefficient implies that a thinner material is enough to harvest the incoming photons. The absorption coefficient shows a sharp decrease as the energy of the light approaches the band gap of the absorber material. Fig 2.6 shows the absorption coefficients of several commonly used photovoltaic materials.

The absorption coefficient for a direct band gap material is given by the empirical relation [3]

$$\alpha = A\sqrt{(h\vartheta - E_g)}$$

where, A is an energy independent constant proportional to the effective electron and hole masses.

The absorption coefficient of an indirect band gap semiconductor is described by

$$\alpha = A\frac{(h\vartheta - E_g \pm E_p)^2}{\pm\left(e^{\left(\frac{h\vartheta}{kT}\right)} - 1\right)}$$

where E_p is the energy of the phonon involved in the transition, k the Boltzmann constant, and T the temperature.

The absorption coefficient of direct band gap materials (CdTe, a-Si:H, GaAs) is higher than indirect band gap semiconductors such as c-Si. The lower absorption coefficient requires solar cells made with indirect band gap materials like c-Si to have a much thicker absorber layer (~mm) as compared to thin active layers found in direct band gap materials (~microns thick).

Absorption of photons with energies only slightly lower than the band gap primarily occur through tail states transitions and is governed by [5],

$$\alpha = Ae^{\left(\frac{(h\vartheta)}{E_U}\right)}$$

where E_U, the Urbach energy, is a measure of the density of tail states.

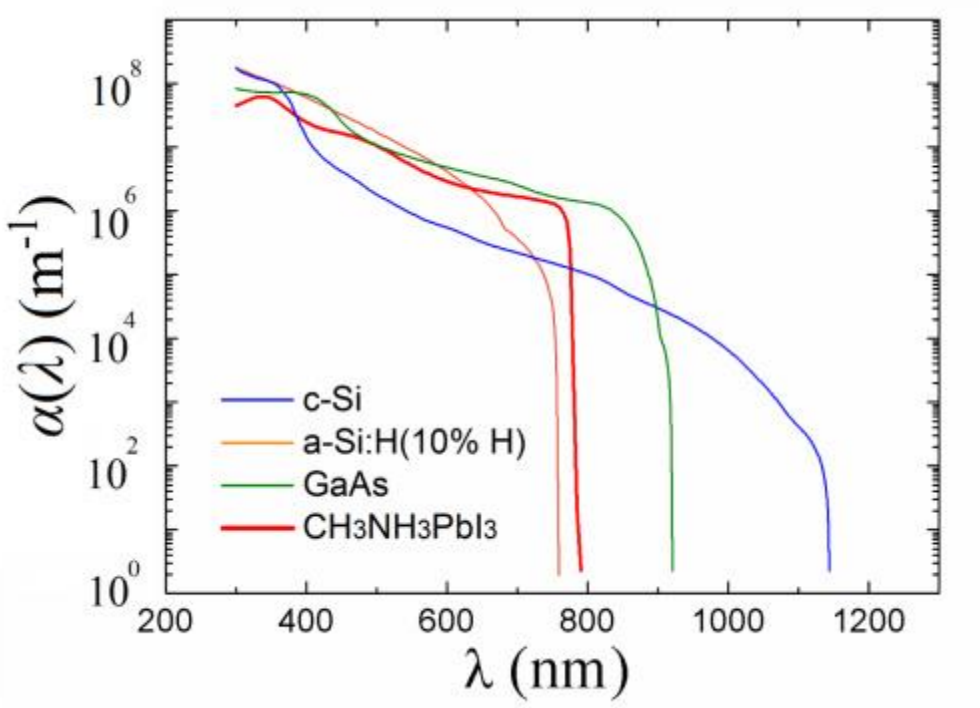

Figure 2.6: Absorption coefficients of commonly used photovoltaic materials as a function of wavelength (λ)[7]

2.2 Generation of charge carriers

Upon the absorption of a photo-generated electrons, hole pairs are generated in the semiconductor. The electron hole pairs can be unbound free charges or bound by an attractive Columbic force, which stabilizes the energy of the electron hole pair. The bound state quasi neutral particle is called an exciton. The binding energy of the exciton in the material determines whether the electron hole pairs are bound or unbound. The binding energy of an exciton in a dielectric material is related to the dielectric constant of relative permittivity in the material and is given by:

$$E_b = \frac{\mu e^4}{2\,\hbar^2\,\epsilon^2}$$

where μ is the reduced mass of the electron, e is the electronic charge, $\hbar$ is Plank's constant, and ε is the relative permittivity of the material.

When the exciton binding energy of the material is higher than the thermal energy at room temperature (kT = 25.9meV), then the electron hole pairs remain bounded as excitons. c-Si and perovskite materials have exciton binding energies lower than the thermal energy and thus the electron hole pairs can be transported freely [9,10]. In contrast, organic semiconductors with dielectric constants in the range of 2-5 have binding energies much higher than the thermal energy and thus the electron-hole pairs remain in the bound state, their collection requiring excitonic dissociation with heterojunctions.

2.3 Transport of charge carriers

Once the charge carriers are generated, they need to be separated and transported to the device contacts for collection [11]. Charge carrier transport can occur through either drift or diffusion transport, depending on the presence or absence of an electric field [12]. Charge transport in the presence of an electric field occurs through drift transport, while in the absence of an electric field the charge carriers are transported by the gradient in the concentration of charge carriers in the device. Both drift and diffusion transport are governed by the ambipolar transport equation,

$$\frac{\partial \Delta n}{\partial t} = D' \frac{\partial^2 \Delta n}{\partial x^2} + \mu' \varepsilon \frac{\partial \Delta n}{\partial x} + G - R$$

where, Δn is the excess concentration of electrons, μ' is the ambipolar mobility, ε is the electric field, D' is the ambipolar diffusion constant, G is the generation rate, and R is the recombination rate. The ambipolar mobility μ' and ambipolar diffusion constant, D' are given by

$$\mu' = \frac{\mu_n \mu_p (p - n)}{n\mu_n + p\mu_p}$$

$$D' = \frac{n\mu_n D_p + p\mu_p D_n}{n\mu_n + p\mu_p}$$

where μ_n, μ_p, D_n and D_p are the electron and hole mobilities and diffusion constant, respectively. N and p are the electron and hole concentration, respectively.

Considering the case of a n-type semiconductor (n >> p) with low level injection (($\Delta n = \Delta p$) << n), ambipolar equation reduces to

$$\frac{\partial \Delta p}{\partial t} = D_p \frac{\partial^2 \Delta p}{\partial x^2} + \mu_p \varepsilon \frac{\partial \Delta p}{\partial x} + G - \frac{\Delta p}{\tau_p}$$

where τ_p is the lifetime of the hole. This illustrates how minority charge carriers (holes, in this case) dominate the transport process in a solar cell under low level injection. Similarly, electrons transport is the deciding mechanism in the case of a p-type semiconductor at low level injection.

When the transport of charge carriers is diffusion dominated, which occurs in the absence of an electric field, the ambipolar transport equation further reduces to

$$\frac{\partial \Delta p}{\partial t} = D_p \frac{\partial^2 \Delta p}{\partial x^2} + G - \frac{\Delta p}{\tau_p}$$

At a steady state condition, assuming no excess charge carrier generation, the equation can be solved as a second order differential equation.

$$\frac{\partial \Delta p}{\partial t} = D_p \frac{\partial^2 \Delta p}{\partial x^2} + G - \frac{\Delta p}{\tau_p} = 0$$

$$\Delta p = \Delta p(x = 0) e^{-\frac{x}{L_p}}$$

where L_p, the diffusion length of holes, is defined by

$$L_p = \sqrt{D_p \tau_p}$$

This suggests that the minority charge carrier concentration decay exponentially with distance and thus a higher diffusion length is beneficial for charge collection efficiency. Ensuring that the thickness of the absorber layer is smaller than the charge carrier diffusion length is critical for good device performance in a diffusion based solar cell.

If the diffusion length in a material is not high enough and reduction of the thickness of the absorber layer is not possible due to low absorption coefficients, then an electric field is required for drift-based charge transport. In the case of an n-type semiconductor material with a strong internal electric field at steady state condition, the ambipolar equation can be solved similarly,

$$\frac{\partial \Delta p}{\partial t} = \mu_p \varepsilon \frac{\partial \Delta p}{\partial x} + G - \frac{\Delta p}{\tau_p} = 0$$

$$\Delta p = \Delta p(x = 0) e^{-\frac{x}{R_p}}$$

$$R_p = \mu_p \tau_p \varepsilon$$

where R_p is the drift range of holes [13]. Here it is assumed that drift-based transport dominates any diffusion-based transport due to the strong electric field. In the case of both drift and diffusion transport, a critical electric field can be defined that determines the dominant transport mechanism.

$$\varepsilon_C = \frac{kT}{eL_p}$$

If the internal electric field is larger than ε_c, then the transport is drift dominated, else it is diffusion dominated.

A p-i-n structure solar cell leverages the electric field generated by the highly doped n+ and p+ layers to improve charge transport in the absorber i-layer, sidestepping any concerns about the diffusion length not being large enough for efficient diffusion-based collection. The

electric field extends from the n-layer to the p-layer and the electrons and holes are collected in the n-layer and p-layer respectively.

2.4 Collection of charge carriers

After the charge carriers are transported to contacts, they need to be collected by an ohmic contact between the transport layer and the metal electrode. Proper choice of metal work function, one that is higher than the work function of the transport layer, ensures efficient collection of the charge carriers at the electrode.

2.5 Recombination

Recombination processes lead to a loss in photogenerated charge carriers and reduce efficiency of the solar cell. Recombination processes can be either radiative, where the excess energy is released as a photon, or non-radiative, where the energy is released as thermal energy. There are three major recombination mechanisms: band to band recombination, trap assisted recombination (Shockley Reed Hall recombination), and Auger recombination. [11,12,13]

2.5.1 Band to Band Recombination

In band to band recombination, the electron from the conduction band combines with a hole from the valence band with the release of excess energy in the form of a photon [Fig 2.7 (a)] . This is a form of radiative recombination. The rate of recombination is governed by

$$R_B = C_B(np - {n_i}^2)$$

where C_B is the band-to-band recombination coefficient and n_i is the intrinsic carrier concentration [11,12]. Considering the case of low-level injection (($\Delta n = \Delta p$) << n) in a n-type material (n >> p), this equation reduces to

$$R_B = C_B(n\Delta p) = \frac{\Delta p}{\tau_p}$$

$$\tau_p = \frac{1}{C_B n}$$

The lifetime of the minority charge carriers (τ_p, in this case) is inversely proportional to the concentration of the majority charge carriers (n).

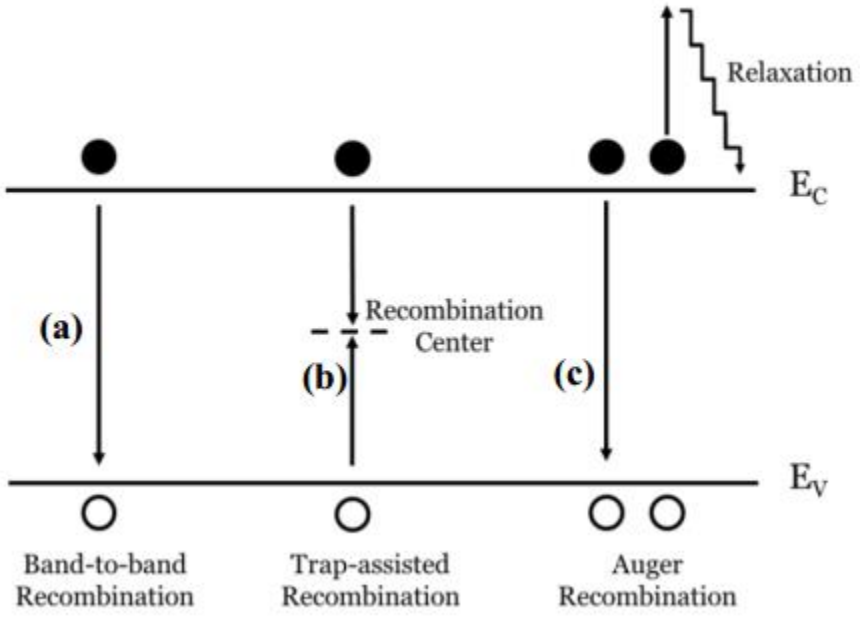

Figure 2.7: Recombination mechanisms; (a) band-to-band recombination, (b) SRH recombination, (c) Auger recombination

2.5.2 Trap Assisted Recombination (Shockley Reed Hall recombination)

Here the electron hole recombination is mediated by the presence of a trap state within the band gap of the material[Fig 2.7 (b)]. Trap states can exist both in the bulk as well as at interfaces [11,12].

SRH recombination is governed by

$$R_{SRH} = \frac{(np - {n_i}^2)}{\tau_p(n + n_1) + \tau_n(p + p_1)}$$

$$n_1 = n_i e^{\left(\frac{E_T - E_i}{kT}\right)}$$

$$p_1 = n_i e^{\left(\frac{E_i - E_T}{kT}\right)}$$

where E_T and E_i are the trap energy and intrinsic energy level, respectively. For a low-level injection in an-type material, the equation simplifies to

$$R_{SRH} = C_p \Delta p N_T$$

$$\tau_p = \frac{1}{C_p N_T}$$

where C_p is the SRH recombination coefficient for holes and N_T is the density of traps states. We see that for SRH recombination the minority charge carrier lifetimes are a function of the number of traps present.

2.5.3 Auger recombination

During Auger recombination the excess energy generated during the transition is transferred to a second electron in the conduction band, which excites it higher into the conduction band[Fig 2.7 (c)]. This energy is later dissipated as thermal energy due to lattice collisions. Auger recombination is dominant in heavily doped semiconductors. Auger recombination is governed by

$$R_A = C_A n(np - {n_i}^2)$$

for a n-type semiconductor, where C_A is the Auger recombination coefficient. At low level injection this reduces to

$$R_A = C_A n_0 \Delta p = \frac{\Delta p}{\tau_p}$$

$$\tau_p = \frac{1}{C_A {n_0}^2}$$

In Auger recombination, the lifetime of the minority charge is inversely proportional to the square of the doping density.

In the case where multiple recombination mechanisms are active, the minority charge carrier lifetimes are given by

$$\frac{1}{\tau} = \frac{1}{\tau_B} + \frac{1}{\tau_{SRH}} + \frac{1}{\tau_A}$$

where τ_B, τ_{SRH}, τ_A are the minority carrier lifetimes for band-to-band, and SRH and Auger recombination respectively.

2.6 Shockley Queisser (SQ) Limit

Shockley and Queisser calculated the theoretical efficiencies of an ideal solar cell under the generation, recombination, and transport equations discussed above. Considering only the absorption losses, recombination losses, and black body radiation losses, they calculated the maximum theoretical efficiencies for solar cell given the band gap of their active absorber layers [14]. Fig 2.8 shows how the maximum theoretical efficiency relates to the band gap with thermodynamic losses dominating below 1.34eV. Here, a large fraction of the energy collected by the solar cell is lost due to the thermal relaxation of the electrons to the bottom of the conduction band. Above 1.34eV, absorption losses dominate where the absorber is unable to collect photons with energies below the band gap of the material. Peak theoretical efficiency is achieved at 1.34eV with a maximum efficiency of 34%. Fig 2.9 illustrates the proportion of energy losses and usable electric power generated for various band gaps [15].

31

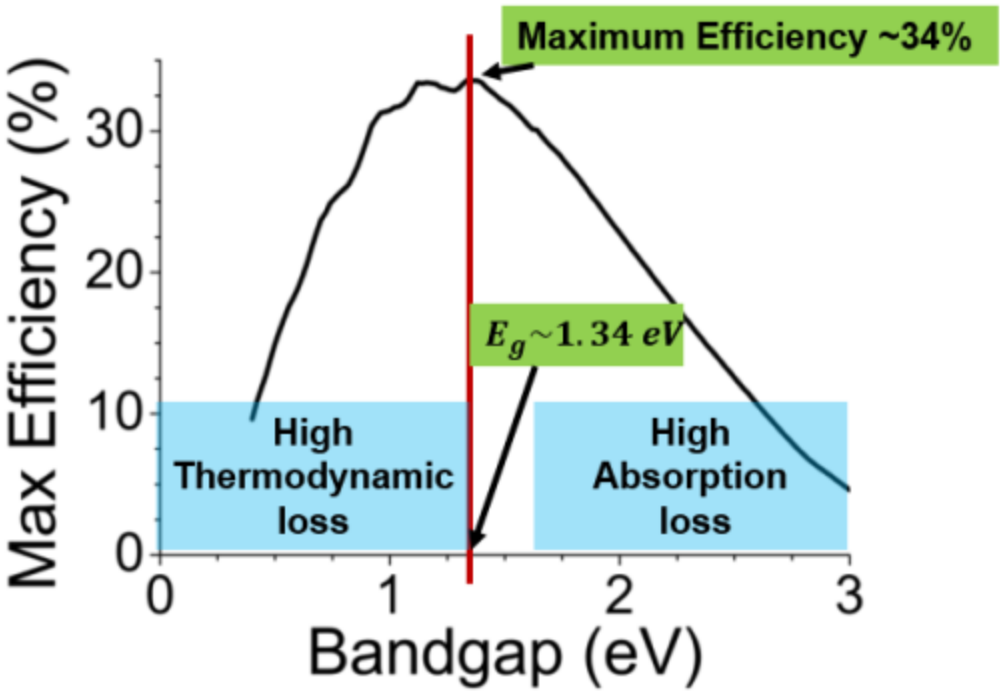

Figure 2.8: Shockley-Queisser Limit of the maximum theoretical efficiency for a single-junction solar cell as a function of absorber layer band gap [14]

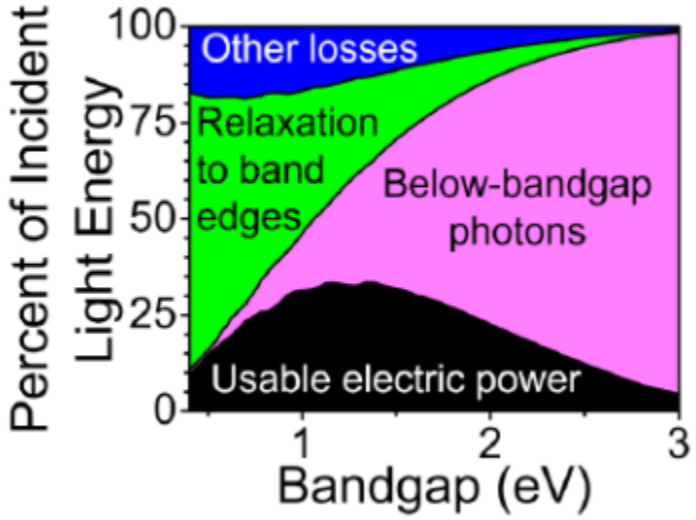

Figure 2.9: Usable electrical energy and energy losses as function of absorber layer band gap [15]

Fig. 2.10 compares the SQ limit with various current technologies. Several recombination losses and parasitic losses not considered in the SQ limit further reduce the achievable efficiency of solar cells. Several technologies have been developed through which the SQ limit can be surpassed, such as photon up conversion and photon down conversion, concentrator photovoltaics, multi junction, and tandem solar cells.

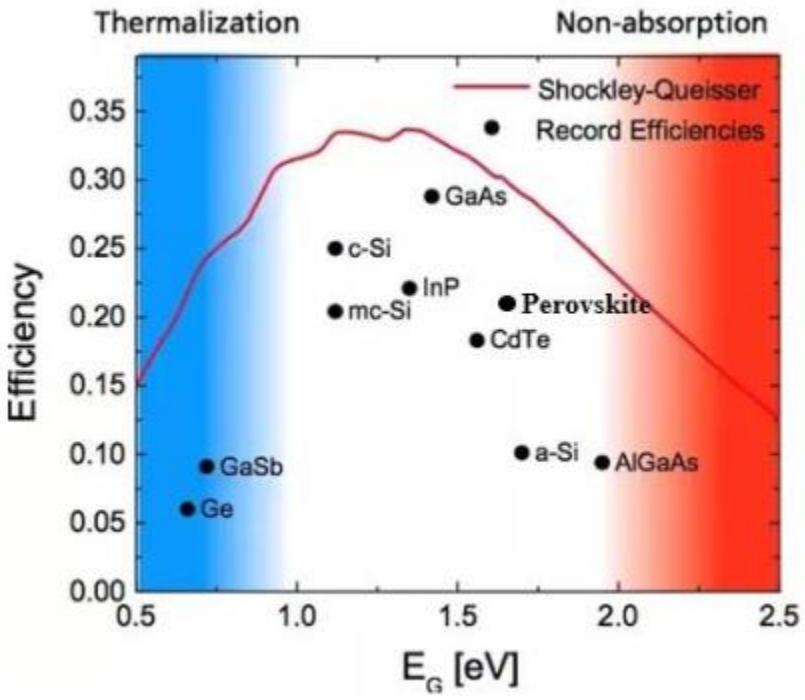

Figure 2.10: Maximum photoconversion efficiency achieved by various photovoltaic technologies compared to the maximum theoretical efficiency from the Shockley Queisser Limit

2.7 Working Principle of a solar cell

In section 2.3, we have seen how a sandwich structure with the intrinsic layer between two highly doped n+ and p+ layers helps in efficient charge collection. Here, we explore the

working principle of such a p-i-n structure solar cell [Fig 2.11]. In a p-i-n solar cell, the light is first incident on the p+ layer, must be chosen so that it possesses a high enough band gap that it does not absorb much of the light. Ideally, the valence band of the p+ layer must match well with the valence band of the absorber i-layer to easily collect electrons, but the conduction band of the p+ layer should be higher than that of the i-layer to form an effective barrier for the holes. The absorber i-layer should be thick enough to ensure complete absorption of light with the thickness being close to the absorption depth for all wavelengths of light below the energy band gap of the material. On the other hand, the conduction bands of the absorber i-layer and the n+ layer should match with the valence bands being offset to facilitate easy collection of holes and block electrons.

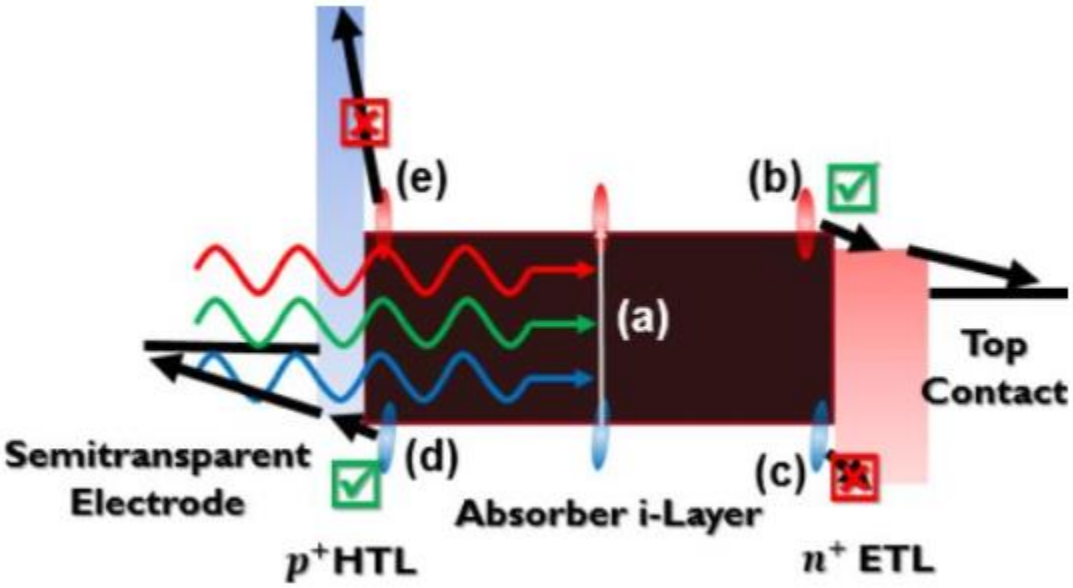

Figure 2.11: Simplified band diagram of a p-i-n junction solar cell. (a) Absorption of light and generation of charge carriers; (b) collection of electrons and (c) rejection of holes at ETL; (d) collection of holes and (e) rejection of electrons at HT

2.8 Equivalent Circuit of a Solar cell

The equivalent circuit of a solar cell comprises of an ideal diode in parallel with a current source, with shunt and series resistance [Fig. 2.12]. The current flowing through an external load is given by [17],

$$I = I_L - I_0\left[e^{\left(\frac{qV}{\eta kT}\right)} - 1\right] - \frac{V + IR_S}{R_{Sh}}$$

where I_L and I_0 are the photo-current and the reverse saturation currents respectively, V is the applied Voltage, η is the ideality factor of the diode, and R_S, R_{Sh} are the series and shunt resistances respectively.

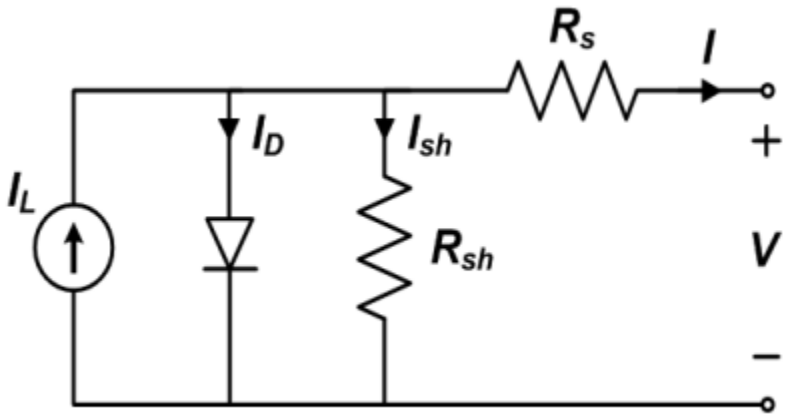

Figure 2.12: Equivalent circuit of a solar cell [17]

The single diode assumes that the ideality factor of the solar cell is constant with voltage, which is not necessarily true. The two-diode model of the solar cell [Fig 2.12] is used to model the recombination mechanisms in the solar cell more precisely. The total current in the two-diode model is given by:

$$I = I_L - I_{01}\left[e^{\left(\frac{qV}{\eta_1 kT}\right)} - 1\right] - I_{02}\left[e^{\left(\frac{qV}{\eta_2 kT}\right)} - 1\right] - \frac{V + IR_S}{R_{Sh}}$$

where I_{01}, I_{02}, and η_1, η_2 are the reverse saturation and ideality factors of the two diodes respectively.

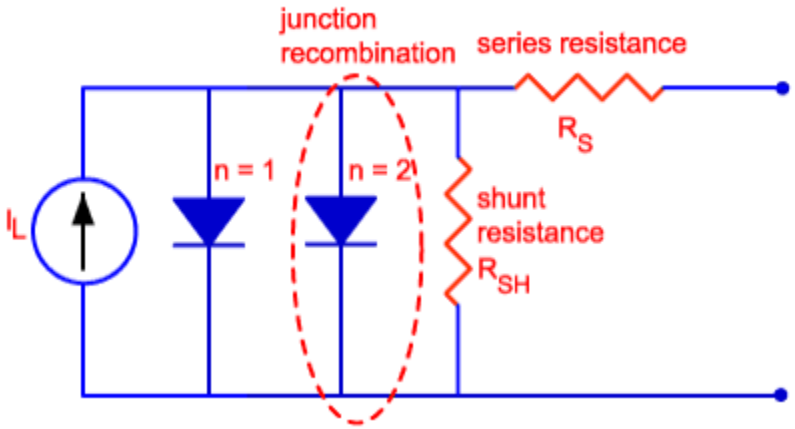

Figure 2.13: Equivalent circuit of a solar cell using the two-diode model

The two diodes represent the two recombination mechanisms of the solar cells. At low biases, recombination in junction region dominates and is represented by the second diode with ideality factor η_2=2 and diode current proportional to $e^{\left(\frac{qV}{2kT}\right)}$. At higher bias conditions, recombination in the bulk region dominates and is represented by the first diode with η_1=1 and diode current is proportional to $e^{\left(\frac{qV}{kT}\right)}$. The two-diode model is useful to model the functioning of the solar cell under no illumination, as the diode currents are usually overshadowed by the much larger photo-current I_L under illumination.

References

1. PV Education
   Link: http://www.pveducation.org

2. B. G. Streetman and S. K. Banerjee, Solid state electronic devices. (Pearson Education, New Jersey, 2006), 6th edition

3. Pranav Joshi, Ph.D. dissertation, “Understanding the photostability of perovskite solar cell”, Iowa State University (2016)

4. Liang Zhang, Ph.D. dissertation, “Device physics of perovskite solar cells”, Iowa State University (2016)

5. Mehran Samiee, Ph.D. dissertation, “Device physics of organic and perovskite solar cells”, Iowa State University (2015)

6. S M Istiaque Hossain, PhD. Dissertation, “Performance and stability of perovskite solar cells”, Iowa State University (2018)

7. J. I. Pankove, “Optical processes in semiconductors”, Dover Pub., New York, 1971
   W. van Roosbroeck and W. Shockley, “Photon-radiative recombination of electrons and holes in germanium” , Phys. Rev. 94, 1558 (1954)

8. F. Urbach, "The long-wavelength edge of photographic sensitivity and of the electronic absorption of solids", Phys. Rev., 92, 1324 (1953). doi:10.1103/PhysRev.92.1324

9. Xie, Z., et al., Refractive index and extinction coefficient of CH3NH3PbI3 studied by spectroscopic ellipsometry. Optical Materials Express, 2015. 5(1): p. 29-43

10. Green, M.A., Improved value for the silicon free exciton binding energy. Aip Advances, 2013. 3(11)

11. Knupfer, M., Exciton binding energies in organic semiconductors. Applied Physics Materials Science & Processing, 2003. 77(5): p. 623-626

12. R. F. Pierret, Advanced semiconductor fundamentals. (Addison-Wesley Publishing Company, Reading, 1987)

13. R. A. Smith, Semiconductors. (Cambridge Univeristy Press, London and New York, 1968)

14. W. Shockley and H. J. Queisser, " Detailed balance limit of efficiency of p-n junction solar cells", J. Appl. Phys., 32, 510 (1961). doi:10.1063/1.1736034

15. U. Rau, B. Blank, T. C. M. Müller and T. Kirchartz, Efficiency potential of photovoltaic materials and devices unveiled by detailed-balance analysis, Phys. Rev. Appl., 7, 044016, 2017,

16. Abderrahmane Belghachi, “Theoretical Calculation of the Efficiency Limit for Solar Cells”, Solar Cells - New Approaches and Reviews, 2015, doi:10.5772/58914

CHAPTER 3. CHARACTERIZATION TECHNIQUES OF SOLAR CELLS

This chapter describes the fundamentals of the various characterization techniques we use to optimize device performance and troubleshoot problems.

3.1 Current-Voltage (IV) measurement

In IV measurements, the voltage applied across the sample is varied and the current values are recorded. When conducted under illumination this measurement is called Light IV, and when conducted under dark conditions it is called Dark IV.

3.1.1 Light IV measurement

The light IV measurement gives us critical information about the photovoltaic device. This measurement gives us the Photoconversion Efficiency of the solar cell, which is the single most important parameter in comparing a solar cell. The light IV measurement is conducted using a Keithley source-measurement-unit (Keithley SMU 237) under illumination by an ABET 105000 solar simulator to obtain the full AM1.5 solar spectrum. The spectrum of the ABET and the AM1.5 spectrum is displayed in Fig. 3.1. A reference Si diode was used to calibrate the light source.

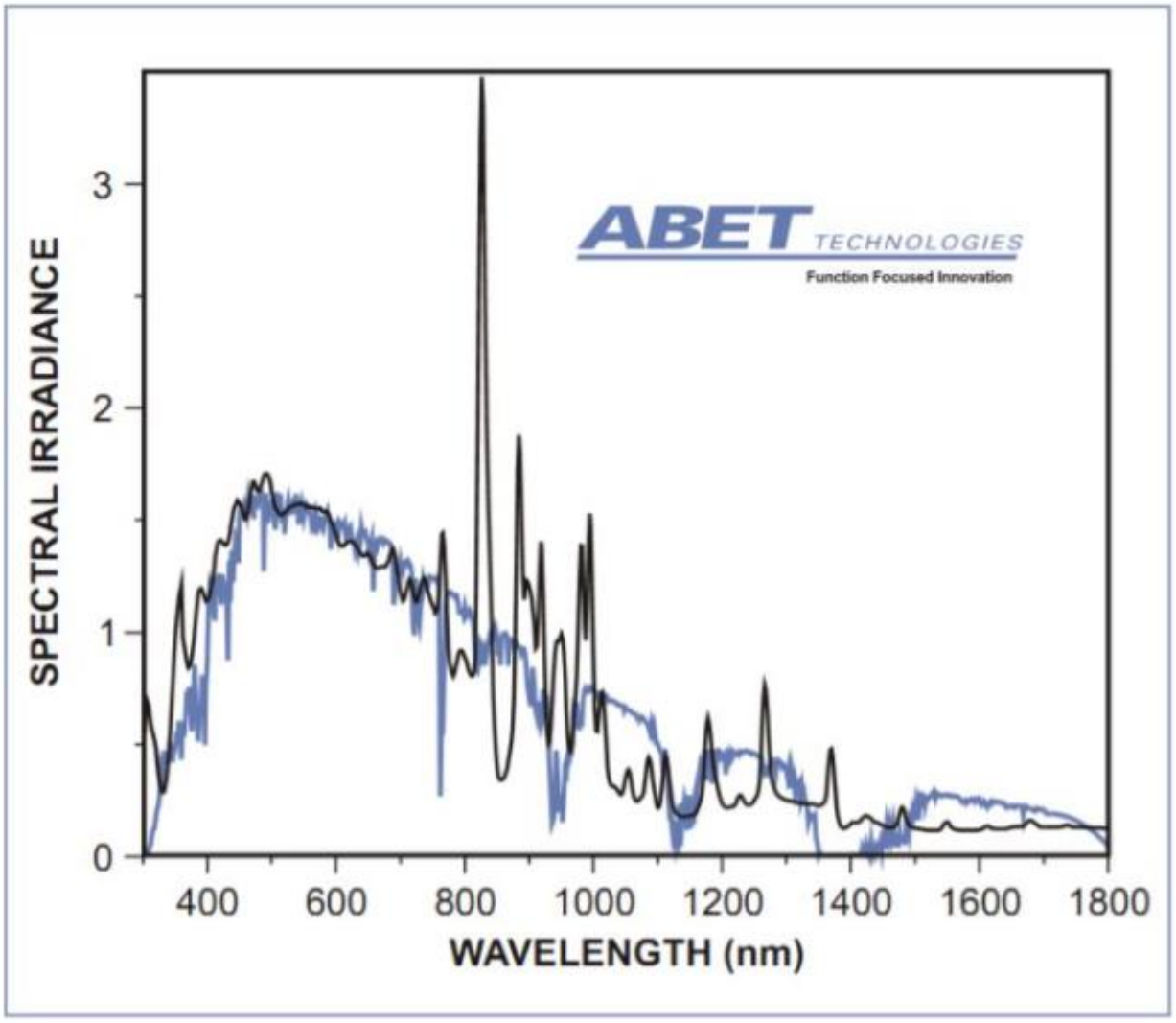

Figure 3.1: AM1.5 spectrum (blue) and simulated spectrum with ABET 10500 solar simulator

Under dark conditions, the IV response of an ideal solar cell is given by[1-3]

$$I = I_0 \left[e^{\left(\frac{qV}{\eta k T}\right)} - 1 \right]$$

which is represented by Fig. 3.2(a) with the IV curve in the 1st quadrant. Under illumination, the light generated current shifts the IV curve down into the fourth quadrant [3.2(b),(c)], where the IV response is given by [1-3]

$$I = I_0 \left[e^{\left(\frac{qV}{\eta kT}\right)} - 1 \right] - I_L$$

Conventionally, the current axis is inverted, as shown in Fig. 3.2(d), and the IV response becomes,

$$I = I_L - I_0 \left[e^{\left(\frac{qV}{\eta kT}\right)} - 1 \right]$$

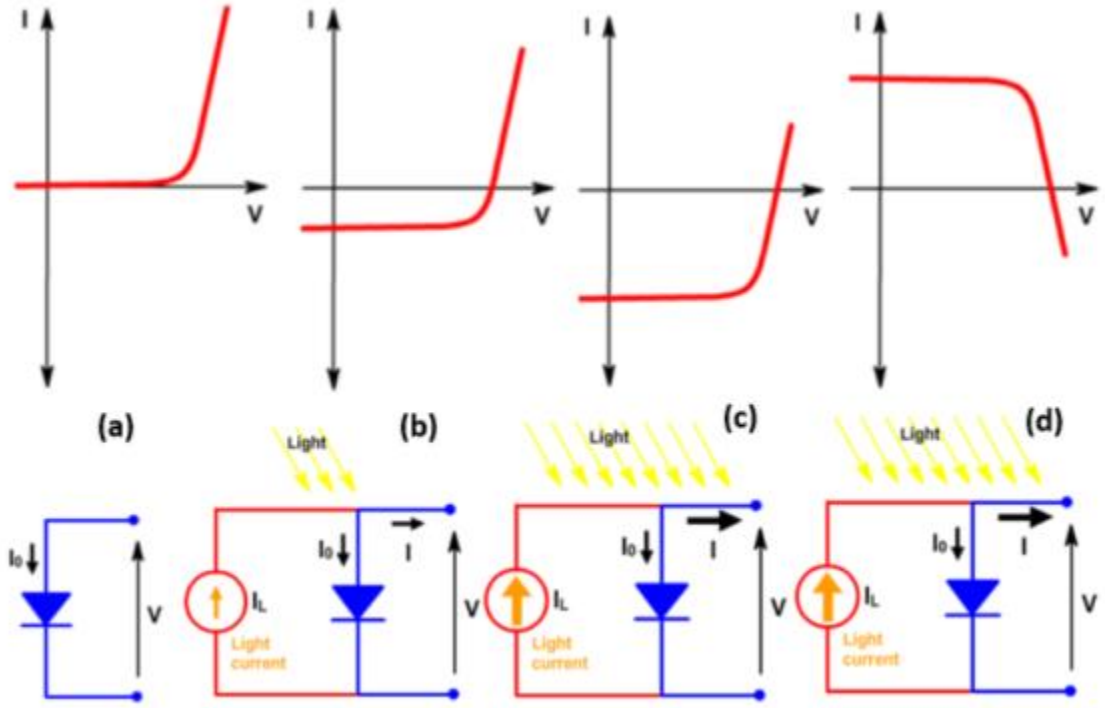

Figure 3.2: Effect of light on current -voltage characteristics and equivalent circuit. (a) Dark IV response, (b) under small illumination, (c) greater illumination, (d) conventionally inverted IV curve [1]

The IV curve possesses a wealth of information and extracts some of the most important parameters [Fig 3.2] of the solar cell [1-3]:

(a) Short Circuit Current

The short circuit current (I_{SC}) is the maximum current that can be extracted from the solar cell at 0 bias voltage. I_{SC} is dependent on charge generation and collection mechanisms in the

solar cell. Light spectrum, absorption coefficient, and thickness of the absorber material, area under illumination, and charge collection efficiency play an important role in I_{SC}. The I_{SC} of a solar cell is given by [2],

$$I_{SC} = qAG(L_n + L_p)$$

where A is the area of the solar cell, G is the generation rate, and L_n and L_p are the diffusion length of electrons and holes respectively. In an ideal case, the short-circuit current (I_{SC}) should be identical to the photogenerated current (I_L), assuming no recombination or resistive losses. The I_{SC} is also a function of the bandgap of the absorber material, with ISC decreasing as Eg increase, as less of the light spectrum is able to be harvested by the absorber.

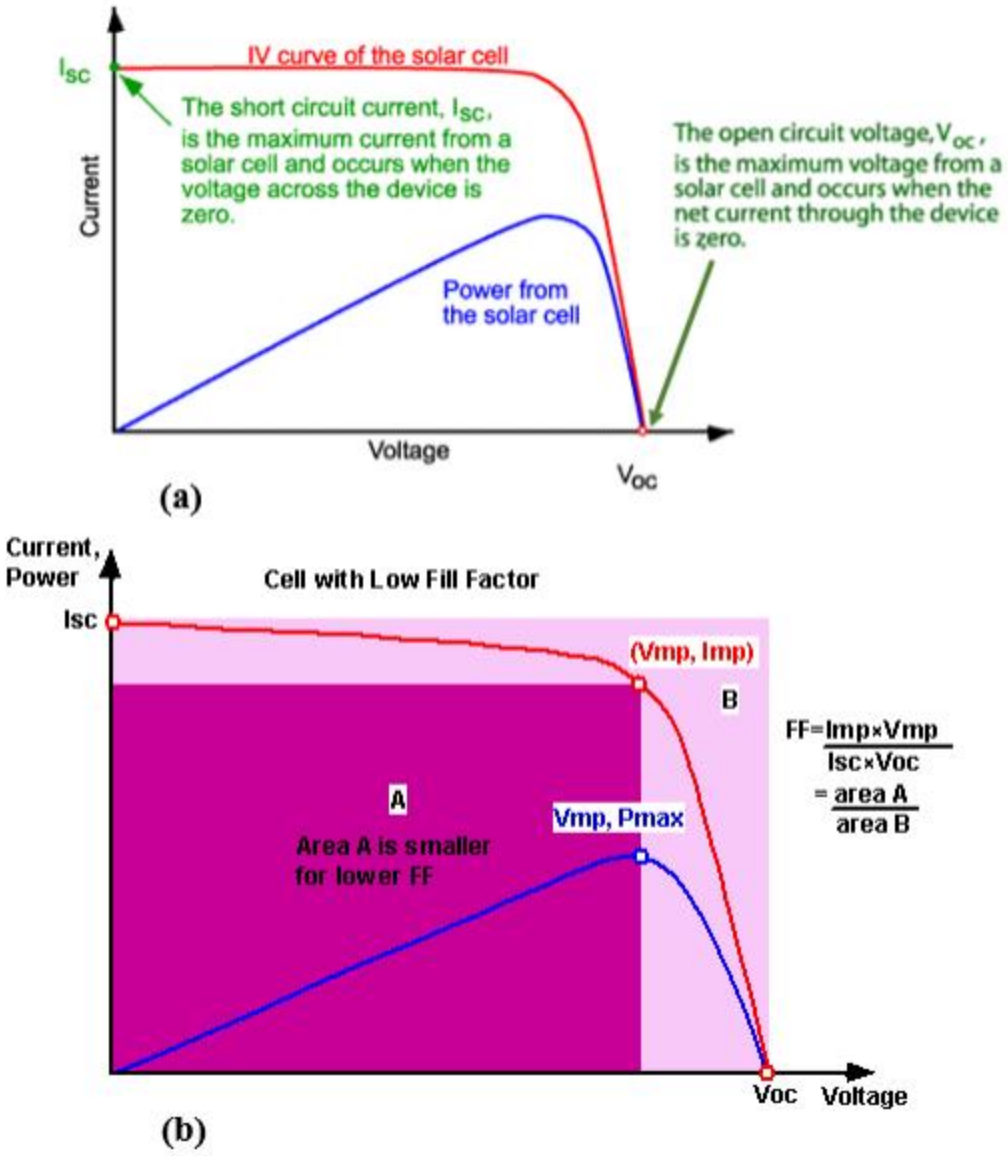

Figure 3.3: Key parameters of a solar cell from the light IV response

(b) Open-Circuit Voltage

The maximum voltage generated by the solar cell when the current through it is 0 is called the open-circuit voltage (V_{OC}). Equation 3.1.1 can be solved to express V_{OC} by

$$V_{OC} = \eta kT \ln\left(\frac{I_L}{I_0} + 1\right)$$

As the reverse saturation current (I_0) is a function of the recombination mechanisms active in the device, an implied V_{OC} can be calculated using the carrier concentrations,

$$V_{OC} = kT \ln\left(\frac{(N_A + \Delta n)\Delta n}{{n_i}^2}\right)$$

where N_A is the doping concentration. Unlike the ISC, the V_{OC} increases with increasing band gap of the absorber material.

(c) Fill Factor

The Fill Factor (FF) is defined as the ratio between the maximum power (P_{MP}) extracted from the solar cell to the product of the cell's ISC and V_{OC}. It is a measure of the squareness of the IV curve. The voltage and current at this maximum power point are defined as VMP and IMP of the cell.

$$FF = \frac{P_{MP}}{V_{OC} I_{SC}} = \frac{V_{MP} I_{MP}}{V_{OC} I_{SC}}$$

The maximum FF for a given V_{OC} is given by the empirical equation,

$$FF = \frac{v_{OC} - \ln(v_{OC} + 0.72)}{v_{OC} + 1}$$

$$v_{OC} = \frac{q}{\eta kT} V_{OC}$$

where v_{oc} is the normalized V_{OC}. Parasitic resistances significantly lower the FF from its ideal values, as will be discussed later in this chapter.

(d) Power Conversion Efficiency

The Power Conversion Efficiency (PCE) is the most important parameter in evaluating solar cells. It is the ratio of the incident light energy that is converted to usable electric energy by the photovoltaic device.

$$PCE = \frac{P_{MP}}{P_{in}} = \frac{V_{OC} I_{SC} FF}{P_{in}}$$

P_{in} is the input light energy, which is 100mW/cm^2 for the standard AM1.5 spectrum that we receive on the surface of the earth.

(e) Shunt and Series Resistance

Light IV measurements can also be used to calculate the parasitic shunt resistance (R_{sh}) and series resistance (R_s) of the solar cell. In an ideal solar cell, the series resistance is 0 and the shunt is infinitely large. However, in real cases they are not so. The series and shunt resistance can be calculated from the IV curve by measuring the slope at the open-circuit and short-circuit conditions respectively[Fig 3.4].

$$R_S = \lim_{V \to V_{OC}} \left(\frac{1}{dI/dV} \right)$$

$$R_{Sh} = \lim_{V \to 0} \left(\frac{1}{dI/dV} \right)$$

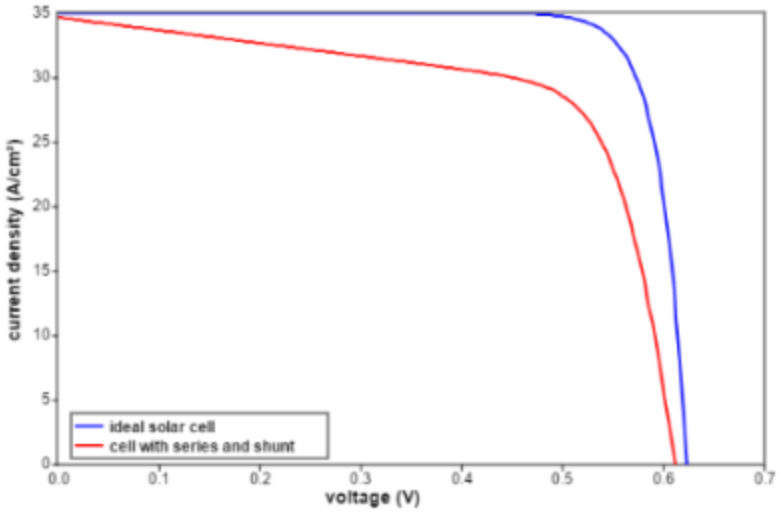

Figure 3.4: Light IV response of an ideal solar cell (blue0 and a real cell with shunt and series resistance (red)

3.1.2 Dark IV Measurements

An IV measurement conducted under no illumination is called a dark IV measurement, which are useful in understanding the contributions from the parasitic resistances and the diode currents as the smaller diode current components are not overshadowed by the large photo-generated current (I_L) in the 2 diode model of the solar cell[Fig 3.5] [3,4].

$$I = I_L - I_{01}\left[e^{\left(\frac{qV}{\eta_1 kT}\right)} - 1\right] - I_{02}\left[e^{\left(\frac{qV}{\eta_2 kT}\right)} - 1\right] - \frac{V + IR_S}{R_{Sh}}$$

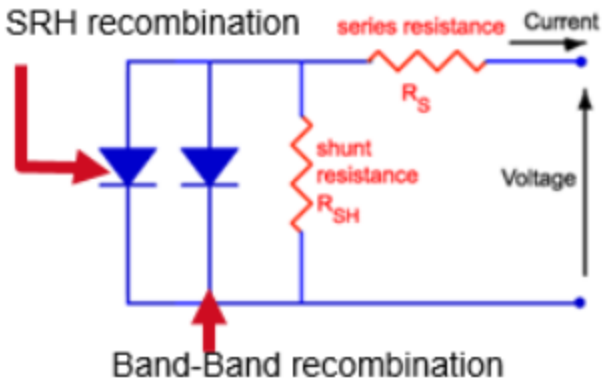

Figure 3.5: Equivalent circuit of a solar cell with the two-diode model

The dark IV curve is plotted on a semi-log scale[Fig 3.5] to understand the various contributions. At lower bias conditions (0-0.1V), the shunt current dominates, and the shunt resistance can be calculated using the slope of the IV curve here. Pin holes in the active absorber layer can create a shunt pathway in the solar cell, severely degrading device performance. As the voltage increases, the current increases exponentially. At very high bias voltages the current is dominated by the series resistance (R_{SR}), which deviates the IV curve from this exponential behavior. Ideality, factors corresponding to the two diodes in the equivalent circuit can be extracted from the IV curve in the middle region. In the standard dark IV curve from Fig XX, for example, recombination is dominated by the depletion layer at low biases (~0.4V), giving an ideality factor of 2. The reverse saturation current due to this depletion layer recombination is a function of the minority charge carriers.

At higher biases (~0.5V), as the depletion region shrinks the band-to-band recombination in the bulk dominates, leading to an ideality factor of 1. The reverse saturation current due to band-to-band recombination in the neutral region is dependent on the electron and hole mobilities.

Similarly, ideality factors can be derived for other recombination mechanisms. Auger recombination has an ideality factor of 2/3 and high carrier injection results in ideality factor of 2.

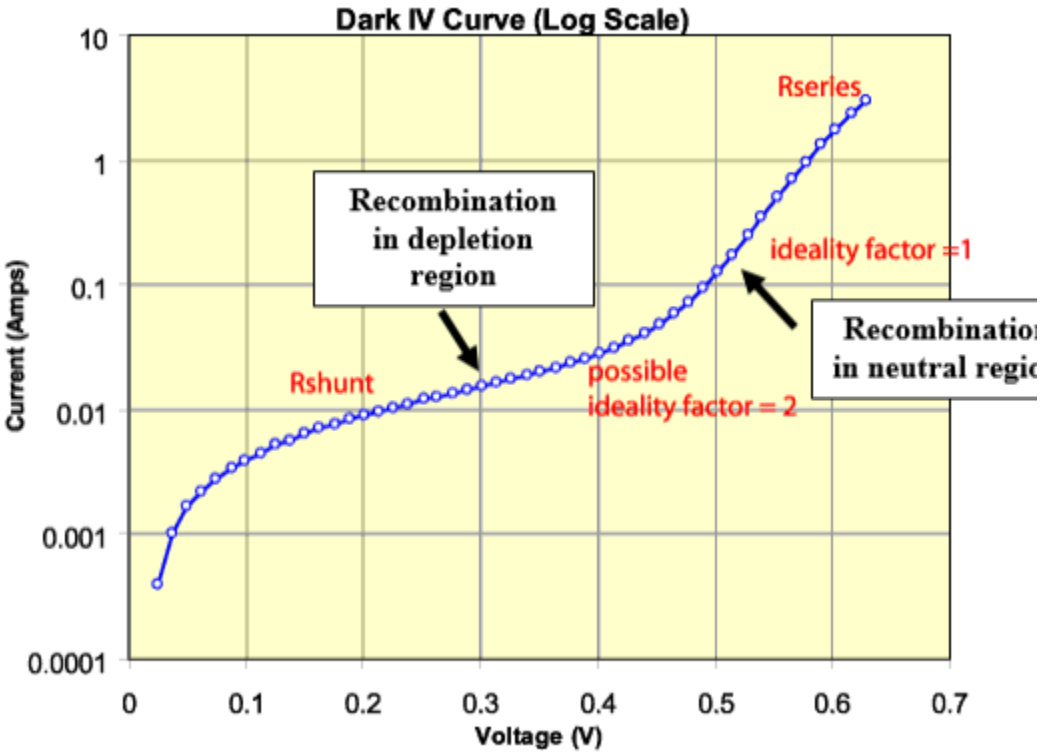

Figure 3.6: Dark IV response plotted on a semi-log scale

3.2 Quantum Efficiency

The external quantum efficiency (EQE) of a solar cell is the measure of how efficiently the solar cell is able to absorb photons and collect the separated charge carriers. The EQE is a function of the wavelength (λ) of the light and is defined as [1,5,6]

$$Esternal\ Quatum\ Efficiency(\lambda) = \frac{Number\ of\ charge\ carriers\ collected}{Number\ of\ incident\ photons}$$

The setup of the External Quantum Efficiency measurement is shown in Fig. 3.2.1. White light from a Halogen lamp is incident on a monochromator with a diffraction grating. Adjusting

the angle of incidence (θ_i), the desired wavelength is sent through the slit of the monochromator into the optical chopper, which converts the incident DC light signal into a 13Hz AC signal before the light is focused onto the Device Under Test (DUT) using a lens and mirror. Unwanted harmonics in the AC light signal are suppressed using order sorting filters. Signal from the DUT is collected and fed to a pre-amplifier. The DUT response to the chopped AC light signal is filtered from any unwanted stray light or electronic noise and interference by using a lock-in amplifier synchronized with the optical chopper. The DUT can be also be biased using a separate DC light source to measure light biased QE. A voltage source is provided to measure the QE at different voltage biases. A reference silicon diode with a known EQE at different wavelengths is used to measure the photon flux of the light beam.

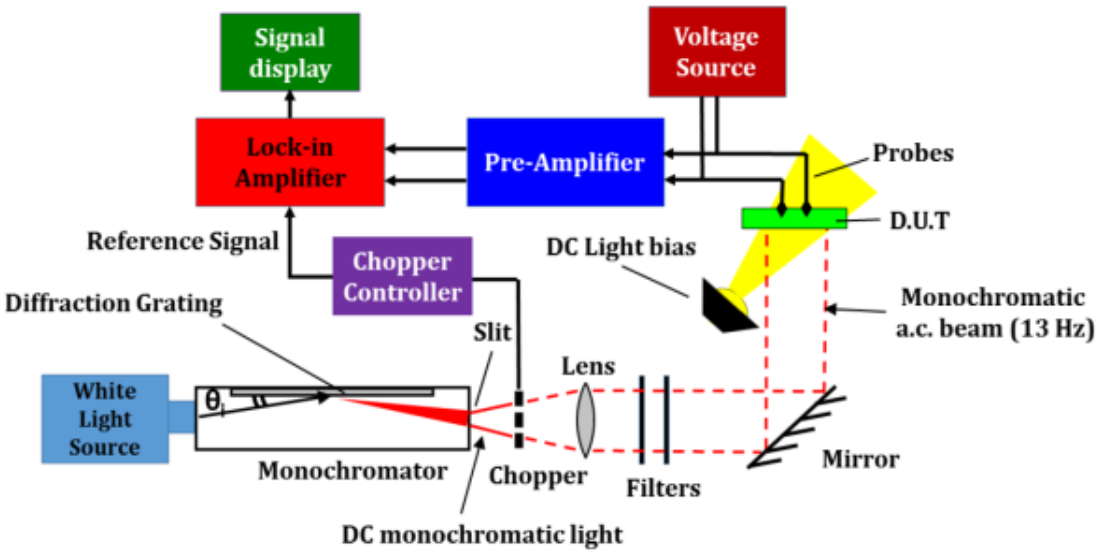

Figure 3.7: Schematic of the quantum efficiency setup

THE EQE of the DUT can be calculated by using,

$$EQE_{DUT} = \frac{Signal_{DUT}(\lambda)}{Signal_{Reference}(\lambda)} * \frac{Area_{DUT}}{Area_{Reference}} * EQE_{Reference}(\lambda)$$

The EQE of an ideal solar cell, a “real” solar cell, and possible loss mechanisms is shown in Fig 3.8. While the EQE of an ideal cell is a square shape, as shown in the figure, the EQE of most cells deviate significantly from this shape. The EQE of a solar cell includes losses due to reflection and transmission of the light. At low wavelengths (<300 nm), the high energy photons can be absorbed very easily in the glass substrate or transport layers and not reach the absorber layer. Thus, the EQE at <300nm is very low. Light of higher wavelength beyond the band gap of the absorber material cannot be collected, and as thus the EQE drops as well. Between these two regions, the EQE is affected by the various loss mechanisms in the solar cell. Blue photons with high energies, having high absorption coefficients, are collected close to the front surface of the solar cell, and recombination due to surface states near the front of the device can reduce the EQE. Red photons, with lower energy, are collected closer to the back surface of the cell and can be affected by recombination due to surface states near the back of the cell. If the thickness of the absorber layer in the solar cell is too thin enough to collect all the incident light, then the EQE drops overall. Largely, the EQE is an excellent diagnostic tool to troubleshoot the functioning of the solar cell.

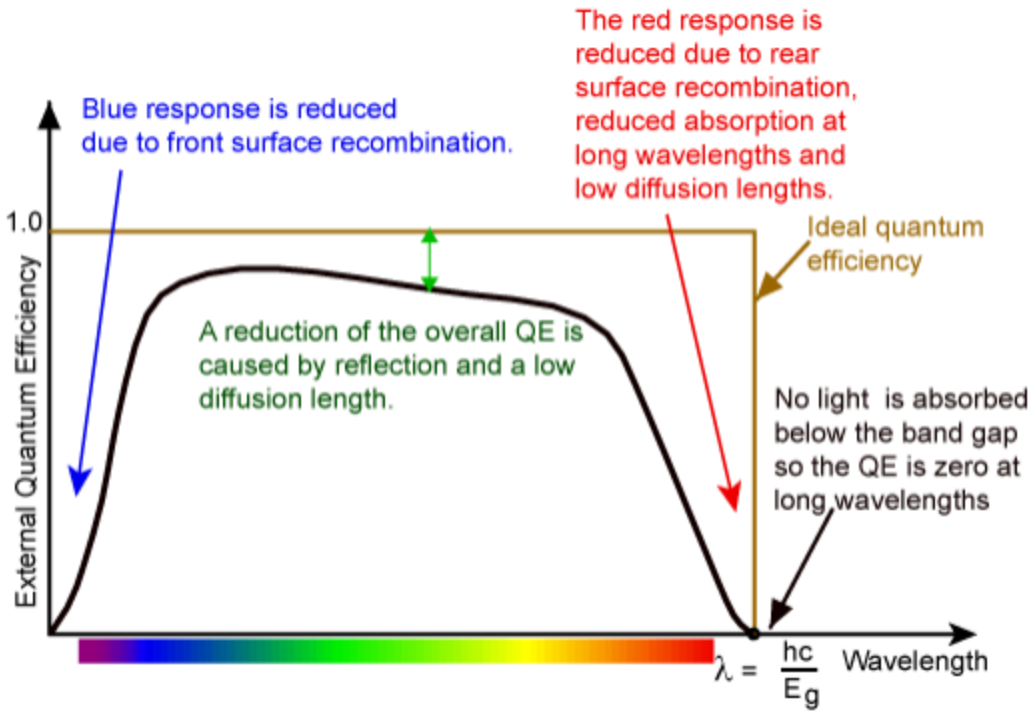

Figure 3.8: Quantum Efficiency of an ideal solar cell (yellow curve) and practical cell (black)

3.3 Sub-gap Quantum Efficiency

Fig. 3.3.1 shows the density of electronic states as function of energy in a semiconductor with electronic disorder. The valance and conduction bands are separated by an energy gap. Tail states from the conduction and valence bands extend into the band gap and exponentially fall off with distance from band edges. Also present are mid-gap states with a Gaussian distribution of densities. The mid-gap and tail states are responsible for parasitic recombination pathways, which reduce the device performance; understanding of their distributions and energies are critical to optimize device performance. These mid gap and tail state defects are responsible for sub-band gap absorption and they can be quantified with the help of the sub-gap QE measurement [7].

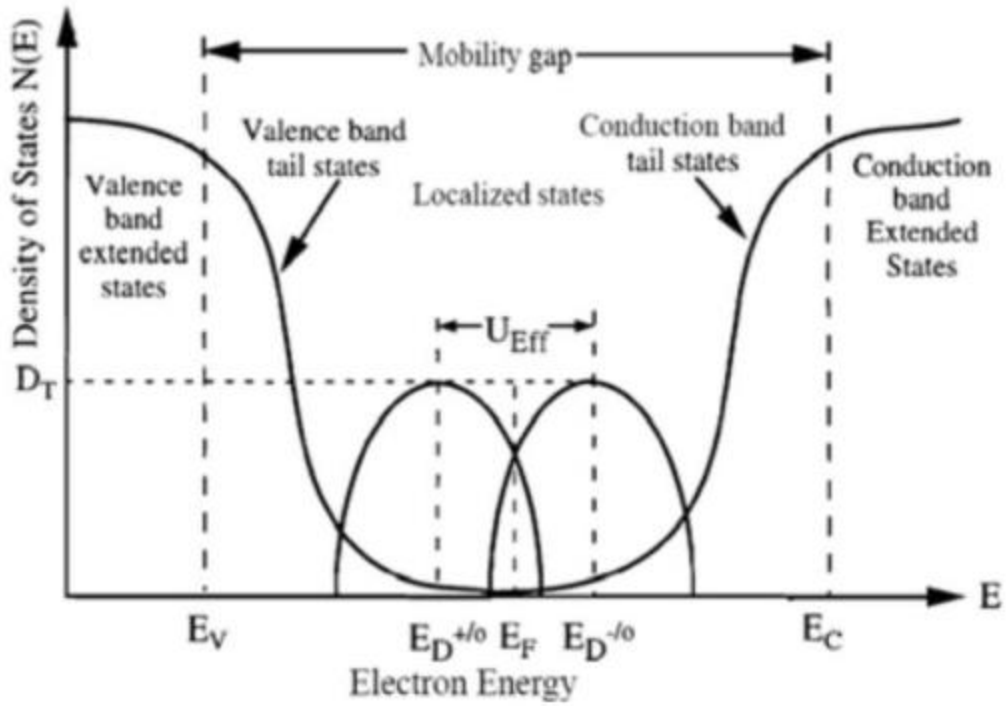

Figure 3.9Density of states in a semiconductor with crystal disorder. Tail states are exponentially distributed, and mid gap states are normally distributed [7]

Fig. 3.3.2 shows the typical sub-gap QE of a perovskite solar cell with an energy band gap of 1.6eV. Below the band gap of the material, the QE falls exponentially. As detailed in Section 2.1, the sub-band gap absorption due to tail states are described by

$$\alpha = Ae^{\left(\frac{(h\vartheta)}{E_U}\right)}$$

where the Urbach energy, E_U, is a measure of the breadth of the density of tail states. The Urbach energy of the tail states can be calculated from the slope of the QE curve in this regime. A lower Urbach energy corresponds to a sharper fall in the density of tail states, which usually implies the higher crystallinity of the material grown. At lower energies, the sub-gap absorption results from transitions through the mid-gap states of the material and the sub QE plateaus.

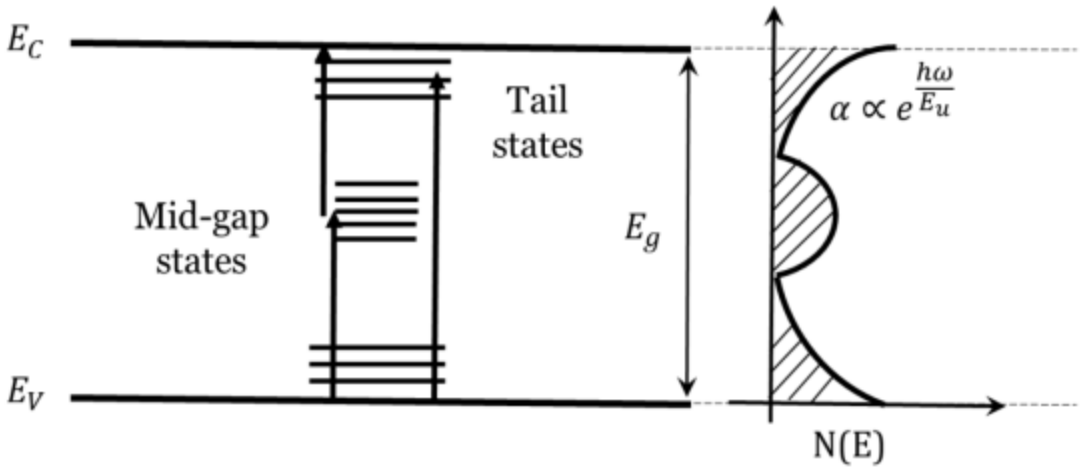

Figure 3.10: Transition through defect states (left) and distribuition of defect states (right)

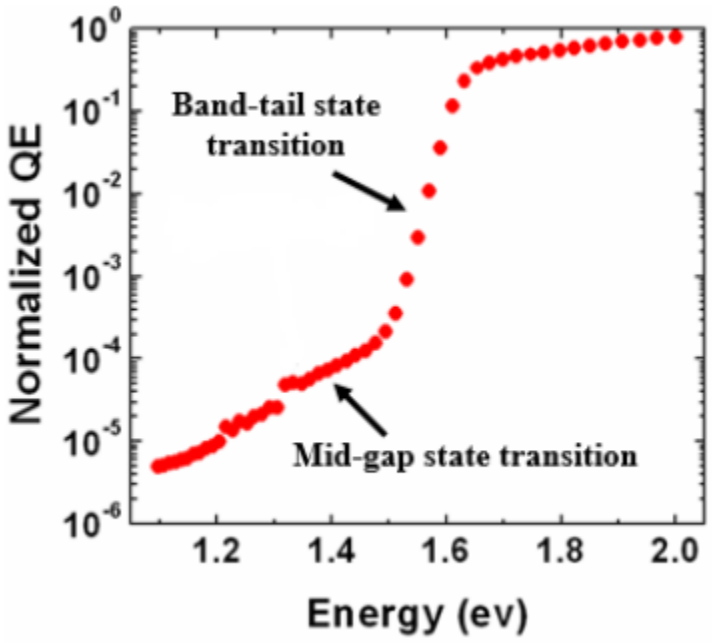

Figure 3.11 Sub-band QE of a typical perovskite solar cell [3]

3.4 Capacitance-Voltage measurement

Capacitance-Voltage(CV) measurements are used to determine the dopant density and depletion layer width of the solar cell. Fig. 3.4.1 shows the band diagram of a Schottky junction under depletion. E_C , E_V, and E_F represent the conduction band, valence band, and Fermi level

respectively. The depletion width (W_d) and junction capacitance (C) of this one-sided ($n^+|p$) junction is given by [2]

$$W_d = \sqrt{\frac{2\epsilon(V_0 - V)}{qN_A}}$$

$$C = \frac{A\,\epsilon}{W_d} = A\sqrt{\frac{q\epsilon N_A}{2(V_0 - V)}}$$

where V_0 , V are the built-in voltage, and voltage applied to the solar cell and N_A is the dopant density of the lightly doped p side. Simplifying,

$$\frac{1}{C^2} = \frac{2}{q\epsilon N_A A^2}(V_0 - V)$$

Thus, by plotting $1/C^2$ vs V, we can extract the dopant density (N_A), the built-in voltage(V0) of the solar cell as seen in Fig. 3.4.2

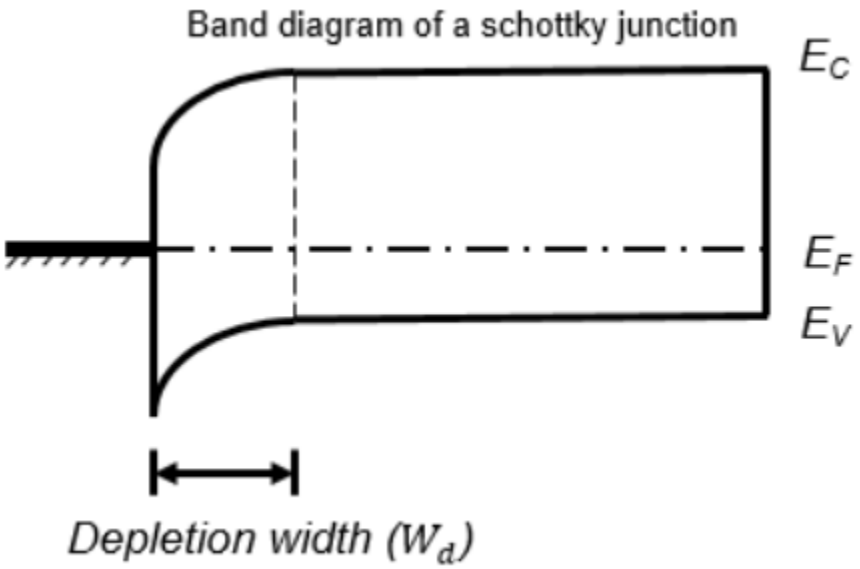

Figure 3.12: Band diagram of a Schottky pn junction

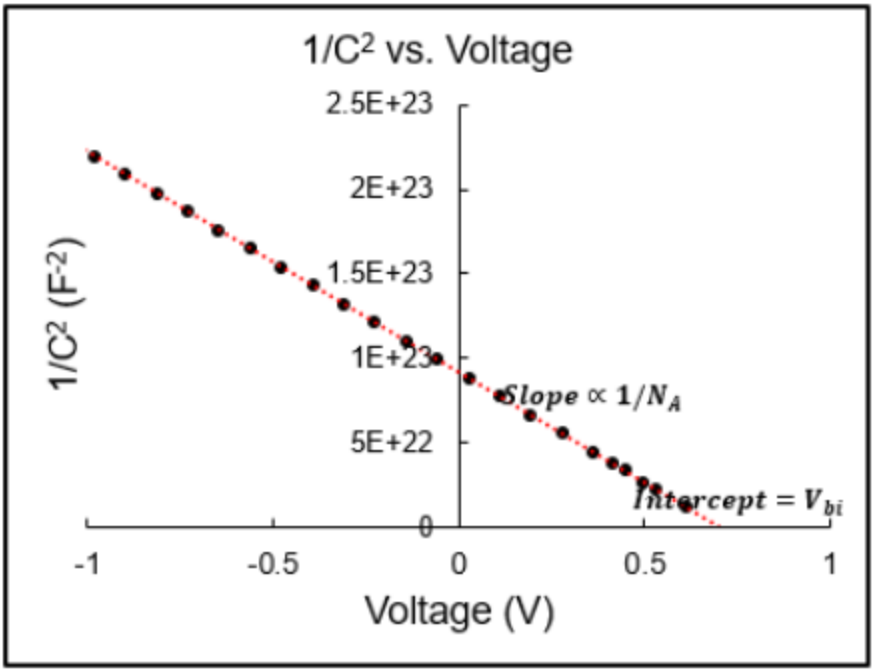

Figure 3.13: Ideal capacitance-voltage profile of a one-sided pn junction

3.5 Capacitance Frequency measurement

The energetic distribution of trap states in the solar cell can be obtained by measuring the Capacitance as a function of frequency. The Capacitance-frequency(C-f) measurement technique is based on the fact that the emission rate of an electron from a trap state at an energy level (E_T) within the band-gap of the material is given by [2,10,11],

$$e_n = \upsilon_0 e^{-\left[\frac{E_C - E_T}{kT}\right]}$$

where e_n is the emission rate of electrons to the conduction band from the trap state and ν_0 is the attempt-to-escape frequency. Most importantly, the emission rate is an exponential function of the depth of the traps in which they are trapped.

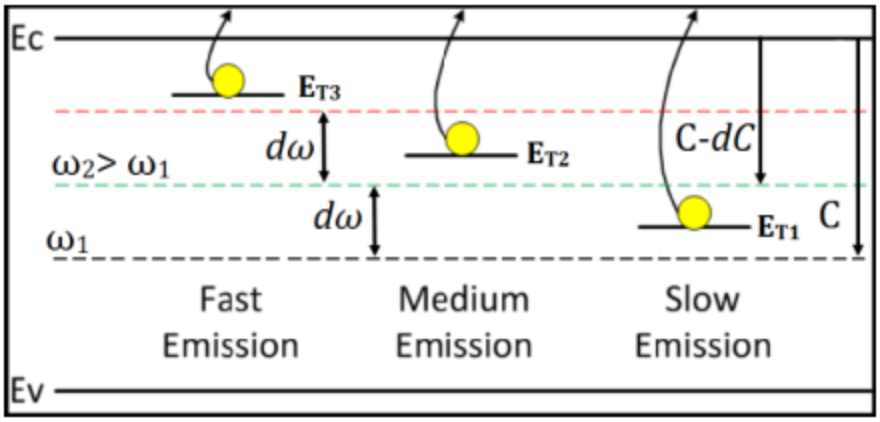

Figure 3.14: Emission rates of traps dependent on their depth in the band gap

Under an AC bias, the trapped electrons in the defect states can follow the signal depending on the emission rates and the frequency of the signal applied. Shallow traps with a faster emission rate can respond to high frequency signals. Deeper traps with a slower emission rate can only respond to lower frequency signals and not to high frequency signals, as shown in Fig. 3.5.1. By sweeping the frequency of the AC signal and measuring the capacitance at each frequency, the density of deep states can be calculated by,

$$N_T(E_\omega) = -\frac{V_0}{qW_d}\frac{dC}{d\omega}\frac{\omega}{kT}$$

where the angular frequency of the applied signal is given by, $\omega = 2\pi f$. The demarcation energy, E_ω, is given by,

$$E_\omega = \frac{kT}{q}\ln\left(\frac{\omega}{\omega_0}\right)$$

where the angular ATEF ω_0 is given by

$$\omega_0 = 2\pi\upsilon_0$$

$$\upsilon_0 = N_C\upsilon_{th}\sigma_n$$

where N_c is the effective density of states, ν_0 is the ATEF, ν_{th} is the thermal velocity, and σ_n is the electron capture cross section of the trap.

Quite simply, when probed at a certain frequency (ω) the traps at energies below the demarcation energy (E_ω) are able to respond and contribute to the capacitance, while traps deeper than E_ω are unable to respond and do not contribute to the capacitance. Reducing the frequency of the applied AC signal allows deeper traps to respond and will increase the measured capacitance. A typical Cf response curve and the calculated density of deep states is shown in Fig. 3.5.2

Another implication of equation, 3.5.1 is that higher temperatures are able to activate deeper traps to emit electrons. This fact is leveraged by the Capacitance-frequency-Temperature measurement technique to extend the energy window in which the traps could be characterized. Calculating the density of deep defects in each energy window and overlaying the results yield the energetic distribution of the trap states over a large window. Further, the CfT technique can be used to determine the ATEF and activation energy of the trap states.

As both the effective density of states ($N_c \sim T^{3/2}$) and the thermal velocity ($\nu_{th} \sim T^{1/2}$) are proportional to temperature, the ATEF is a function of temperature as well ($\nu_0 \sim T^2$). The equation 3.5.1 can be expressed as

$$\ln\left(\frac{e_n}{T^2}\right) = \ln(\xi) - \frac{E_A}{kT}$$

where the activation energy, $E_A = E_C - E_T$ and ξ, is a proportional constant. Thus, by measuring C-f at multiple different temperatures and plotting $\ln\left(\frac{e_n}{T^2}\right)$ vs $\frac{1}{kT}$ we can determine both the activation energy of the traps as well as the ATEF. Fig. 3.5.3 shows the Capacitance-frequency data captured at multiple different temperatures and displayed as $-f\frac{dC}{df}$ vs f. The

capacitance increases with temperature as the emission rates increase and deeper traps contribute. The peaks of the $-f\frac{dC}{df}$ vs f correspond to the emission rates at the different temperatures. The peaks from the plot are extracted and plotted as $\ln\frac{f_{peak}}{T^2}$ vs $\frac{1}{kT}$, which give us the activation energy of the two traps as 0.66eV and 0.24eV below the conduction band. ATEF of the dominant trap is calculated to be $2x10^{-11}$Hz from the intercept of the plot.

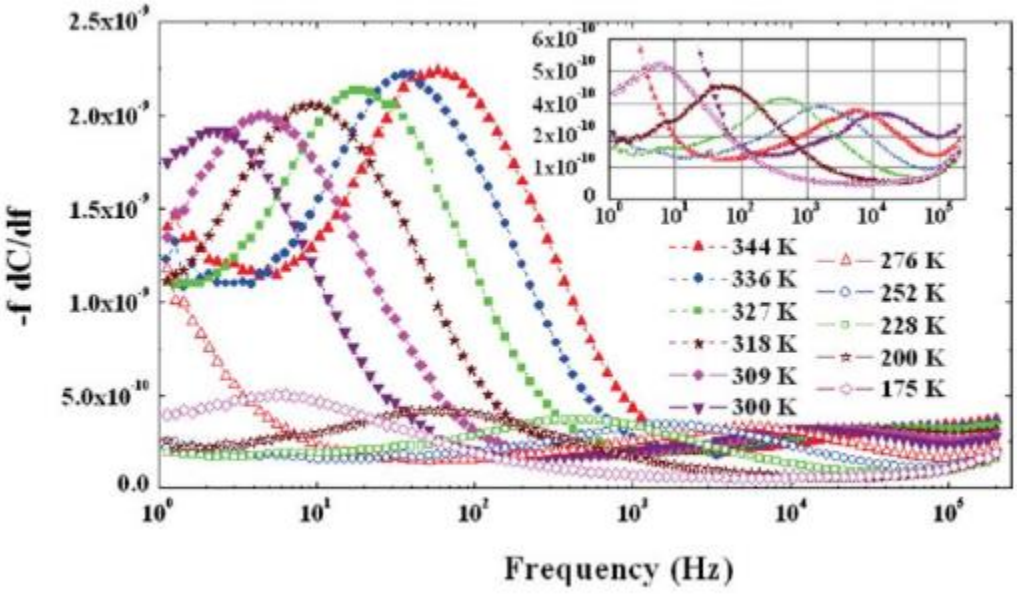

Figure 3.15: Capacitance frequency plotted as $-f\frac{dC}{df}$ vs f for a perovskite solar cell [15]

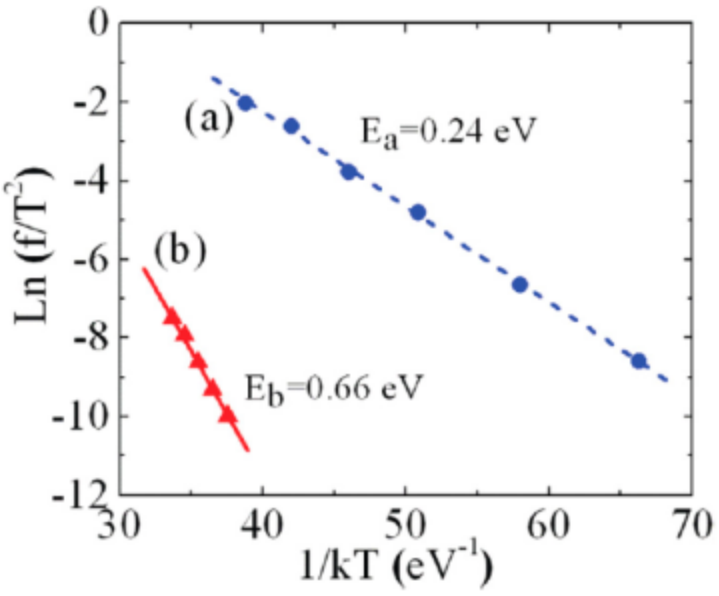

Figure 3.16: Arrhenius plot of peak frequencies as a function of temperature [15]

References

1. PV Education
   Link: http://www.pveducation.org

2. B. G. Streetman and S. K. Banerjee, Solid state electronic devices. (Pearson Education, New Jersey, 2006), 6th edition

3. Pranav Joshi, Ph.D. dissertation, “Understanding the photostability of perovskite solar cell”, Iowa State University (2016)

4. Liang Zhang, Ph.D. dissertation, “Device physics of perovskite solar cells”, Iowa State University (2016)

5. Mehran Samiee, Ph.D. dissertation, “Device physics of organic and perovskite solar cells”, Iowa State University (2015)

6. 3 F. A. Lindholm, Fossum, J. G., and Burgess, E. L., “Application of the superposition principle to solar-cell analysis”, IEEE Transactions on Electron Devices, vol. 26, pp. 165–171,1979

7. R. A. Sinton and Cuevas, A., “Contactless determination of current–voltage characteristics and minority-carrier lifetimes in semiconductors from quasi-steady-state photoconductance data”, Applied Physics Letters, vol. 69, pp. 2510-2512, 1996

8. M. A. Green, “Solar cell fill factors: General graph and empirical expressions”, Solid State Electronics, vol. 24, pp. 788 - 789, 1981

9. E. A. Davis and N. F. Mott, "Conduction in non-crystalline systems v. Conductivity, optical absorption and photoconductivity in amorphous semiconductors", Phil. Mag., 22, 903 (1970)

10. S. John et. al., “Theory of electron band tails and the Urbach optical absorption edge”, Vol.57, No. 14, 1986, pp. 1777-1780.

11. L. C. Kimerling, "Influence of deep traps on the measurement of free-carrier distributions in semiconductors by junction capacitance techniques", J. Appl. Phys., 45, 1839 (1974). doi:10.1063/1.1663500

12. T. Walter, R. Herberholz, C. Müller, and H. W. Schock, "Determination of defect distributions from admittance measurements and application to cu(in,ga)se2 based heterojunctions", J. Appl. Phys., 80, 4411 (1996). doi:10.1063/1.363401
13. D. K. Schroder, Semiconductor material and device characterization. (Wiley-IEEE Press, New York, 2015), 3rd edition

14. R. F. Pierret, Advanced semiconductor fundamentals. (Addison-Wesley Publishing Company, Reading, 1987).63

15. Mehran Samiee, Siva Konduri, Balaji Ganapathy, Ranjith Kottokkaran, Hisham A. Abbas, Andrew Kitahara, Pranav Joshi, Liang Zhang, Max Noack, and Vikram Dalal "Defect density and dielectric constant in perovskite solar cells", APPLIED PHYSICS LETTERS 105, 153502 (2014)

CHAPTER 4. PEROVSKITE SOLAR CELLS

4.1 Introduction

Perovskites are a class of materials with the crystal structure ABX_3, named after the Russian mineralogist Lev Perovski. The first perovskite materials, Calcium titanate ($CaTiO_3$) were discovered in the Ural Mountains by Gustav Rose in 1839. Perovskites have a general crystal structure of ABX_3 where A and B are cations of different sizes and X is the anion that binds the structure together [1]. A cation and B cation have +1 and +2 electron vacancy respectively. Fig. 4.1 shows the general lattice structure of the perovskite crystal.

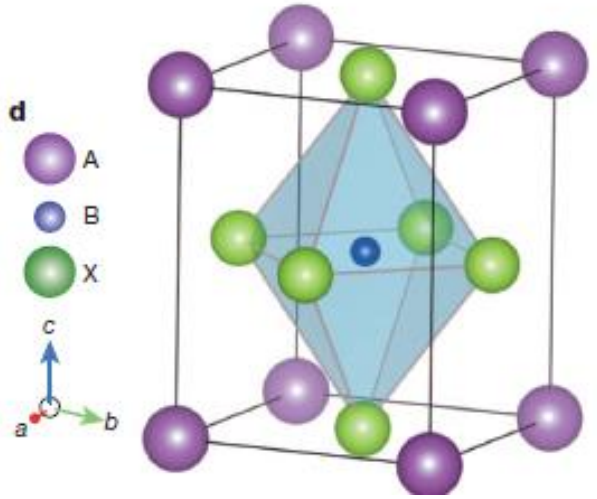

Figure 4.1: General crystal structure of ABX_3 perovskite

For the formation of the perovskite crystal structure, the ionic radii must follow certain tolerance and octahedral factors.

To form a cubic perovskite crystal structure [2], the perovskite material must conform to:

$$\text{Goldschmidt Tolerance Factor}, t = \frac{r_A + r_X}{2\sqrt{(r_B + r_X)}}$$

$$0.81 < t < 1.11$$

$$Octahedaral\ Factor, \mu = \frac{r_B}{r_X}$$

$$0.44 < \mu < 0.9$$

where r_A, r_B and r_X are the ionic radii of the A cation, B cation, and the X anion respectively.

A wide variety of materials satisfy the necessary tolerance and octahedral factors required to form perovskite materials. The A cation can be an organic cation, such as the widely used Methylammonium (MA) or the less common Ethylammonium (EA) or Formamidinium (FA) or even an inorganic cation such as Cesium (Cs). The B cation can be Lead (Pb) or Tin (Sn) and the X anion can be halides like Iodine(I), Bromine (Br), or Chlorine (Cl). Further, any combination of the A and B cations and X halides can form perovskites as long as they satisfy the tolerance and octahedral factors.

4.2 Perovskite Solar Cells: A short history

The use of perovskites as active layers in LEDs and thin-film transistors predates the use of perovskites in photovoltaics[3-5]. Tsutomu Miyasaka and colleagues in Japan are credited with the first such utilization of perovskites in photovoltaics, having utilized organic inorganic lead halide perovskites as light absorbers in dye-sensitized solar cells in 2006 [6]. They used methylammonium lead bromide ($MAPbBr_3$) to achieve a power conversion efficiency of 2.2% and later topped it with a methylammonium iodide ($MAPbI_3$) solar cell with an efficiency of 3.3% [6]. Park's research group was able to improve the efficiency by depositing perovskite on Titanium dioxide (TiO_2) nanoparticles to achieve efficiencies of 6.5% [7]. Gratzel and Park further optimized perovskite efficiencies using spiro-MeOTAD as a hole transport layer to achieve 10.9% efficiency [8]. Sequential solution deposition technique was used independently by Gratzel and Snaith to surpass 15% efficiencies in 2013 [9]. Snaith reported the first vapor

deposited perovskites in 2013. Currently, the efficiency of perovskite solar cells (PSC) surpass more established photovoltaic technologies like Cadmium Telluride (CdTe) and Copper Indium Gallium Selenide (CIGS), while still lagging Silicon photovoltaics. The record efficiency for a single junction perovskite solar cell, reported from the Chinese Academy of Sciences and certified by the National Renewable Energy Laboratory in 2018, stands at 23.7% [10].

Tandem structures of perovskite with other photovoltaic technologies have also displayed remarkable progress with the Oxford PV, showing 28.0% efficiency for a monolithic perovskite/Si tandem cell.

4.3 Properties of Perovskite

The perovskite material possesses several properties that make it an attractive candidate for the absorber material in a solar cell:

1. Perovskites have high absorption coefficients in the order of 10^{-5}-10^{-6} cm^{-1}. This makes them ideal candidates for thin film solar cells where only a relatively thin layer (100nm-1000nm) is enough to capture most of the incident photons.
2. Perovskite band gaps can be tailored by changing the relative compositions of the halides. For example, in the case of $MAPbI_{3-x}Br_x$, Hole et al. showed that the band gap can be varied from 1.55eV to 2.2eV by changing the fraction of Iodine in the material [Fig 4.2]. This enables the use of perovskite either as single junction solar cells with a small band gap, or tailor a larger band gap to be utilized as top cells in tandem junctions, or simply to capture UV radiation [11].
3. Perovskite materials have a large diffusion length, enabling efficient charge collection with little recombination. Several groups have reported diffusion lengths in excess of 1 micron[12-14].

4. Perovskite materials have been reported to possess low Urbach energies and low density of mid gap defects [15].
5. Perovskite materials have high dielectric constant, which ensures the exciton binding energies are lower than the thermal energy at room temperature. $MAPbI_3$ has been reported to have a dielectric constant of 60 and a corresponding exciton binding energy of 0.6 meV, much lower than the thermal energy at room temperature [16]. Thus, the electron hole pairs generated are free to be separated and collected without the need for heterojunctions to separate them.
6. The conduction band and valence band of perovskite materials match a wide variety of materials that can be used as hole transport and electron transport layers [17].
7. Perovskite materials are cheap to fabricate. The precursor materials required for perovskites—such as lead iodide, lead bromide, methylammonium iodide, and formamidinium iodide—are relatively inexpensive and easily accessible.
8. Perovskite materials are structurally flexible and can be incorporated on bendable substrates.
9. Most importantly, the electrical and optical properties of perovskites are tunable by varying their compositions.

Despite these attractive properties, there are certain challenges with perovskite materials that need to be addressed before perovskite solar cells become a candidate for commercial deployment in real world conditions. Several of these challenges are explored in the next section.

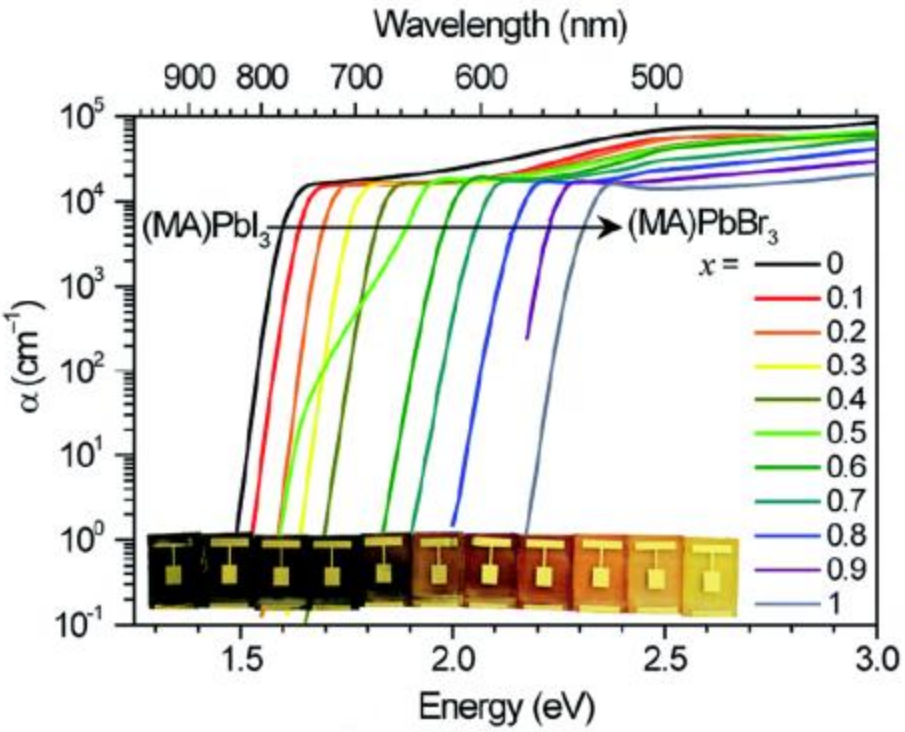

Figure 4.2: Absorption Spectra of $MAPb(I_{1-x}Br_x)_3$ as a function of the iodine fraction (x) [11]

4.4 Challenges with perovskite materials

Most of the current research on perovskite solar cells is based on methylammonium iodide-based hybrid organic-inorganic lead halide solar cells. There are some interesting challenges when working with these perovskites, as detailed below.

4.4.1 Thermal Stability

The material $MAPbI_3$ is not thermally stable. $MAPbI_3$ decomposes into MAPbI and PbI_2 above 85°C [18]. This degradation is accompanied by the release of gases via simple sublimation or assisted chemical reactions. The first step in such a thermal degradation is

$$CH3NH3PbI_3 \rightarrow NH3 + CH3I + PbI_2$$

$$CH3NH3I \rightarrow NH3 + CH3I$$

Conings et al. showed the thermal degradation of solution grown $MAPbI_3$ using an ITO/TiO2/$MAPbI_3$ structure under thermal stress at 120°C for over 10 hours. [Fig. 4.3]. Over time, the peaks corresponding to $MAPbI_3$ disappear as the material decomposes to PbI_2.

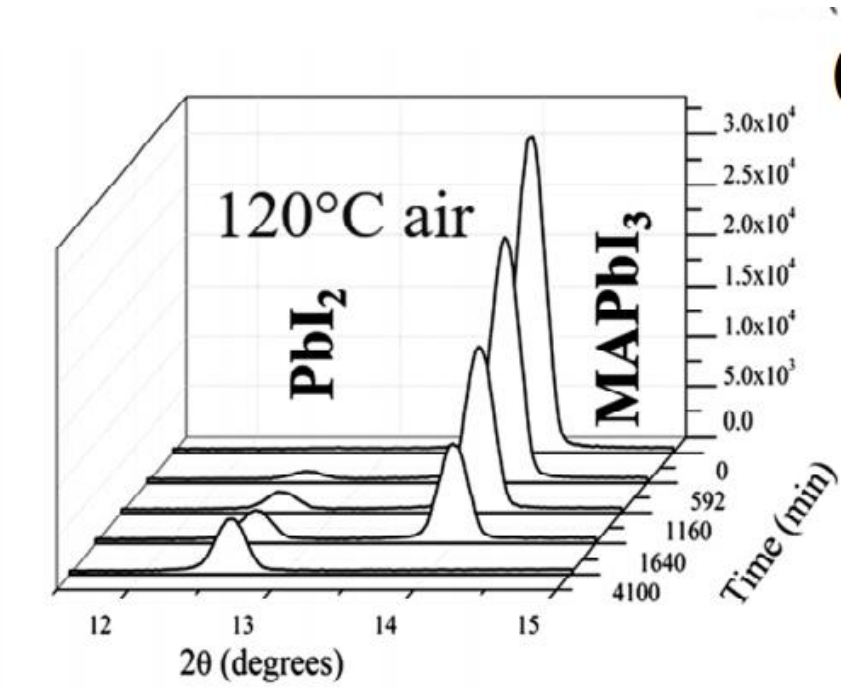

Figure 4.3: XRD spectrogram of $MAPbI_3$ undergoing thermal degradation at 120°C in air [18]

Further, Kottokkaran et al. showed the thermal decomposition of vapor deposited $MAPbI_3$ at 100°C over 24 hours [Fig. 4.4] [19]

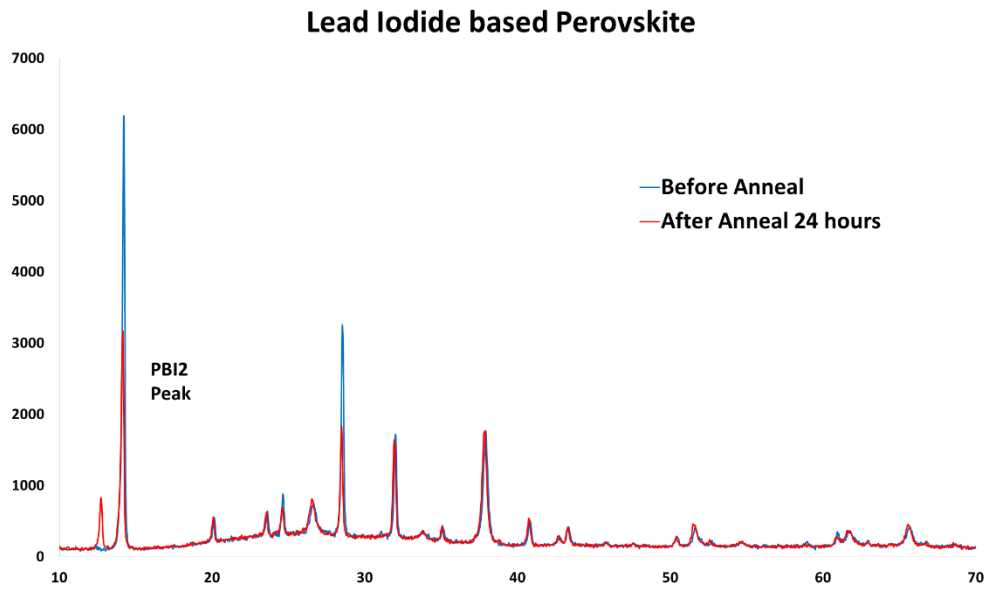

Figure 4.4: XRD analysis of thermal degradation of $MAPbI_3$ at 100°C in nitrogen ambient [19]

Xu et al. showed the thermal degradation in $MAPbI_3$ solar cells under 110°C for 1hr in a nitrogen ambient. The solar cells suffered as much as 30% efficiency losses in 1 hour of thermal stressing at 110°C [Fig 4.5] [20].

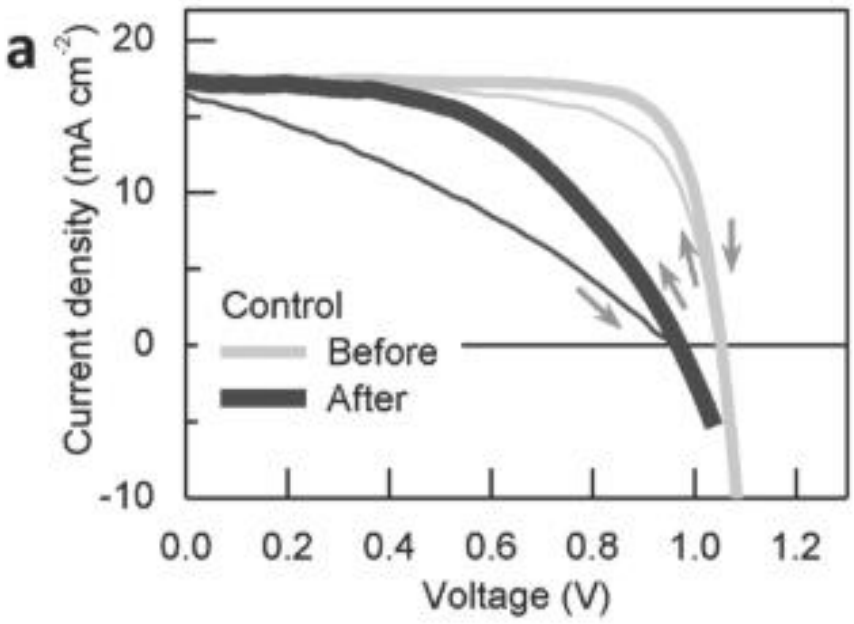

Figure 4.5: JV curves of $MAPbI_3$ solar cells before and after thermal degradation at 110°C for 1 hours [18]

Similarly, another commonly used perovskite material, $FAPbI_3$, undergoes thermal degradation at slightly higher temperatures of 125°C over 24 hours [Fig. 4.6] [19].

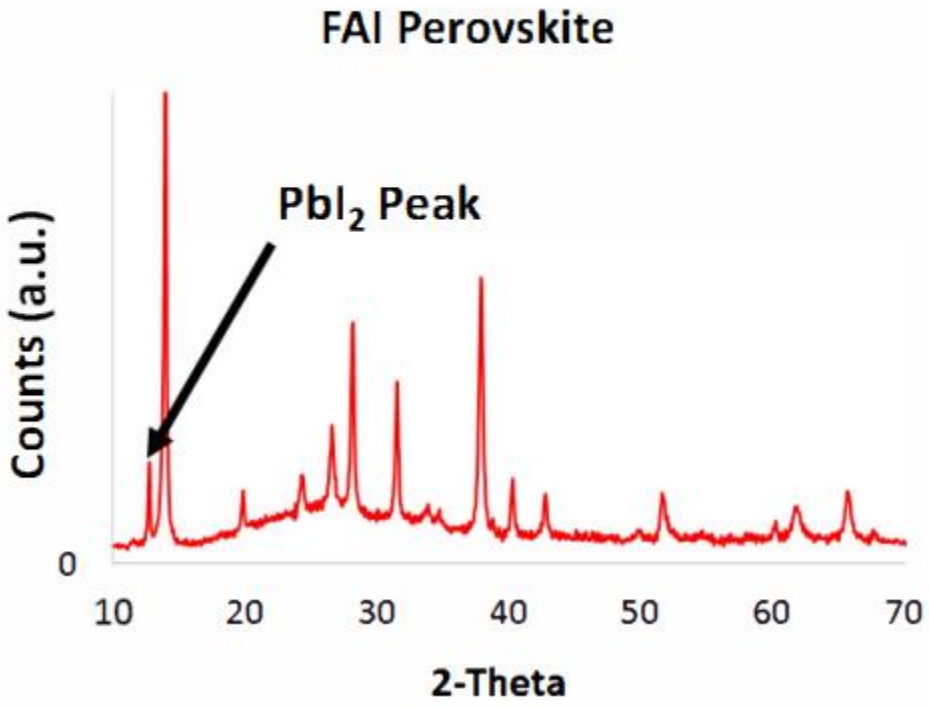

Figure 4.6: XRD analysis of thermally degraded $FAPbI_3$ at 125°C in nitrogen ambient

Fig.4.7 shows a solar resource map of the photovoltaic power potential of the whole world. Areas with the highest photovoltaic potential (highlighted by black ovals in figure) such as the

Southwestern United States, Chile, Northern Africa, the middle east, and Australia, also experience some of the highest ambient temperatures up to 50°C at peak intensities.

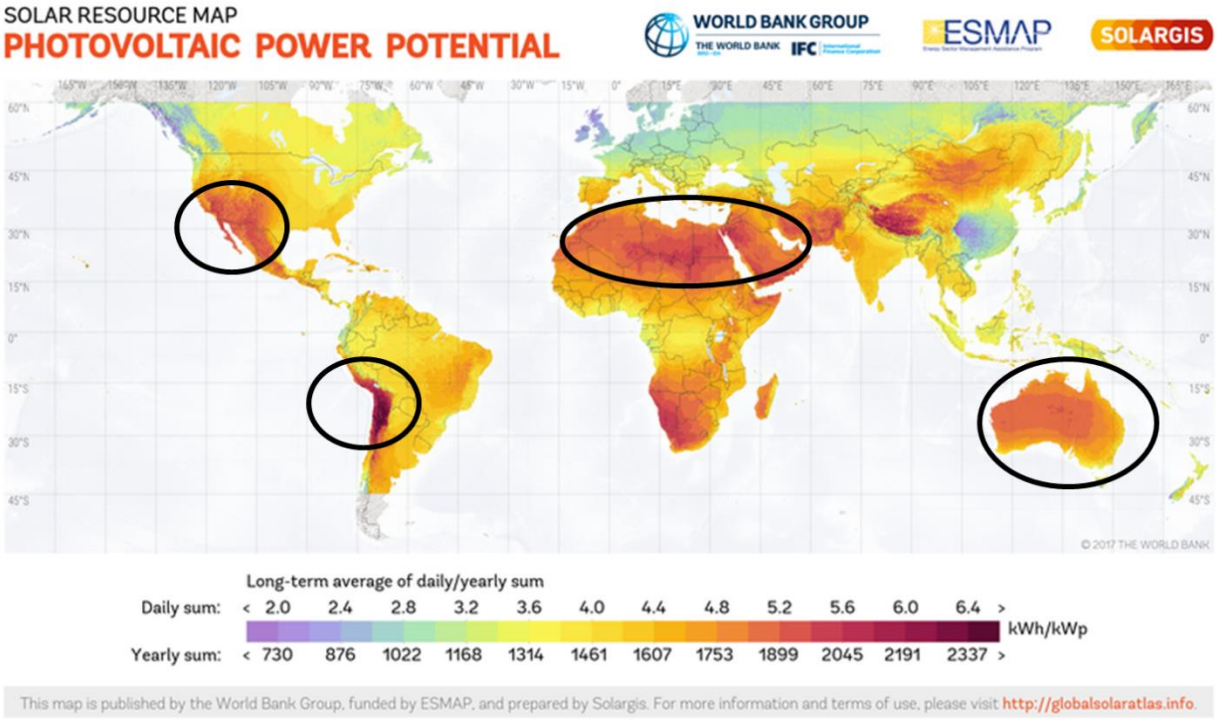

Figure 4.7: Photovoltaic power potential of the world

Garcia et al. have shown through simulations that module temperatures of even un-encapsulated solar cells are up to 40 °C higher than ambient temperatures in areas with high solar illuminance

[Fig 4.8] [21].

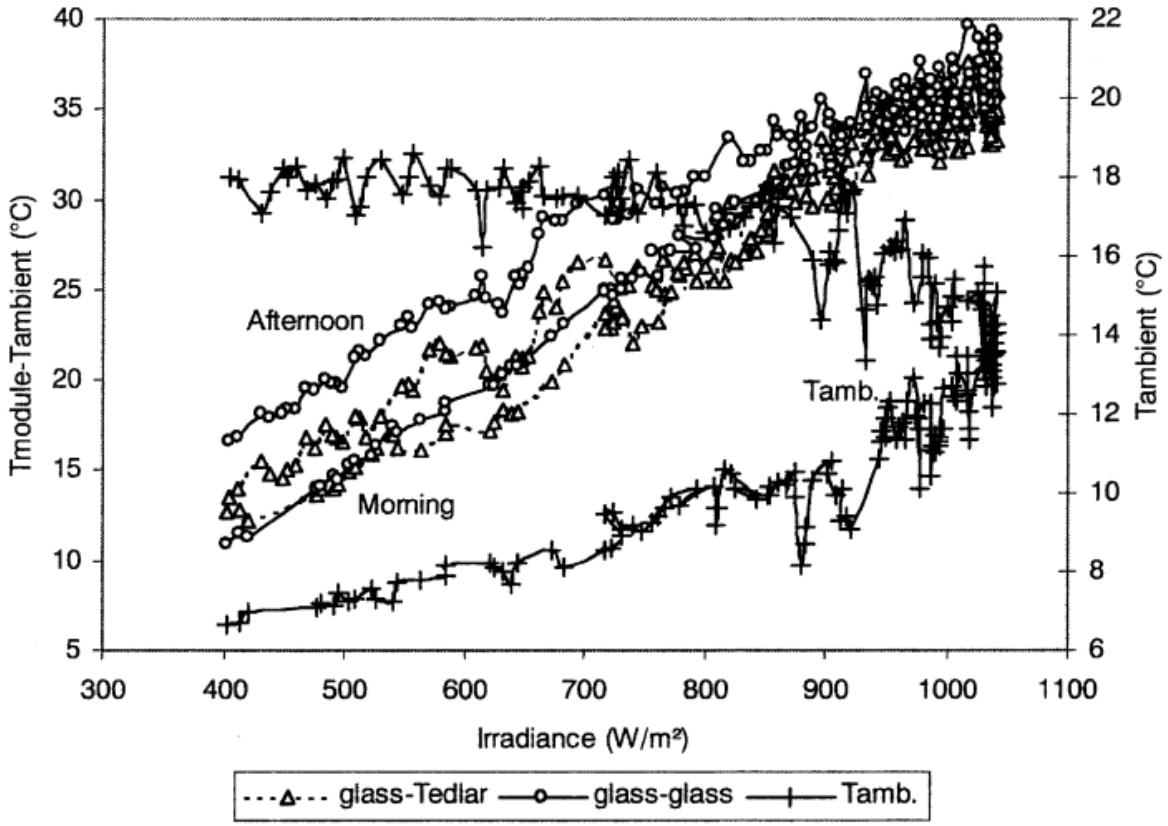

Figure 4.8: Simulations of module temperatures as a function of ambient temperature and solar irradiance

Results from field tests in the desert state of Rajasthan in India show that the temperature of solar modules under direct solar illumination exceed 85°C [23]. Besides thermal stresses during deployment, the solar cells must also endure high thermal stresses during fabrication and encapsulation. Perovskite materials being sensitive to moisture, must be encapsulated to prevent ingress of moisture. These encapsulation procedures often need to be conducted at high temperatures. In conclusion, the thermal stability of perovskite materials is a critical problem that must be resolved for deployment in real-world conditions.

4.4.2 Environmental Stability

Perovskite materials are sensitive to moisture. In 2016, Zhao et al. explained the perovskite degradation process in the presence of moisture [24]. Redox reactions are key to this degradation process with metal contacts acting as a catalyst in this process. Fig. 4.9 explains the redox reaction in detail.

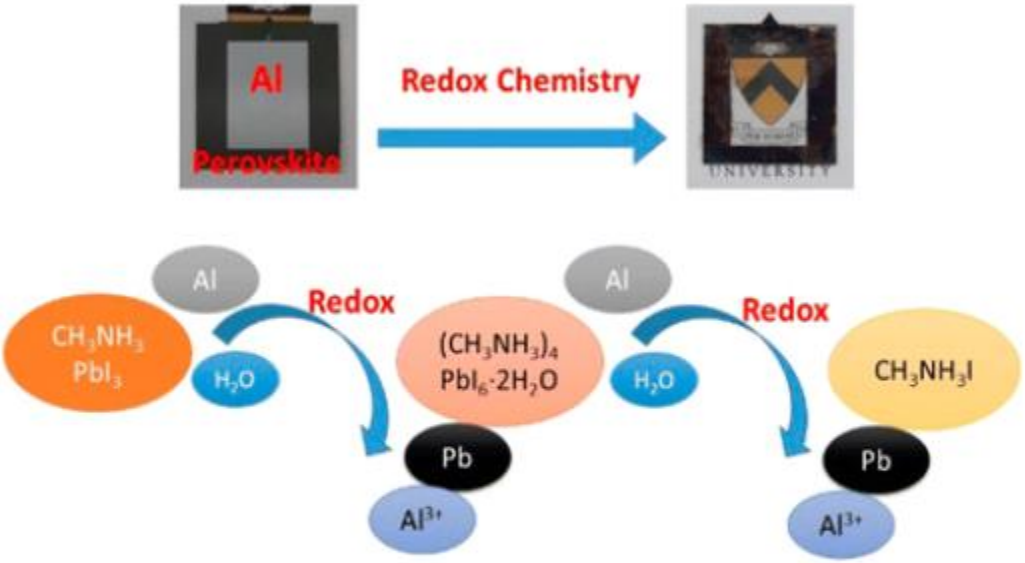

$$2Al + 4(MA)PbI_3 + 2H_20 \rightarrow (MA)_4PbI_6.2H_2O + 3Pb + 2Al^{3+} + 6I^-$$
$$2Al + 3(MA)_4PbI_6.2H_2O \rightarrow 12MAI + 3Pb + 2Al^{3+} + 6I^-$$
$$MAI \leftrightharpoons MA + HI$$

Figure 4.9: Perovskite decomposition mechanism in presence of moisture[24]

The moisture degradation of perovskites is related to the $MAPbI_3$ transforming to the MAI salt and metal halides. The removal of the metal halides by reaction with the electrical contacts of the device hasten the perovskite degradation process. Walsh et al showed that $MAPbI_3$ undergoes

degradation by the introduction of water molecules into the crystal structure, where they form weak hydrogen bonds with the highly hygroscopic methylammonium cations leading to bond dislocations in the crystal structure.

4.4.3 IV Hysteresis

The device performance of a perovskite solar cell depends on the direction in which the voltage is swept across it [25]. Fig. 4.10 shows a typical IV hysteresis curve for a solution processed $MAPbI_3$ n-i-p device.

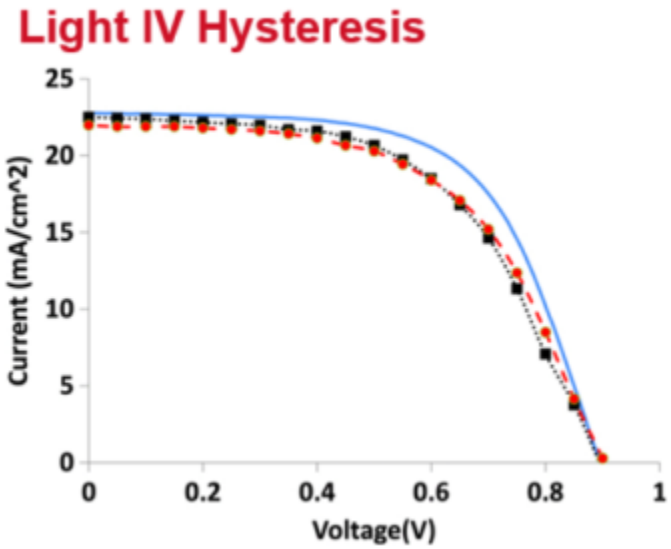

Figure 4.10: Typical IV hysteresis of a n-i-p $MAPbI_3$ device. blue curve represents the scan from high-low bias, red curve represtns the reverese scan from low-high bias with a slow voltage scan and the black curve represents the scan from high to low bias [25]

McGhgee et al. showed that the light IV hysteresis depends upon several factors, such as scan speed, scan direction, and voltage pre-biasing conditions [26]. Zhao et al. showed the origin of these hysteresis behaviors by analyzing the morphological changes that the perovskite material undergoes under an electric field [Fig 4.11].

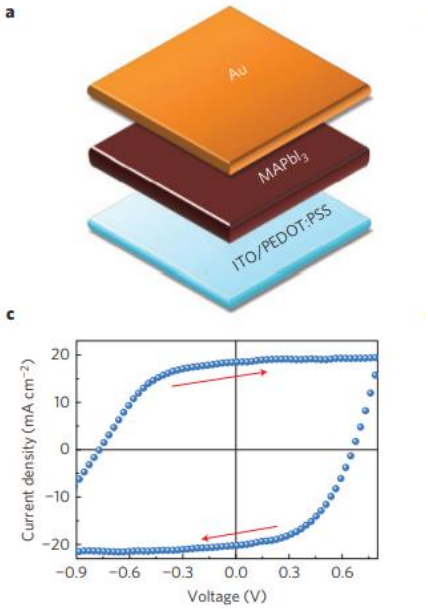

Figure 4.11: (a) Device structure and (b)photo-current hysteresis of the device

Hysteresis behavior can be quantified by the hysteresis index,

$$Hysteresis\ index = \frac{PCE_{FWD} - PCE_{REV}}{PCE_{FWD}} * 100$$

where the PCE_{FWD} and PCE_{REV} are the photoconversion efficiencies of the solar cell measured during a High-Low Voltage bias and Low-High voltage bias respectively.

4.4.4 Environmental Concerns

Most common perovskite materials contain lead, which is an environmentally hazardous material. Further exacerbating the issue is the water solubility of the perovskite material, which becomes a significant problem in deploying perovskite solar cells on roof mounted installations.

4.5 Inorganic Perovskites

The thermal stability of perovskites is a critical problem that needs to be resolved in order to deploy perovskite solar cells in real-world conditions. A strategy to improve the thermal stability of hybrid organic-inorganic perovskites is to replace the organic cation (MA/FA/EA)

with an inorganic cation like Cesium (Cs) or Rubidium (Rb). The thermal instability of the organic-inorganic hybrid perovskites stems from the degradation of the hydrogen bonding between the monovalent organic cation and the octahedral PbI_2. Substituting the organic cation with an inorganic cation improves this bonding behavior between the cation and the PbI_2 octahedra, thus improving stability under thermal stresses.

4.5.1 $CsPbI_3$

The most common such fully inorganic metal halide perovskite is $CsPbI_3$, first studied by Snaith et al. $CsPbI_3$ has a higher band gap of 1.7eV compared to its hybrid organic-inorganic perovskite equivalent (1.6eV). $CsPbI_3$ is present in two forms: the δ- non-perovskite phase as well as the photovoltaically desirable α-perovskite phase [27]. In the α-perovskite phase, the perovskite material is able to absorb light up to a wavelength of 700nm [Fig. 4.12]. The phase transition from δ-phase to α-phase occurs at temperatures of 300+°C. More importantly, $CsPbI_3$ is thermally stable at high temperatures exceeding 300°C.

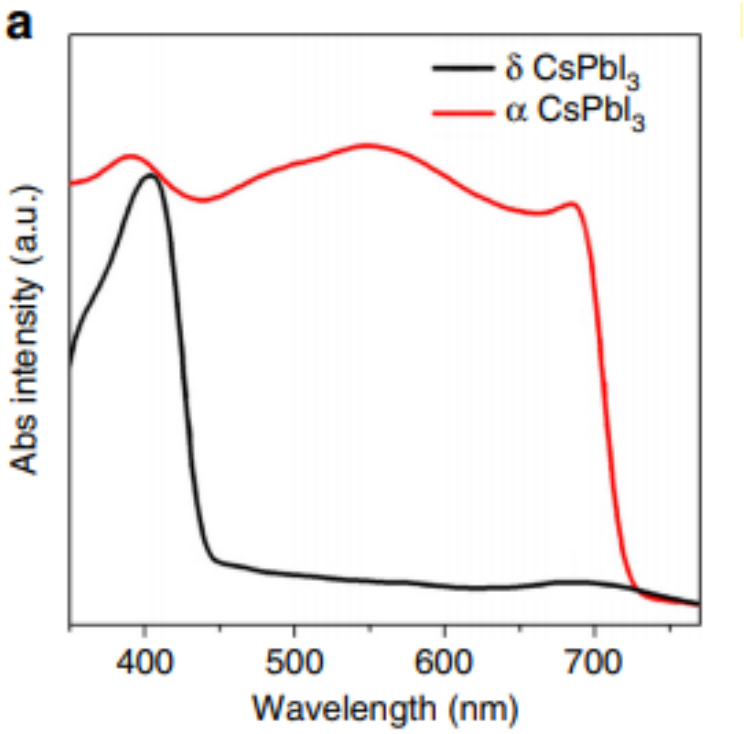

Figure 4.12: Absorption spectra of the alpha phase (red) and delta phase (black) of $CsPbI_3$

4.6 Closing Remarks

This chapter took a brief look at the various advantageous properties of perovskite materials that make it an attractive material for photovoltaics, as well as challenges with perovskite materials that must be overcome to ensure commercial deployment of perovskite solar cells. We also introduced a strategy to overcome the thermal instability of perovskites by switching to fully inorganic perovskite materials like $CsPbI_3$.

The next chapter focuses on the various fabrication techniques used to prepare the perovskite solar cells

References

1. John W. Anthony, Richard A. Bideaux, Kenneth W. Bladh, Monte C. Nichols, *Handbook of Mineralogy*, Mineralogical Society of America.

2. M. A. Peña, J. L. Fierro, "Chemical structures and performance of perovskite oxides", Chemical Reviews. 101 (7): 1981–2017. doi:10.1021/cr980129f. PMID 11710238

3. D. B. Mitzi, S. Wang, C. A. Feild, C. A. Chess, and A. M. Guloy, "Conducting layered organic–inorganic halides containing <110>-oriented perovskite sheets", Science, 267, 1473 (1995). 35

4. D. B.Mitzi, K. Chondroudis, and C. R. Kagan, "Organic-inorganic electronics", IBM J. Res. Dev., 45, 29 (2001). 36

5. H. Topsöe, "Krystallographisch-chemische untersuchungen homologer verbindungen", Zeitschrif für Kristallographie, 8, 246 (1884)

6. A. Kojima, K. Teshima, T. Miyasaka, and Y. Shirai, "Novel photoelectrochemical cell with mesoscopic electrodes sensitized by lead-halide compounds (2)", in Proc. 210th ECS Meeting (ECS, 2006)

7. J. H. Im, C. R. Lee, J. W. Lee, S. W. Park, and N. G. Park, "6.5% efficient perovskite quantum-dot-sensitized solar cell", Nanoscale, 3, 4088 (2011). doi:10.1039/c1nr10867k

8. H. S. Kim, C. R. Lee, J. H. Im, K. B. Lee, T. Moehl, A. Marchioro, S. J. Moon, R.Humphry-Baker, J. H. Yum, J. E. Moser, M. Gratzel, and N. G. Park, "Lead iodide perovskite sensitized all-solid-state submicron thin film mesoscopic solar cell with efficiency exceeding 9%", Sci. Rep., 2, 591 (2012). doi:10.1038/srep00591

9. J. Burschka, N. Pellet, S. J. Moon, R. Humphry-Baker, P. Gao, M. K. Nazeeruddin, and M. Gratzel, "Sequential deposition as a route to high-performance perovskite-sensitized solar cells", Nature, 499, 316 (2013). doi:10.1038/nature12340

10. M. Saliba, T. Matsui, J.-Y. Seo, K. Domanski, J.-P. Correa-Baena, M. K. Nazeeruddin, S. M. Zakeeruddin, W. Tress, A. Abate, A. Hagfeldt, and M. Gratzel, "Cesium-containing triple cation perovskite solar cells: Improved stability, reproducibility and high efficiency", Energy Environ. Sci., 9, 1989 (2016). doi:10.1039/C5EE03874J

11. Hoke, E.T., et al., Reversible photo-induced trap formation in mixed-halide hybrid perovskites for photovoltaics. Chemical Science, 2015. 6(1): p. 613-617
12. Zhao, Y., A.M. Nardes, and K. Zhu, Solid-State Mesostructured Perovskite CH3NH3PbI3 Solar Cells: Charge Transport, Recombination, and Diffusion Length. Journal of Physical Chemistry Letters, 2014. 5(3): p. 490-494

13. Stranks, S.D., et al., Electron-Hole Diffusion Lengths Exceeding 1 Micrometer in an Organometal Trihalide Perovskite Absorber. Science, 2013. 342(6156): p. 341-344

14. La-o-vorakiat et al., Elucidating the role of disorder and free-carrier recombination kinetics in CH3NH3PbI3 perovskite films. Nat Commun, 2015. 6

15. Hooman Mehdizadeh-Rad, Jai Singh, "Influence of Interfacial Traps on the Operating Temperature of Perovskite Solar Cells", Materials, 10.3390/ma12172727, 12, 17, (2727), (2019)

16. Mehran Samiee, Siva Konduri, Balaji Ganapathy, Ranjith Kottokkaran, Hisham A. Abbas, Andrew Kitahara, Pranav Joshi, Liang Zhang, Max Noack, Vikram Dalal, "Defect density and dielectric constant in perovskite solar cells", Appl. Phys. Lett. 105, 153502 (2014); https://doi.org/10.1063/1.4897329

17. Simone Meloni and Giulia Palermo and Negar Ashari Astani and Basile F. E. Curchod and Michael Graetzel and Ursula Roethlisberger, "Valence and conduction bands engineering in halide perovskites for solar cell applications", arxiv.org, 2014,1412.3659

18. Tan, Hairen, Ankit Jain, Oleksandr Voznyy, Xinzheng Lan, F Pelayo García de Arquer, James Z Fan, Rafael Quintero-Bermudez, et al. 2017. "Efficient and Stable Solution-Processed Planar Perovskite Solar Cells via Contact Passivation." Science (New York, N.Y.) 355 (6326): 722–26. https://doi.org/10.1126/science.aai9081.

19. Ranjith Kottokkaran, Hisham A. Abbas, Ganapathy Balaji, Liang N Zhang, Mehran Samiee, Andrew Kitahara, Max A. Noack, Vikram L. Dalal, "Highly reproducible vapor deposition technique, device physics and structural instability of perovskite solar cells", IEEE 42nd Photovoltaic Specialist Conference (PVSC), 2015

20. Weidong Xu,Lijia Liu, Linju Yang, Pengfei Shen, Baoquan Sun, John A. McLeod, "Dissociation of Methylammonium Cations in Hybrid Organic−Inorganic Perovskite Solar Cells", Nano Lett. 2016;16:4720–4725. doi:0.1021/acs.nanolett.6b02307

21. Global Solar Atlas, www.globalsolaratlas.info

22. Miguel García, Luis Marroyo, Eduardo Lorenzo, Javier Marcos, Miguel Pérez, "Solar irradiation and PV module temperature dispersion at a large-scale PV plant", Progress in Photovoltaics, Vol 23, Issue 10, 2014

23. R. Dubey, S. Chattopadhyay, J. J John, V. Kuthanazhi, A. Kottantharayil, B. M. Arora, . . . J. Vasi. (2018). Day Light Electroluminescence Imaging of Photovoltaic Modules by Image Difference Technique. *IEEE 7th World Conference on Photovoltaic Energy Conversion* , 0690-0694.

24. Lianfeng Zhao, Ross A. Kerner, Zhengguo Xiao, YunHui L. Lin, Kyung Min Lee, Jeffrey Schwartz, and Barry P. Rand, "Redox Chemistry Dominates the Degradation and

Decomposition of Metal Halide Perovskite Optoelectronic Devices", ACS Energy Lett. 2016, 1, 595−602, DOI: 10.1021/acsenergylett.6b00320

25. Henry J. Snaith, Antonio Abate, James M. Ball, Giles E. Eperon, Tomas Leijtens, Nakita K. Noel, Samuel D. Stranks, Jacob Tse-Wei Wang, Konrad Wojciechowski, and Wei Zhang, "Anomalous Hysteresis in Perovskite Solar Cells", J. Phys. Chem. Lett., 2014, 5 (9), pp 1511–1515, DOI: 10.1021/jz500113x

26. Zhengguo Xiao, Yongbo Yuan, Yuchuan Shao, Qi Wang, Qingfeng Dong, Cheng Bi, Pankaj Sharma, Alexei Gruverman & Jinsong Huang, "Giant switchable photovoltaic effect in organometal trihalide perovskite devices", Nature Materials volume 14, pages 193–198 (2015), doi:10.1038/nmat4150

27. Eperon, Giles & Paterno, Giuseppe & Hawke, Rebecca & Zampetti, Andrea & Haghighirad, Amir-Abbas & Cacialli, Franco & Snaith, Henry. (2015). Inorganic caesium lead iodide perovskite solar cells. J. Mater. Chem. A. 3. 10.1039/C5TA06398A.

28. Wang, Qi, Xiaopeng Zheng, Yehao Deng, Jingjing Zhao, Zhaolai Chen, and Jinsong Huang. "Stabilizing the α-Phase of CsPbI3 Perovskite by Sulfobetaine Zwitterions in One-Step Spin-Coating Films." *Joule* 1, no. 2 (October 2017): 371–82. https://doi.org/10.1016/j.joule.2017.07.017

CHAPTER 5. FABRICATION OF PEROVSKITE SOLAR CELLS

5.1 Introduction

One of the biggest advantages of perovskite solar cells is their ease of fabrication. Perovskite solar cells can be fabricated in two basic architectures: n-i-p and p-i-n, as discussed in Chapter 2 [Fig.5.1]. A wide variety of materials can be used as the n+ and p+ layers. A selection of the available electron transport layers (ETL) and hole transport layers (HTL) are shown in Fig.5.2 with the position of their conduction and valence bands. Some of the common electron transport layers (ETL) used in fabricating perovskite solar cells are organic compounds, such as Phenyl C61 butyric acid methyl ester (PCBM), and inorganic compounds, such as Cadmium Sulfide (CdS), Zinc Oxide (ZnO), and Titanium-di-oxide (TiO_2). Common hole transport layers include organic compounds like Poly[bis(4-phenyl) (2,4,6-trimethylphenyl) amine] (PTAA), Poly(3-hexylthiophene-2,5-diyl) (P3HT), Poly(4-butylphenyldiphenylamine) (Poly-TPD), poly(3,4-ethylenedioxythiophene) polystyrene sulfonate (PEDOT:PSS), and inorganic metal oxides like Nickel Oxide (NiO_x) and Molybdenum Oxide (MoO_x). Often, these transport layers are doped to increase their conductivity; for example, CdS is doped with Indium and ZnO is doped with Al. Organic transport layers like PTAA and P3HT can be doped with 2,3,5,6-Tetrafluoro-7,7,8,8-tetracyanoquinodimethane (F4-TCNQ) as well.

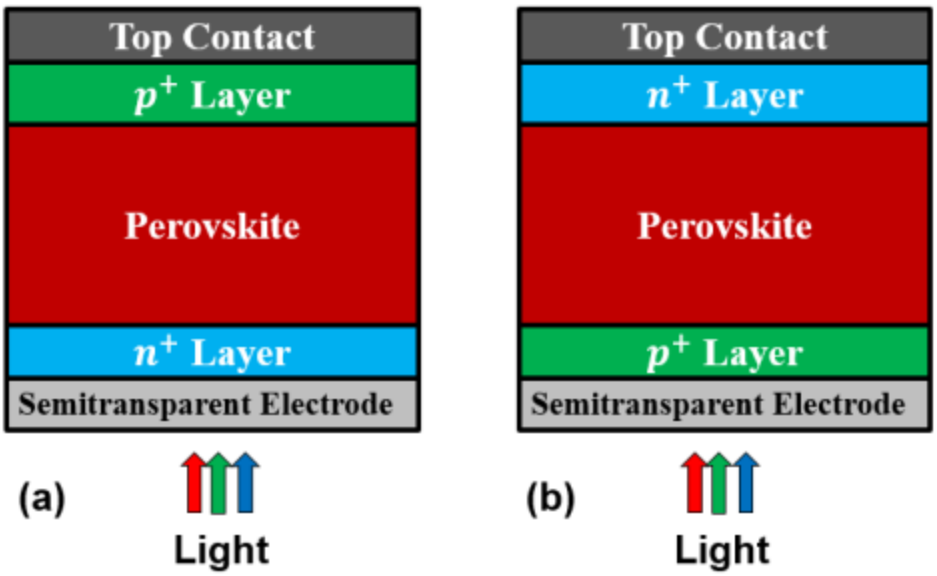

Figure 5.1: Device structure of a n-i-p(a) and p-i-n (b) solar cell

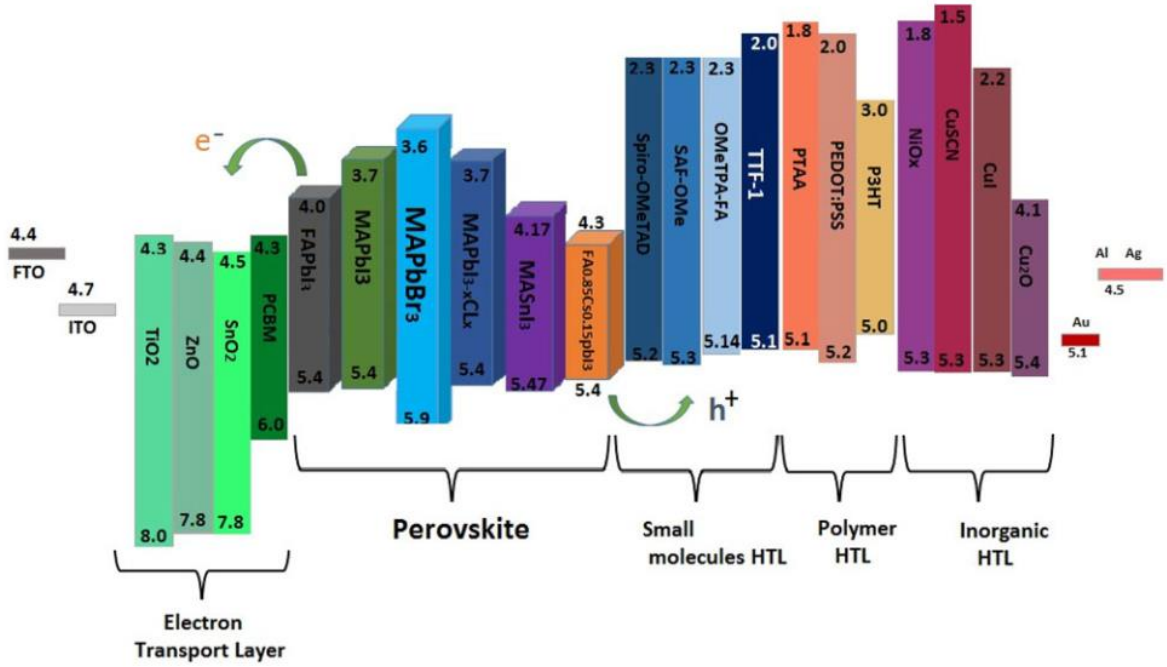

Figure 5.2: Variety of ETL and HTL possibilities for perovskite solar cells

5.2 Perovskite Fabrication Techniques

Several different deposition techniques can be used to grow perovskite materials as illustrated in Fig.5.3.

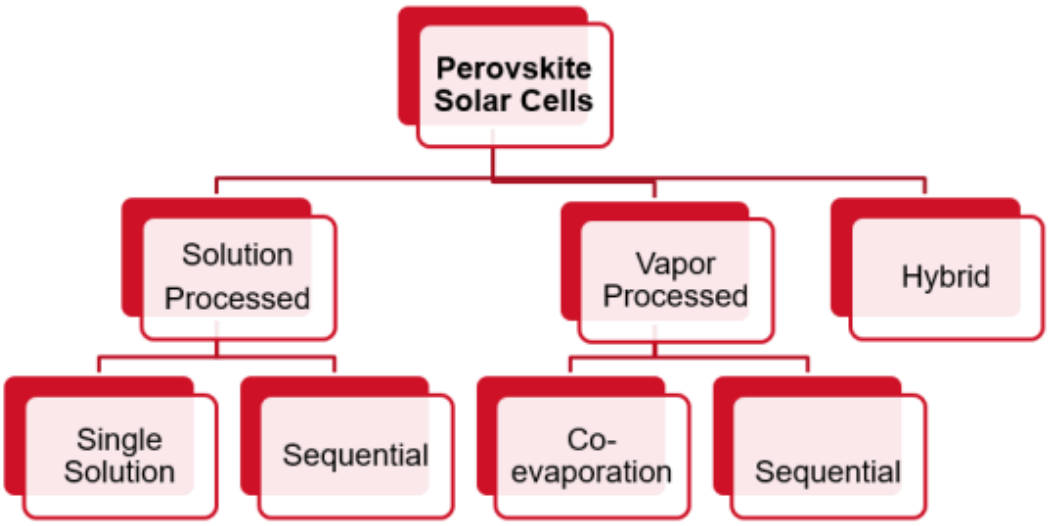

Figure 5.3: Different fabrication techniques for perovskite solar cells

5.2.1 Solution processed growth

In solution process the perovskites are grown using precursor chemicals (MAI, CsI, PbI_2, $PbBr_2$), which are dissolved in organic solvent like Dimethylformamide (DMF), Toluene, and Acetone. The precursor chemical solutions are then spin-coated onto a substrate to form the perovskite material. A subsequent annealing step is necessary to remove the organic solvents from the perovskite films. Solution processing can be done with all the precursors in a single solution or by sequential solution processing of each precursor separately[1-5].

Due to its ease of processing and the relatively cheap equipment needed for processing, solution process is by far the most common method to grow perovskite solar cells in research labs. However, even optimized solution growth techniques suffer from problems with

reproducibility. The crystallization process in the solution growth technique is affected by many factors including the solvents, precursor chemical used, surface properties of the substrate before solution process, the solvent evaporation rates during growth, and annealing[6,7]. Due to the wide variability of these factors even in well controlled environments, the perovskite films grown by this technique have variations in film morphology, thickness, crystallinity, and crystal size, which play a major role in the photovoltaic performance of the devices. Further, incomplete evaporation of the solvents used during the growth can act as parasitic shunt pathways in the solar cell.

5.2.2 Vapor processed growth

In vapor processed growth, the precursor chemicals are evaporated directly on to the substrate in a low-pressure environment [6-12]. Vapor processing is a mature technique widely used in the semiconductor industry to grow thin-film transistors, liquid crystal displays (LCDs), light emitting diodes (LEDs), as well as in other industrial processes, Vapor deposition inherently possesses several advantages over solution processing, such as:

1. Vapor processing is inherently scalable and ready for large scale adoption, making it suitable for commercial availability. For example, large area vapor deposition processing is commonly used in the manufacture of thin metal coating and in the fabrication of Cadmium Telluride solar cells.
2. High purity precursor films can be deposited on to substrates without the need to introduce unnecessary intermediate materials into the films.
3. Precise stoichiometry can be achieved irrespective of the precursor chemical used. For example, solubility limits of Br and Cl salts in the commonly used DMF solvent complicates the growth of Br and Cl based perovskites using single solution processing.

4. Commonly used solvents like DMF, DMSO, water, and chlorobenzene have boiling points in excess of 100°C. This restricts the temperature at which solution grown perovskite layers can be annealed due to the thermal instability of most hybrid organic-inorganic perovskites at temperatures over 100°C. To prevent thermal degradation, the perovskites are annealed at sub boiling point temperatures, preventing the complete removal of solvents from the perovskite film. These solvents intercalated between perovskite grains and crystal act as parasitic shunt pathways, degrading device performance.
5. Vapor deposition enables multiple stacks of films to be grown on top of each other. This technique can be leveraged to grow tandem cells. Solution processing multiple stacks of different materials is tricky, as the solvents would wash away underlying structures.
6. Vapor deposition enables deposition on a wider variety of substrates. Surface morphology of the substrates do not play a big role in vapor deposition. Wettability of substrates is critical for complete and uniform coverage during spin-coating. For example, solution processing with DMF solvents is not possible on polymer transport layers like Poly-TPD, P3HT and PTAA.
7. Careful control of the deposition rate and deposition times ensures good thickness control. Precise thickness control is essential for optimum charge collection efficiencies, which is easily achieved through vapor deposition. Solution processed growth, on the other hand, relies on optimizing the spin speed and concentration of the solution, which is often inexact and difficult.

8. Vapor deposition facilitates better device reproducibility. The crystallization process in vapor deposited perovskites depends on easily controllable and reproducible parameters, such as the deposition rate of the precursors, the temperatures of the substrate during deposition, and the subsequent anneal temperatures.

Vapor deposition of perovskites can be achieved through co-evaporation where the precursor chemicals are evaporated simultaneously onto the substrate, or sequential vapor deposition where the precursor chemicals are evaporated sequentially [Fig. 5.2.1].

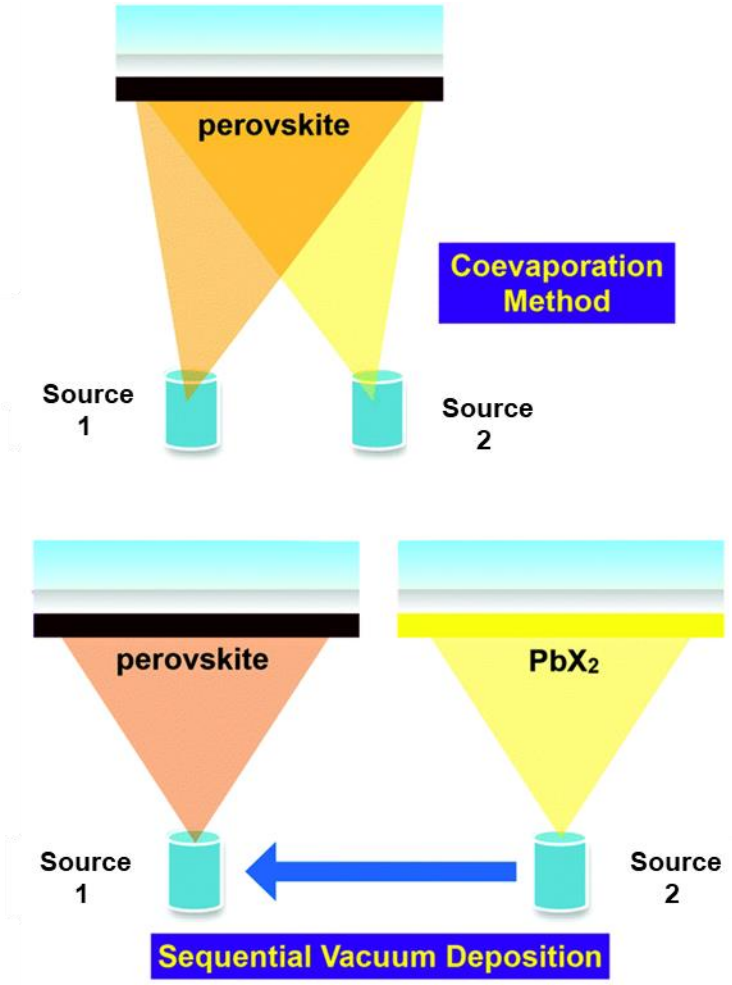

Figure 5.4: Co-evaporation (top) and sequential vapor deposition (bottom) techniques

This report solely focuses on sequentially vapor deposited perovskites due to their inherent advantages over solution processed perovskites in both reproducibility and the ability to precisely control the stoichiometry of the resultant perovskite materials.

5.3 Perovskite Deposition System

Our custom-built deposition system consists of three Luxel furnaces mounted in a stainless deposition chamber pumped down to deposition pressures in the 10^{-7} Torr range. The interior of the deposition chamber is showed in Fig 5.5. The deposition chamber is pumped down using a two stage vacuum pump system consisting of a mechanical roughing pump to bring the pressure from atmospheric pressure down to 700mTorr and a turbo mechanical pump connected to the chamber via a gate valve that operated below 700mTorr and further pumped the chamber down to operating pressures. The mechanical pumps were purged with nitrogen to prevent oil back streaming. Pressures were monitored using two Pirani gauges, one each for the roughing and backing pumps, to measure pressures from 0.5 Torr to 1mTorr. A hot-filament ionization gauge was used to measure chamber pressures once the pressure dropped below 1mTorr. The Luxel furnaces were powered using high power DC power supplies and connected to individual thermocouples to accurately monitor the temperature. The DC power supplies were chosen to ensure that exact control of the current flowing to the Luxel furnace was possible to ensure precise temperature control. A removable substrate holder capable of holding substrates of 2inch X 1inch was fitted with a substrate heater and thermocouple. A variac transformer was used to control the temperature of the substrate. A quartz crystal monitor (QCM) was used to measure the deposition rate of the precursor

materials. A substrate shutter was installed to control the deposition onto the substrate. The deposition chamber, power supplies and pumping mechanism is shown in Fig 5.6.

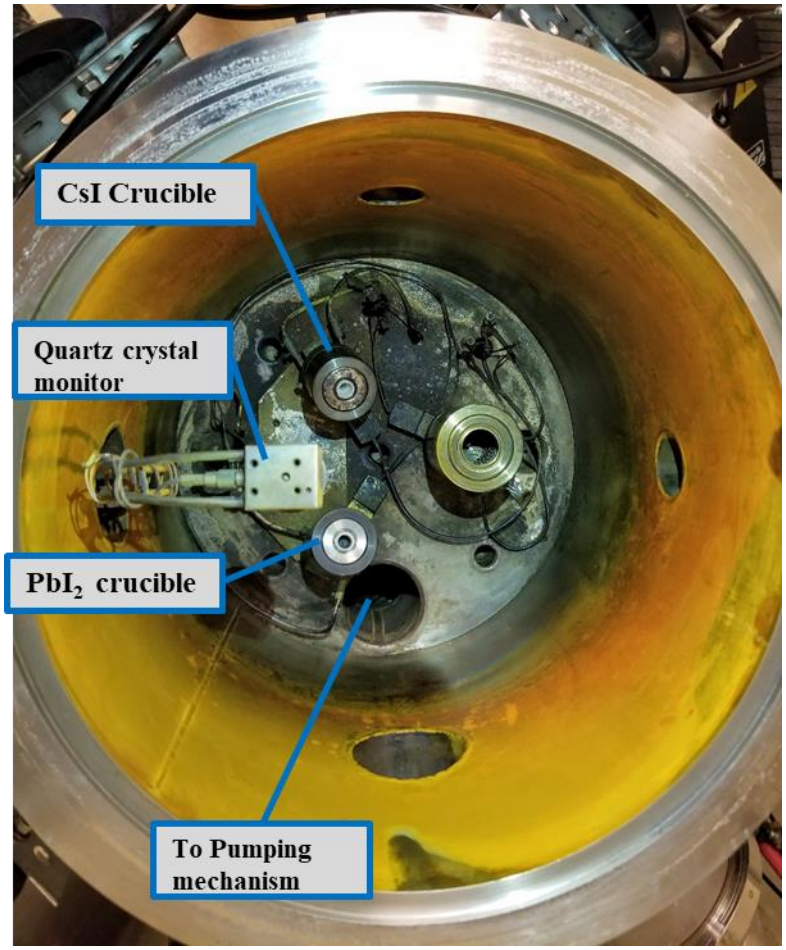

Figure 5.5: Inside of the deposition chamber showing the luxel furnaces and Quartz Crystal Monitor

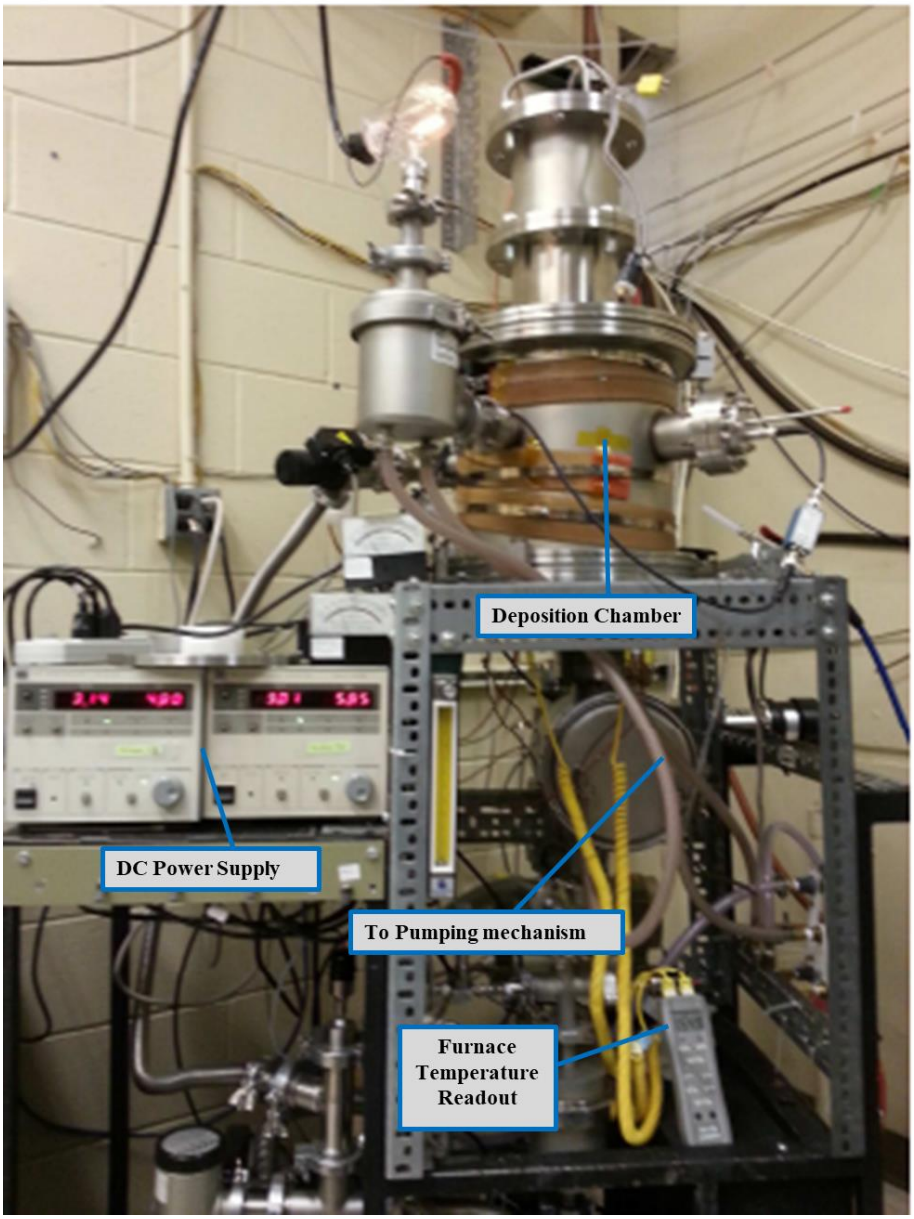

Figure 5.6: The deposition system showing the deposition chamber, DC power supply and furnace temperature monitor

5.3.1 Perovskite growth process

Prior to the growth of the perovskite layer, the Luxel furnaces were charged with the two precursor chemicals and the QCM was calibrated using a surface profilometer for each individual precursor material. Substrates were loaded into the deposition chamber using a

substrate mask. The deposition chamber was pumped down to operating pressures in the low 10^{-7} Torr range to ensure high purity of the material grown. The substrate temperature was raised and lowered to ensure complete outgassing of the substrate and remove any moisture that may have condensed onto it. The Luxel furnaces were heated in a gradual manner up to their holding temperature, at which point they were not yet able to evaporate the precursors. Next, one of the Luxel furnaces was heated further up to its operating temperature with the substrate shutter closed to ensure no deposition on to the substrate. Once the Luxel furnace was at the operating temperatures and stabilized for 5 minutes and the QCM showed a stable rate of deposition, the substrate shutter was opened to deposit a thin layer of the first precursor chemical. Once the required thickness of the first precursor layer was reached, the substrate shutter was closed and the temperature of the first Luxel furnace was brought down to its holding temperature. Simultaneously, the temperature of the Luxel furnace with the second precursor was heated up. Upon reaching its operating temperature and achieving a stable rate of deposition, the substrate shutter was opened to deposit the second precursor material onto the substrate. Upon the deposition of the required thickness of the second precursor chemical the substrate shutter was closed and the second Luxel furnace cooled down to its holding temperature. This process was repeated in multiple cycles to obtain the desired thickness of the final film. Fig 5.7 shows a schematic of the entire deposition process.

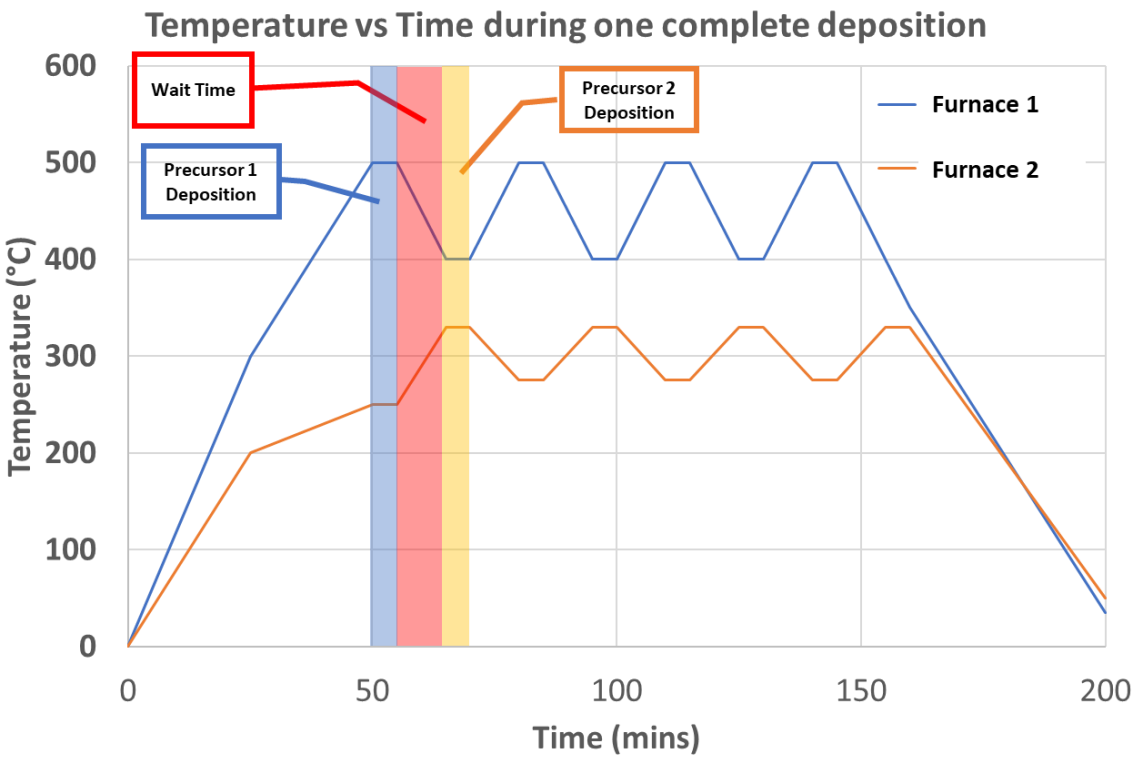

Figure 5.7: Schematic of one complete deposition showing the sequential heating of furnaces, deposition times and wait times

The final film was then unloaded and transferred into a nitrogen glove box using a nitrogen flushed vacuum nipple. The film was annealed on a calibrated hot plate in the nitrogen glove box to complete the formation of the perovskite material.

5.4 Closing Remarks

This chapter described the various fabrication techniques that can be used to fabricate perovskite solar cells. The advantages in using vapor deposition technique and our reasoning behind pursuing this technique have been explained.

In the next chapter we look at the fabrication of the fully inorganic lead halide perovskite, $CsPbI_3$. We focus on the optimization of the device fabrication process to improve device performance.

References

1. J. B. You, Z. R. Hong, Y. Yang, Q. Chen, M. Cai, T. B. Song, C. C. Chen, S. R. Lu, Y. S. Liu, and H. P. Zhou, "Low-temperature solution-processed perovskite solar cells with high
efficiency and flexibility", ACS Nano, 8, 1674 (2014). doi:Doi 10.1021/Nn406020d

2. N. Ahn, D. Y. Son, I. H. Jang, S. M. Kang, M. Choi, and N. G. Park, "Highly reproducible perovskite solar cells with average efficiency of 18.3% and best efficiency of 19.7% fabricated via lewis base adduct of lead(ii) iodide", J. Am. Chem. Soc., 137, 8696 (2015). doi:10.1021/jacs.5b04930

3. Y. Zhou, M. Yang, W. Wu, A. L. Vasiliev, K. Zhu, and N. P. Padture, "Room temperature crystallization of hybrid-perovskite thin films via solvent–solvent extraction for high-performance solar cells", J. Mater. Chem. A, 3, 8178 (2015). doi:10.1039/c5ta00477b

4. M. Xiao, F. Huang, W. Huang, Y. Dkhissi, Y. Zhu, J. Etheridge, A. Gray-Weale, U.Bach, Y.-B. Cheng, and L. Spiccia, "A fast deposition-crystallization procedure for highly efficient lead iodide perovskite thin-film solar cells ", Angew. Chem., 126, 10056 (2014)

5. Z. Xiao, C. Bi, Y. Shao, Q. Dong, Q. Wang, Y. Yuan, C. Wang, Y. Gao, and J. Huang, "Efficient, high yield perovskite photovoltaic devices grown by interdiffusion of solution processed precursor stacking layers", Energy Environ. Sci., 7, 2619 (2014) doi:10.1039/c4ee01138d

6. X. Li, D. Bi, C. Yi, J. D. Decoppet, J. Luo, S. M. Zakeeruddin, A. Hagfeldt, and M. Gratzel, "A vacuum flash-assisted solution process for high-efficiency large-area perovskite solar cells", Science, 353, 58 (2016). doi:10.1126/science.aaf8060

7. D. Zhao, W. Ke, C. R. Grice, A. J. Cimaroli, X. Tan, M. Yang, R. W. Collins, H. Zhang, K. Zhu, and Y. Yan, "Annealing-free efficient vacuum-deposited planar perovskite solar cells with evaporated fullerenes as electron-selective layers", Nano Energy, 19, 88 (2016). doi:10.1016/j.nanoen.2015.11.008

8. M. Liu, M. B. Johnston, and H. J. Snaith, "Efficient planar heterojunction perovskite solar cells by vapour deposition", Nature, 501, 395 (2013). doi:10.1038/nature1250

9. Q. Lin, A. Armin, R. C. R. Nagiri, P. L. Burn, and P. Meredith, "Electro-optics of perovskite solar cells", Nat. Photonics, 9, 106 (2014). doi:10.1038/nphoton.2014.284

10. H. A. Abbas, R. Kottokkaran, B. Ganapathy, M. Samiee, L. Zhang, A. Kitahara, M.Noack, and V. L. Dalal, "High efficiency sequentially vapor grown n-i-p ch3nh3pbi3 perovskite solar cells with undoped p3ht as p-type heterojunction layer", APL Materials, 3,016105 (2015). doi:10.1063/1.4905932

11. Kottokkaran, Ranjith, Harshavardhan A. Gaonkar, Behrang Bagheri, and Vikram L. Dalal. “Efficient P-i-n Inorganic CsPbI3 Perovskite Solar Cell Deposited Using Layer-by-Layer vacuum Deposition.” Journal of Vacuum Science & Technology A 36, no. 4 (July 2018): 041201. https://doi.org/10.1116/1.5029253

CHAPTER 6. CESIUM LEAD IODIDE PEROVSKITE

Cesium lead iodide perovskites were grown using a layer-by-layer sequential vapor deposition technique with PbI_2 and CsI as the precursor materials. Devices were fabricated with a p-i-n architecture with the following structure: ITO/HTL/Perovskite/PCBM/Al. Device optimization was carried out to improve device performance. Devices were fabricated on an ITO coated glass substrate. The ITO coated glass substrate was cleaned using a 5% surfactant solution, deionized water, methanol, acetone, and isopropanol. Multiple different hole transport layers (HTL) were used to optimize device performance. PCBM was chosen as the electron transport layer (ETL) due to its simple fabrication using spin-coating, less hysteresis effects, and its success as an efficient transport layer as used by multiple research groups. PCBM was deposited using spin-coating a 30mg/mL solution in chlorobenzene at 2000RPM for 40 seconds. The top contact of Aluminum was deposited using thermal evaporation using a mask to define the device area. Both the PCBM and Al were processed inside a nitrogen glovebox to prevent moisture degradation of the perovskite material.

6.1 Optimizing the hole transport layer

Choice of the optimal hole transport layer (HTL) is critical for efficient device performance. In general, HTL in a p-i-n device architecture must be chosen so that it possesses a high enough band gap that it does not absorb much light. Ideally, the valence band of the HTL layer must match well with the valence band of the perovskite to easily collect electrons, but the conduction band should be higher than that of perovskite to form an effective barrier for the holes. We worked with a variety of HTLs including organic semiconductors like PEDOT:PSS, Poly-TPD, PTAA, and inorganic compounds such as HTLs like p-type amorphous Si:C, and metal oxides like MoOx and NiOx.

6.1.1 PEDOT:PSS

Poly(3,4-ethylenedioxythiophene)-polystyrenesulfonate (PEDOT:PSS) is a conductive polymer blend in water with the chemical structure as described in Fig. 6.1(a). The energy band diagram of the device architecture is shown in Fig. 6.1(b), which shows that the valence bands of the perovskite material and PEDOT:PSS are reasonably matched with only a 0.2eV offset, ensuring efficient collection of holes. The conduction band of PEDOT:PSS is sufficiently offset from the perovskite, ensuring that electrons are rejected.

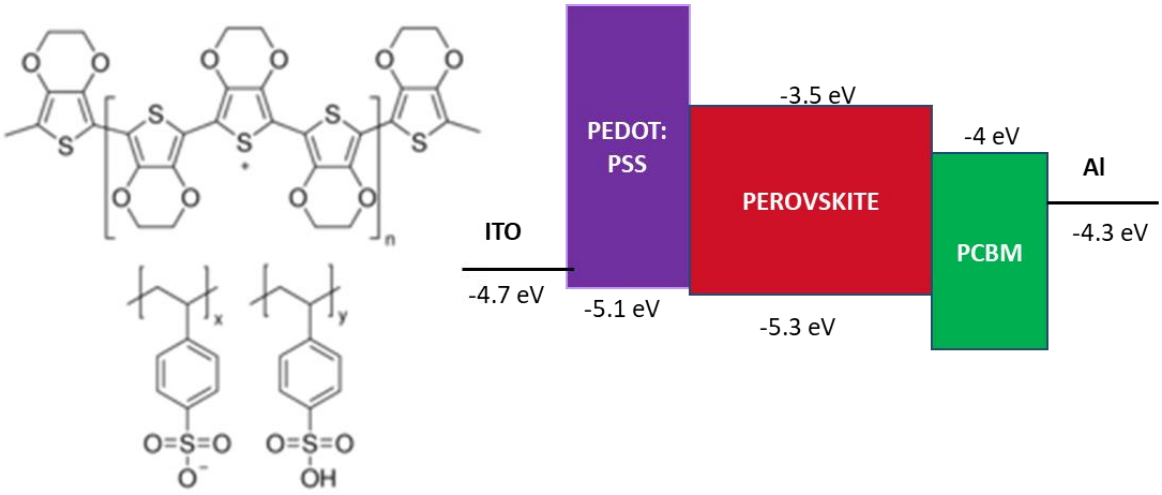

Figure 6.1: (a) The chemical structure of PEDOT:PSS and (b) the device energy band diagram

PEDOT:PSS suspensions of 1.5% in water were spin- coated on to a cleaned ITO glass substrate that was functionalized by an air plasma treatment for 10 minutes. The suspensions were spun at 4000RPM for 40seconds and annealed at 150°C/20 minutes in air. Fig. 6.2 shows the JV curve of the resultant device.

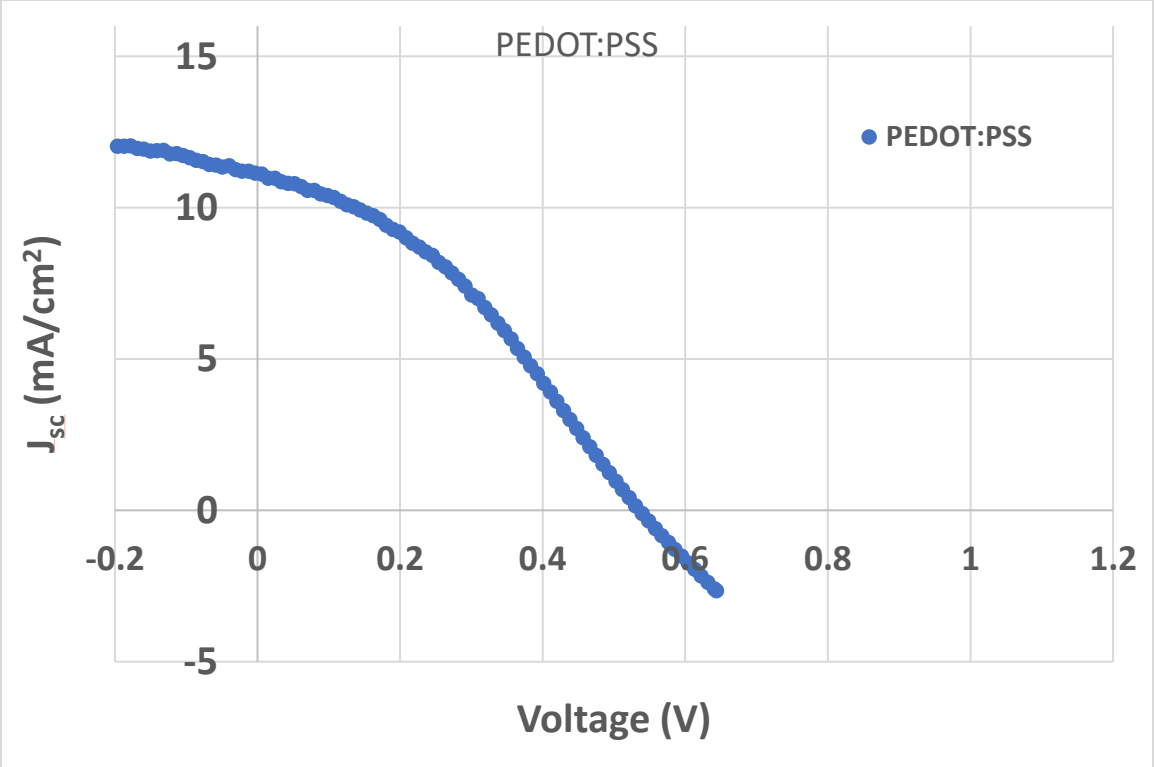

HTL	V_{OC} (V)	ISC (mA/cm^2)	FF (%)	PCE (%)
PEDOT:PSS	**0.54**	**10.9**	**31**	**2.2**

Figure 6.2: JV Curve and characteristics of PEDOT:PSS device

6.1.2 Poly-TPD

Poly [N,N'-bis(4-butylphenyl)-N,N'-bisphenylbenzidine] (Poly-TPD)[Fig 6.3(a)] is another organic semiconductor commonly used as the HTL in photovoltaics and LEDs. Like PEDOT:PSS, Poly-TPD also has a favorable energy band gap match with $CsPbI_3$ [Fig 6.3(b)]. Multiple different concentrations of Poly-TPD were used to optimize device performance. The

solutions were spun at 6000ROMS for 40 seconds and annealed at 150°C for 10 minutes to remove the solvents.

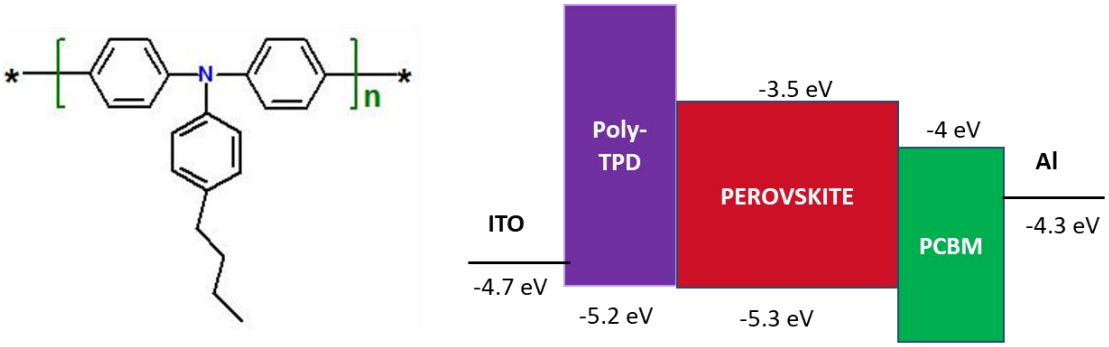

Figure 6.3: (a) The chemical structure of P3HT and (b) the device energy band diagram

Fig 6.5 shows the JV characteristics for the various concentration used. We see that the best device performance is seen for a concentration of 3.25mg/mL with both the JSC and V_{OC} peaking. However, the low fill factors of less than 50% and the high series resistance suggest the presence of a non-ohmic contact in the device.

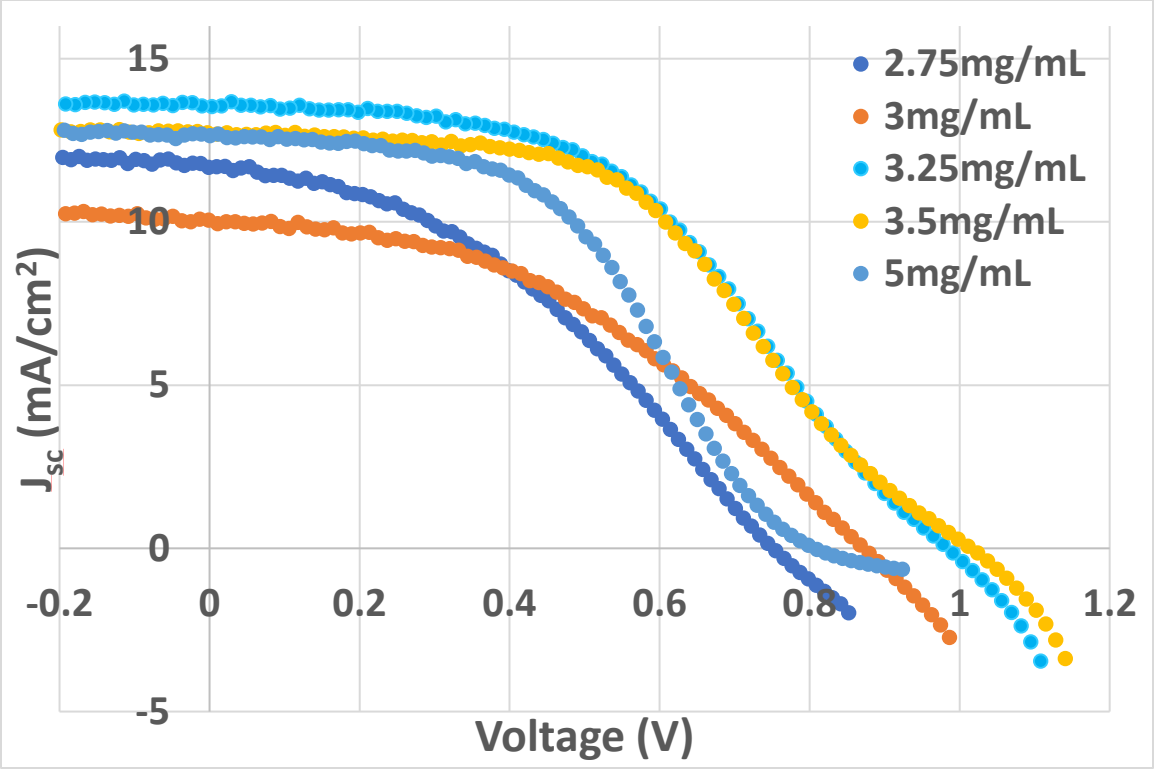

Conc. Of Poly-TPD	V_{OC} (V)	ISC (mA)	FF (%)	PCE (%)
2.75mg/mL	0.76	11.7	39	3.5
3mg/mL	0.87	10	42	3.7
3.25mg/mL	0.99	13.5	48	6.4
3.5mg/mL	1.01	12.6	48	6.2
5mg/mL	0.81	12.6	48	4.86

Figure 6.4:JV Curve and characteristics of devices fabricated with various P3HT concentrations

6.1.3 p-a (Si:C)

p-type amorphous silicon carbide (p-a-Si:C) has an excellent band gap match with perovskite [Fig 6.5]. p-a-Si:C was grown using a Plasma enhanced Chemical Vapor Deposition (PECVD) system using a mixture of silane, methane, hydrogen, and dopant gas. Due to the small band gap of the p-a-SiC, a large fraction of the usable light can be absorbed by the HTL itself. Fig 6.6 shows the JV characteristics of the devices with p-a-SiC grown at 250°C as the HTL. We see that as the thickness of the HTL reduces the current density goes up, indicating that the HTL itself is absorbing light. p-a-SiC grown at higher temperatures have larger band- gaps, thereby reducing the absorption in the HTL itself. However, the higher temperature plasma also reacts with the ITO substrate, leading to poor devices.

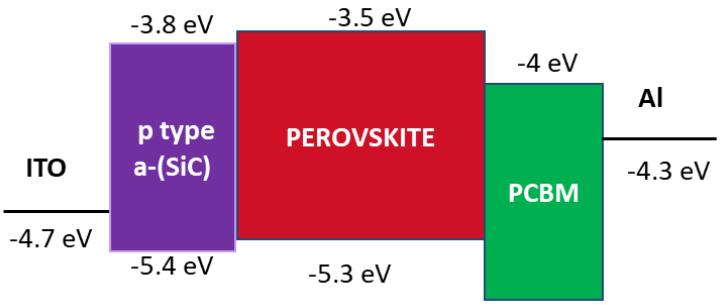

Figure 6.5: Energy band diagram of devices with p-a-Si:C as HTL

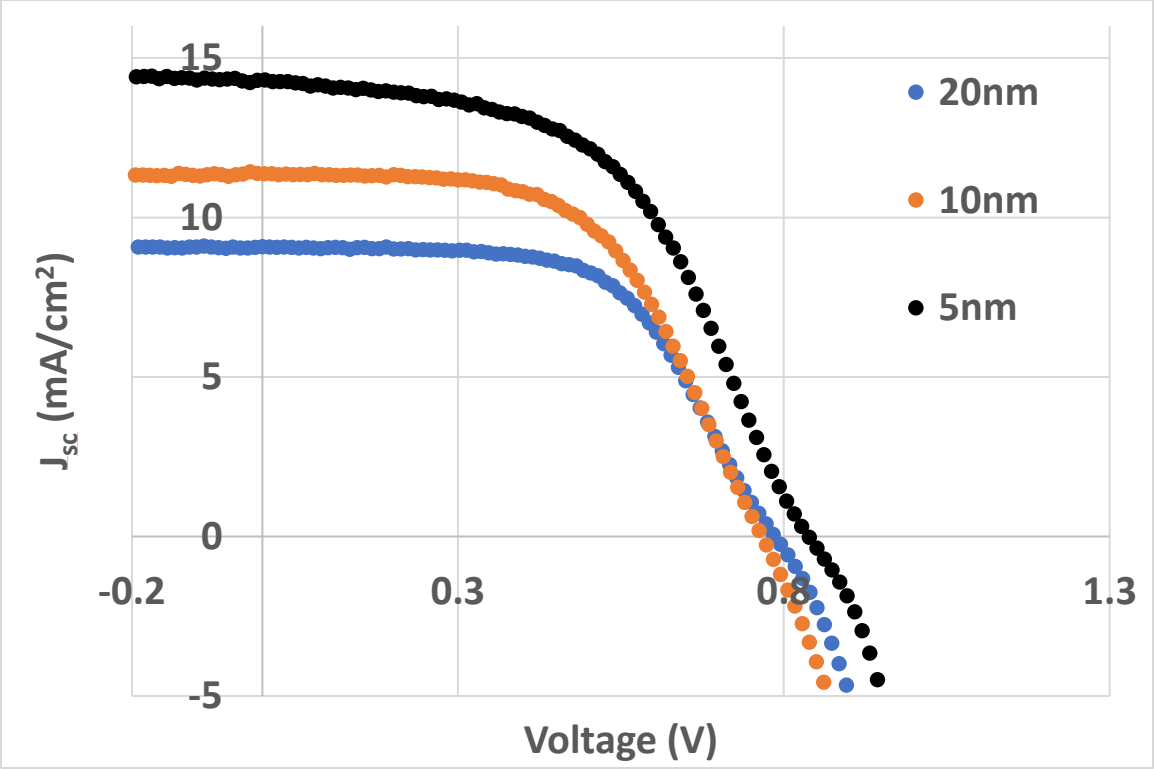

a-SiC thickness	V_{OC} (V)	ISC (mA/cm^2)	FF (%)	PCE (%)
20nm	0.79	9.0	60	4.25
10nm	0.76	9.9	57	4.90
5nm	0.84	14.25	53	6.20

Figure 6.6: JV Curve and characteristics of devices with various thickness of p-a-Si:C as HTL

6.1.4 PTAA

Poly(triaryl amine), Poly[bis(4-phenyl)(2,4,6-trimethylphenyl)amine] (PTAA) is an organic p-type semiconductor with high carrier mobilities that is often used as a hole transport layer in perovskite solar cells. Fig 6.7(a) shows the chemical structure of PTAA and Fig 6.7(b) shows the energy band diagram of the solar cell. PTAA is a direct gap semiconductor with a band gap of ~3eV, which ensures high transmission in both the UV and visible regimes. Solutions of PTAA in toluene were prepared and spin coated onto ITO substrates at 6000RPM for 60 seconds. The JV characteristics are displayed in Fig. 6.8, showing the best device performance for a concentration of 1.1mg/mL. Both higher and lower concentrations of PTAA result in higher resistance in the device, leading to poor device performance. The optimum concentration of 1.1mg/mL corresponds to a very thin ~20nm layer of PTAA.

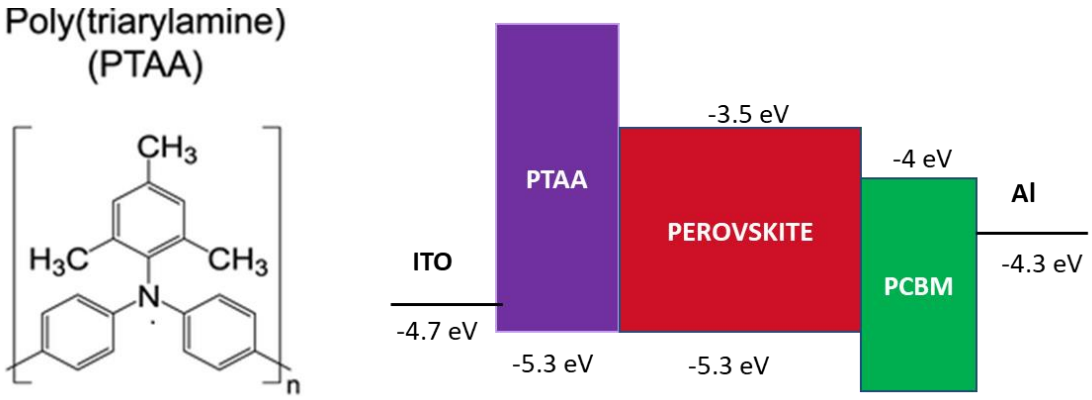

Figure 6.7: (a)Chemical structure of PTAA and (b)device energy band diagram

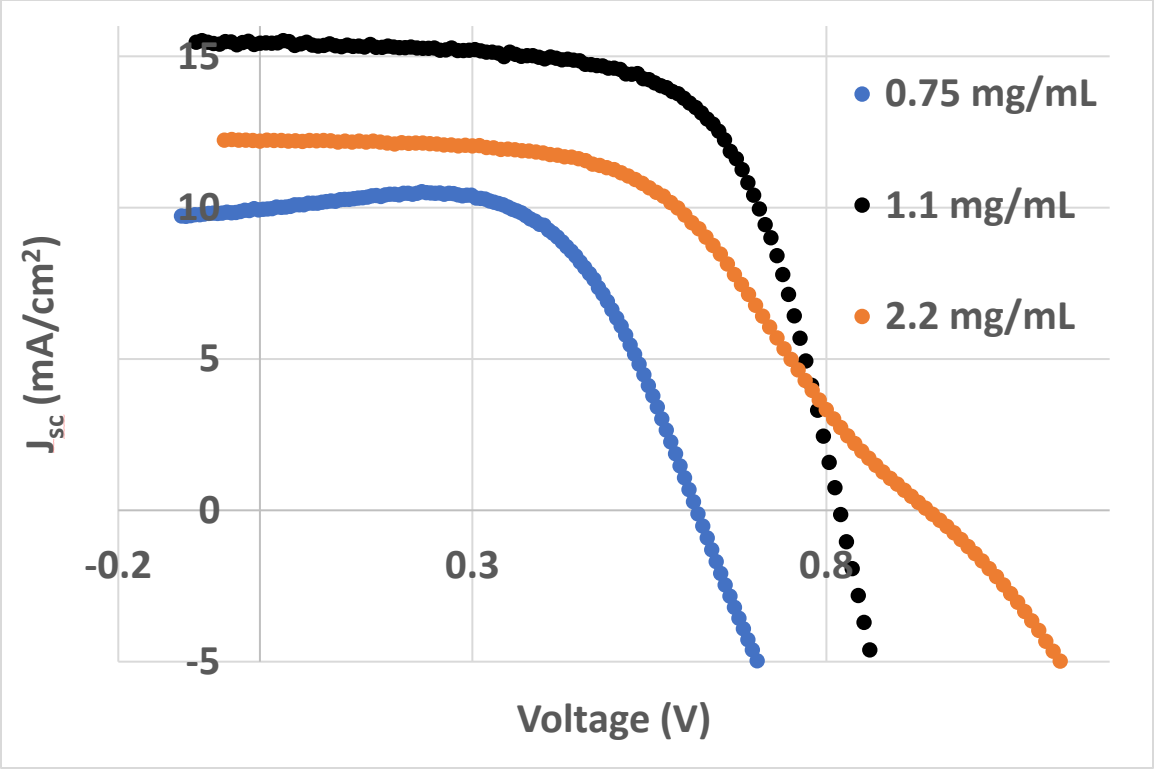

PTAA conc.	V_{OC} (V)	ISC (mA/cm^2)
0.75 mg/mL	0.62	10
1.1 mg/mL	0.82	15.4
2.2 mg/mL	0.95	12.2

Figure 6.8: JV Curve and characteristics of devices fabricated with various PTAA concentrations

Fig 6.9 displays the best JV curves of the various HTLs used in optimizing device performance. PTAA is by far the best, with a high current density of 15.5mA/cm2 and V_{OC} of 0.82V with high fill factors and low series resistances.

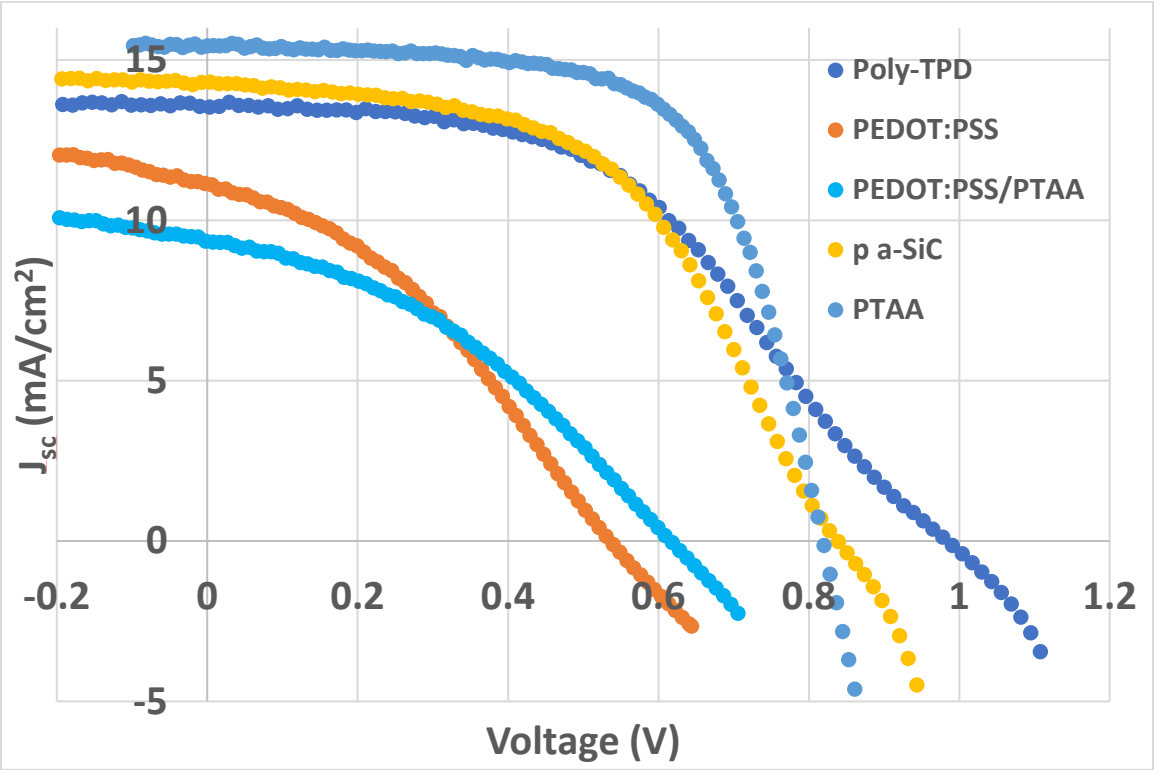

Figure 6.9: JV Curves of the best devices fabricated with various HTL

6.2 Optimizing the Anneal Conditions

The anneal conditions play a key role in the crystallization of the perovskite material from the precursors. It has been shown that $CsPbI_3$ crystallizes into its active α-phase from the δ-phase at temperatures above 310°C. Upon experimenting with various anneal conditions, we adopted the two-step anneal process to form our perovskite material.

The first step involved a low temperature anneal at 150°C for 5 minutes to ensure that any moisture condensed on our film was removed. The second, high temperature step ensured the formation of the perovskite into its preferable α-phase. Anneal temperatures for the second,

high temperature anneal was varied from 315°C to 330°C. We observed that at lower temperatures of 315°C and below the perovskite formed incompletely, with some areas of the film still showing a yellow non-perovskite phase [Fig 6.10]. At temperatures above 320°C, the perovskite film had a gray luster. The JV characteristics of the perovskite films annealed at these multiple temperatures are shown in 6.11.

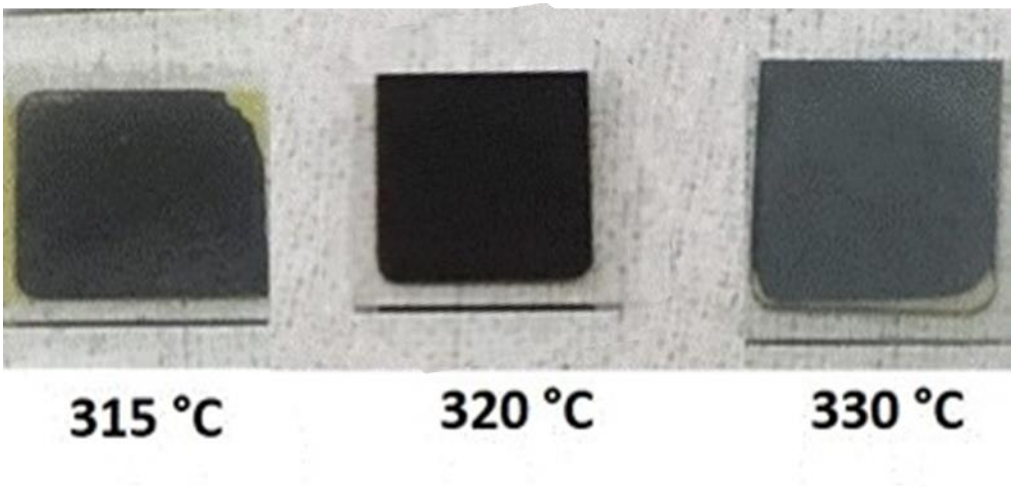

Figure 6.10: Perovskite films annealed at different temperatures

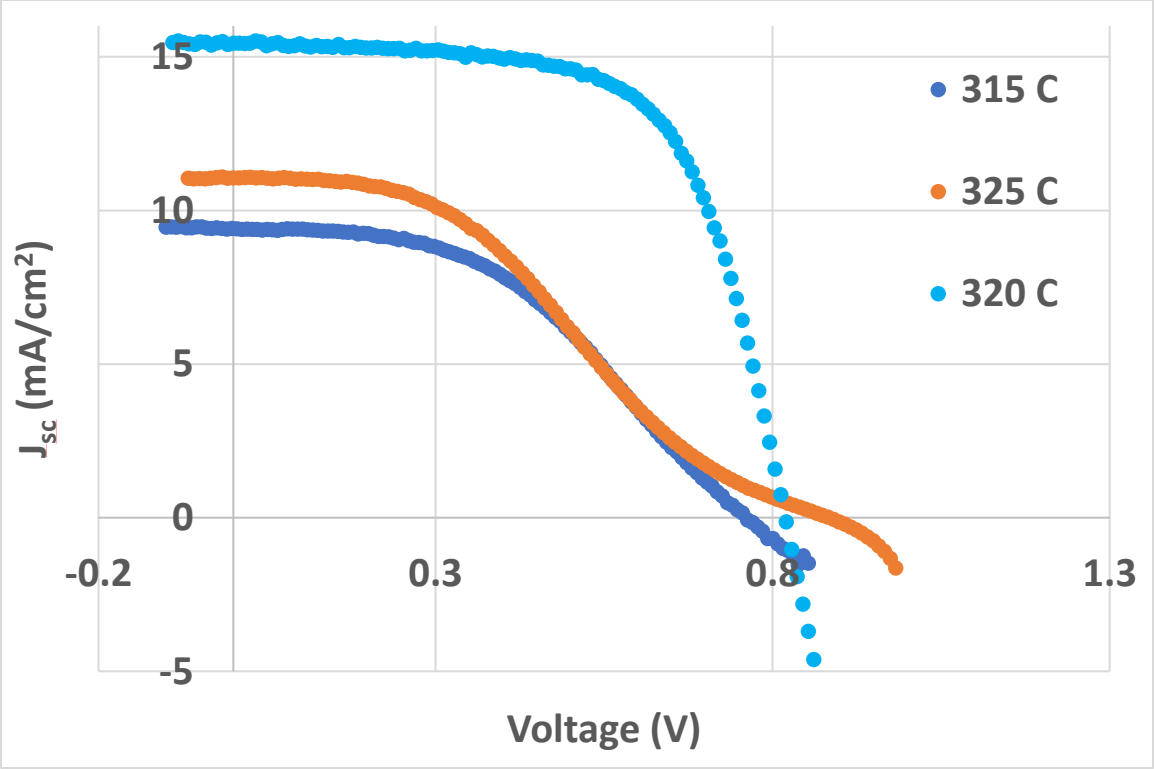

Figure 6.11: JV Characteristics for the device with the perovskite films annealed at different temperatures

6.3 Optimization of Perovskite Stoichiometry

Correct stoichiometric ratios of the precursors, PbI_2, and CsI are essential to prevent unreacted components from degrading the device performance in the solar cell. The sequential vapor deposition technique afforded precise nanometer level control of the thickness of the precursor layers. The stoichiometry of the perovskite layer was varied by holding the thickness of the PbI_2 precursor layer constant and varying the thickness of the CsI layer. We swept the stoichiometry of the perovskite layer from 0.8 CsI: 1.0 PbI_2 to 1.0 CsI: 1.0 PbI_2 and further to 1.2 CsI: 1.0 PbI_2 . We observed the best device performance for devices with the 1.0CsI : 1.0 PbI_2 ratio [Fig 6.12]. Excess PbI_2 has been shown to have passivating effects in several solution growth techniques, and such a phenomenon was not observed using vapor deposition.

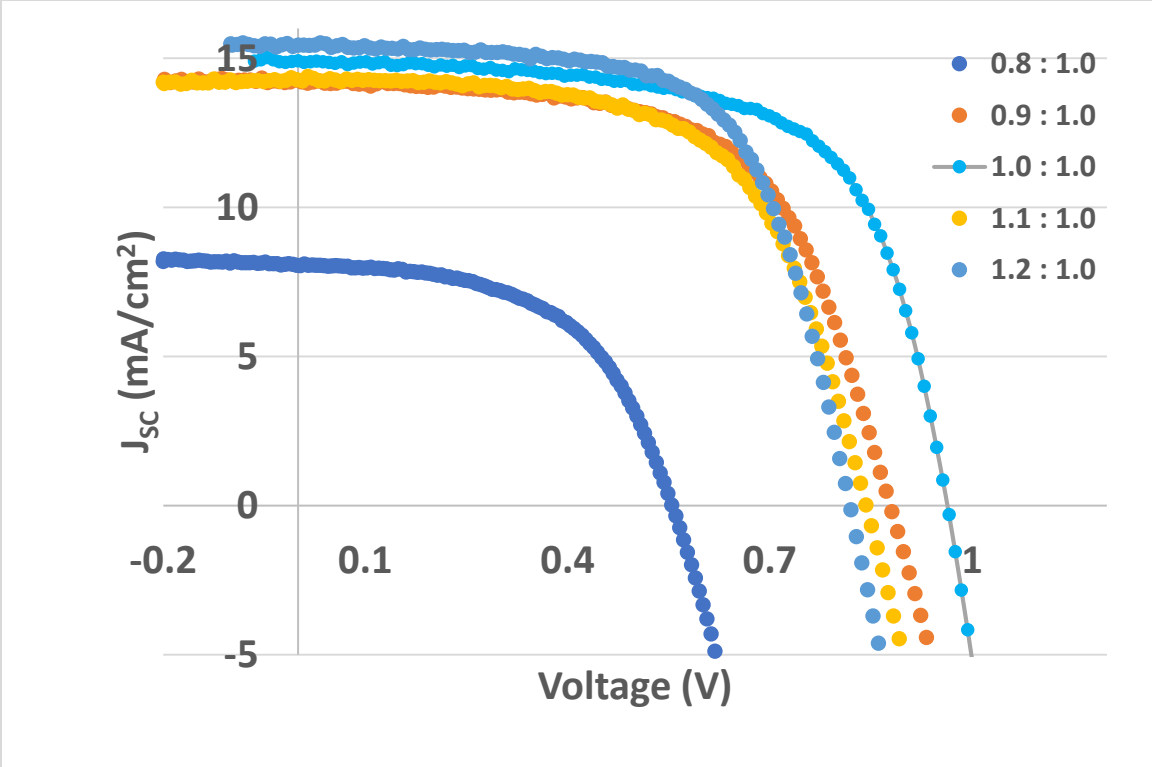

CsI: PbI_2	V_{OC} (V)	J_{sc} (mA/cm2)	FF	PCE (%)
0.8:1	0.55	8.0	54	2.5
0.9:1	0.88	14.4	61	7.7
1:1	0.95	14.9	65	9.4
1.1:1	0.85	14.2	61	7.5
1.2:1	0.83	15.4	65	8.2

Figure 6.12: JV Curves of the devices with various stoichiometries(CsI: PbI_2) for the perovskite layer

6.4 Optimization of Perovskite Layer Thickness

Optimal thickness of the absorber layer is another important parameter in efficient photoconversion efficiency of a solar cell. The absorber layer must be thick enough to collect all the light incident on it, but also be thin enough to ensure efficient charge collection and prevent unwanted recombination. The perovskite layer thickness was varied from 180nm to 300nm in 60nm steps. The JV characteristics and EQE with the various thicknesses are shown in Fig 6.13 and 6.14 respectively. The current density for the 240nm thick device is significantly higher than the 300n and 180nm devices. The EQE of the 180nm device falls off at >600nm, suggesting that the perovskite layer is unable to collect the longer wavelength light. The EQE of the device with 300nm is flat, showing no such drop below the band gap. However, the entire EQE of the device

is lower, suggesting charge collection issues. The EQE of the device with the optimal 240nm thickness shows high EQE of >75% throughout.

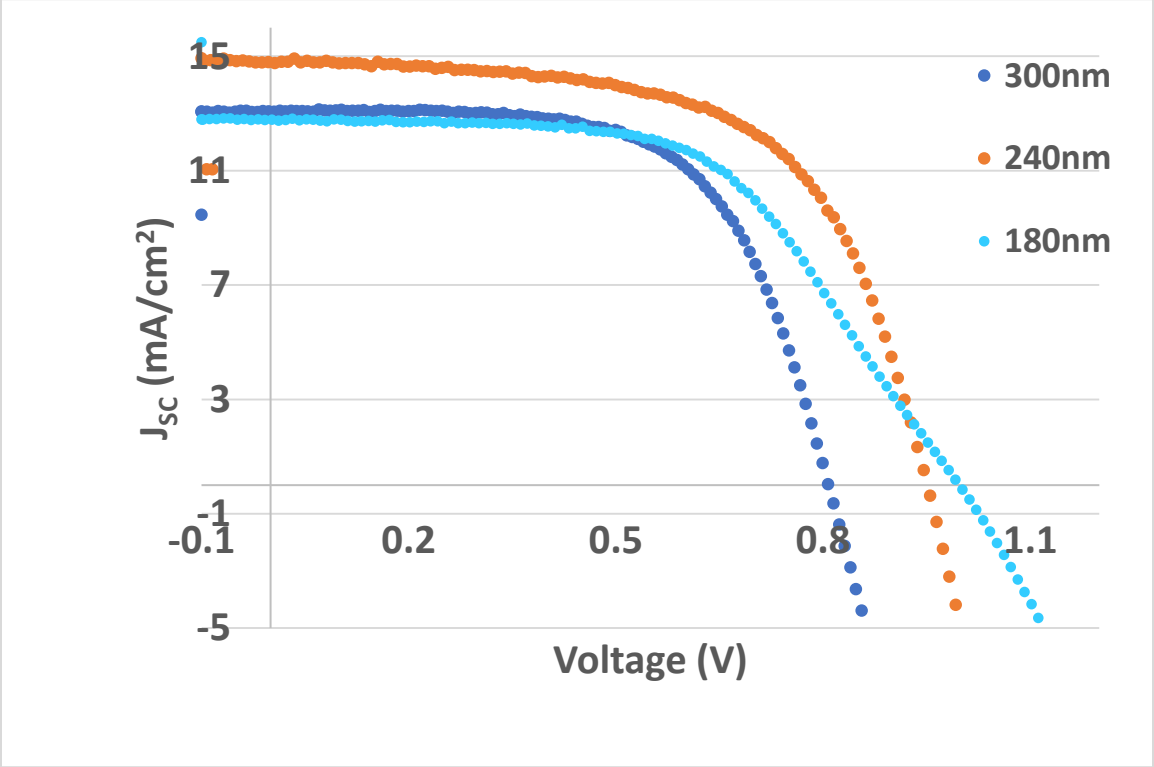

Figure 6.13: JV Curves and characteristics of the devices with various thicknesses of the perovskite layer

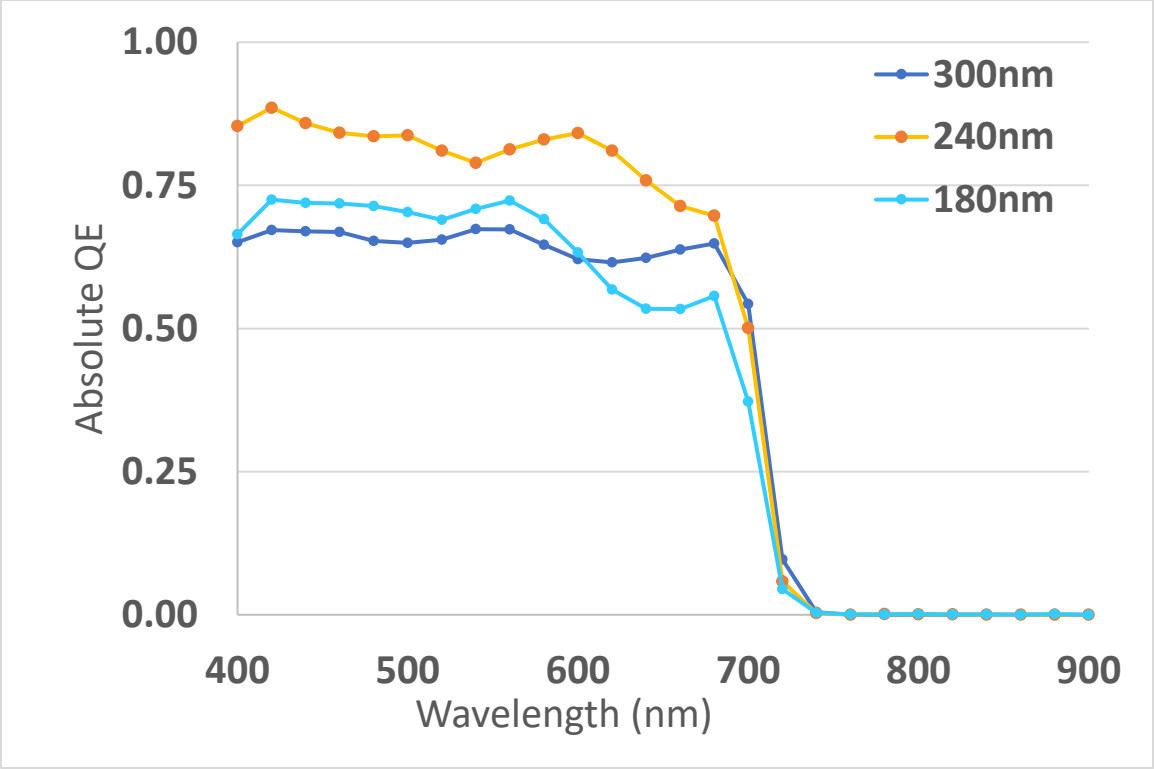

Figure 6.14: EQE of the devices with various thicknesses of the perovskite layer

Optimizing Substrate Temperature

Substrate temperature is a key parameter in controlling the rate of crystallization and thus the grain size of the perovskite material grown. It has been shown that higher substrate temperatures result in larger grain sizes with fewer grain boundaries, which leads to fewer recombination centers in the material and is beneficial to device performance. Devices with perovskite film grown at elevated temperatures of 100°C shows a much higher current density and V_{OC}. Our champion device has a current density of 15.8mA.cm2 and V_{OC} of 1.03V with a photoconversion efficiency of 11.2% [Fig 6.15 (100°C)]. This champion device represents the

highest such reported $CsPbI_3$ perovskite device with a p-i-n architecture as of 2018.

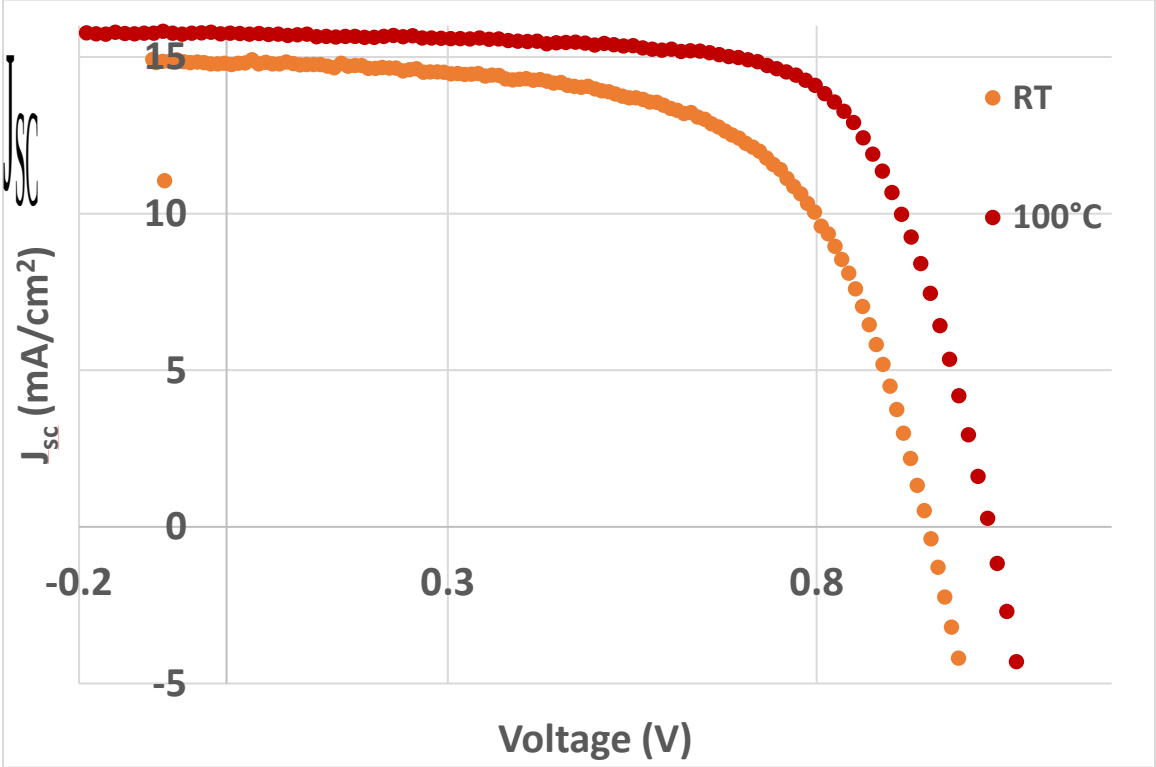

Substrate Temperature	VOC (V)	JSC (mA/cm2)	FF	PCE (%)
RT (25°C)	0.95	14.8	62	9.5
100°C	1.03	15.8	69	11.2

Figure 6.15: JV Curves and characteristics of the devices with the perovskite layer grown at different substrate temperatures

Characterization

One of the central advantages of the sequential vapor deposition grown perovskites is their reproducibility. The reproducibility of our vapor deposition process is illustrated in Fig 6.16, showing histograms of the JSC and V_{OC} of six consecutively deposited devices.

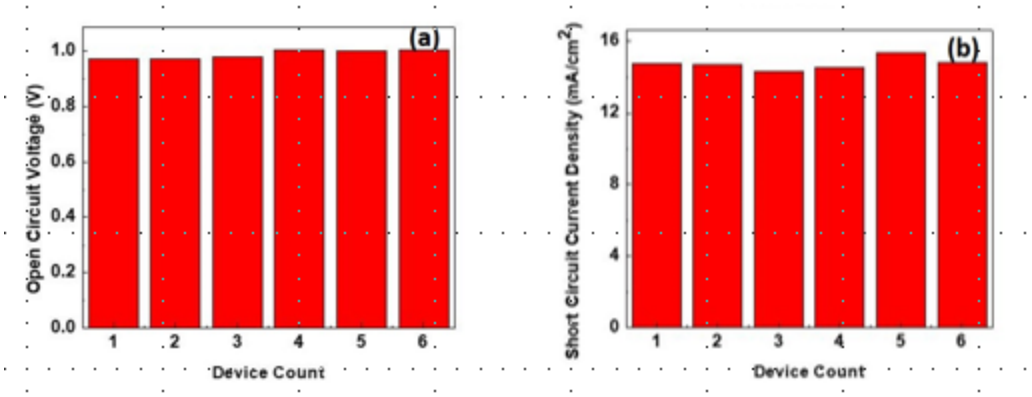

Figure 6.16: Reproducibility of vapor deposited $CsPbI_3$ showing histograms of the V_{OC} and J_{SC} of six consecutively deposited devices

The sum of doping and shallow defects of the $CsPbI_3$ device was determined from the Capacitance-Voltage measurements at 200kHz by plotting the $\frac{1}{C^2}$ vs V and calculating the slope of the linear region in the 0.1V -0.5V range [Fig 6.17]. The sum of doping and shallow defects of the $CsPbI_3$ is determined to be $2x10^{15}/cm^3$ range.

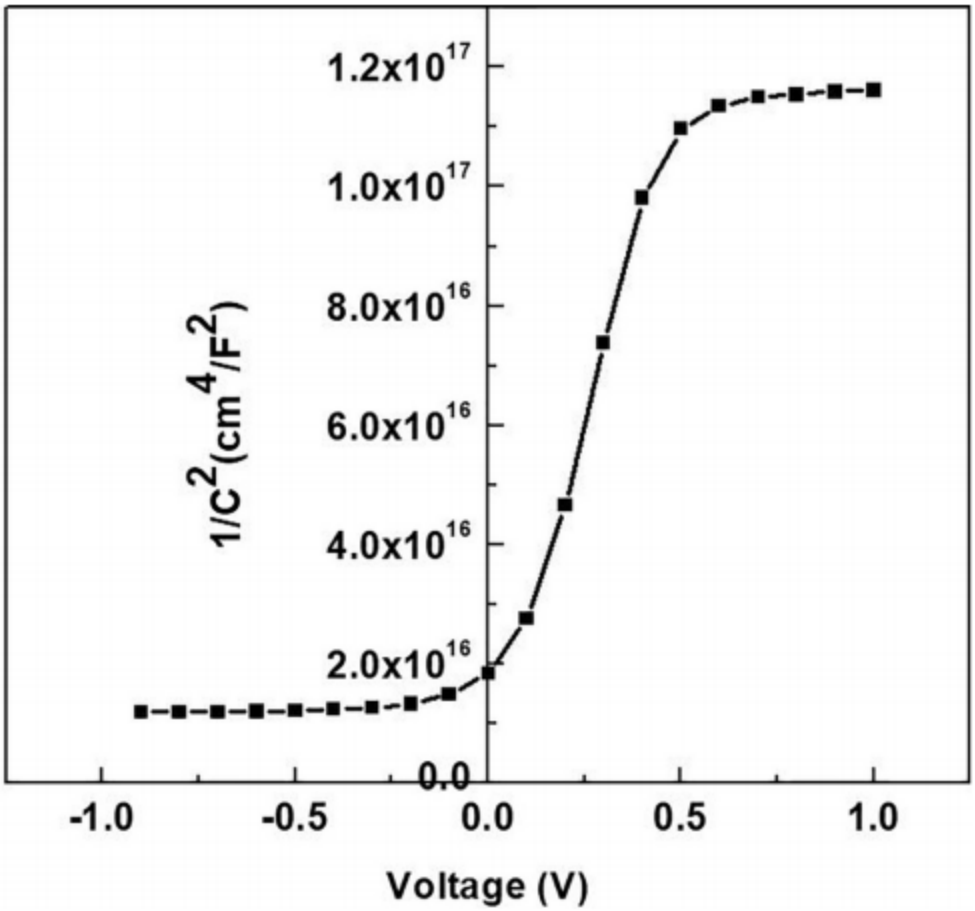

Figure 6.17:Plot of 1/C^2 vs V used to calculate the sum of doping and shallow defect density

The EQE of the champion cell is shown in Fig 6.18. The EQE remains flat over most of the spectrum, before sharply falling off at 700nm. As $CsPbI_3$ is a direct band gap material, the absorption coefficient(α) is given by,

$$\alpha = A\sqrt{(h\vartheta - E_g)}$$

where A is a constant dependent on the electron and hole mobilities, $h\vartheta$ is the energy of the photon, and $E_g$is the band gap of the absorber material. In this regime where the absorption coefficient is sharply falling off the QE~ αt, t being the thickness of the absorber. Plotting

(EQE* $h\vartheta$)^2 vs $h\vartheta$, we are able to extract the exact energy band gap of the material. Such a plot, called the Tauc plot, shown in Fig 6.19, displays the energy band gap of $CsPbI_3$ to be 1.74eV.

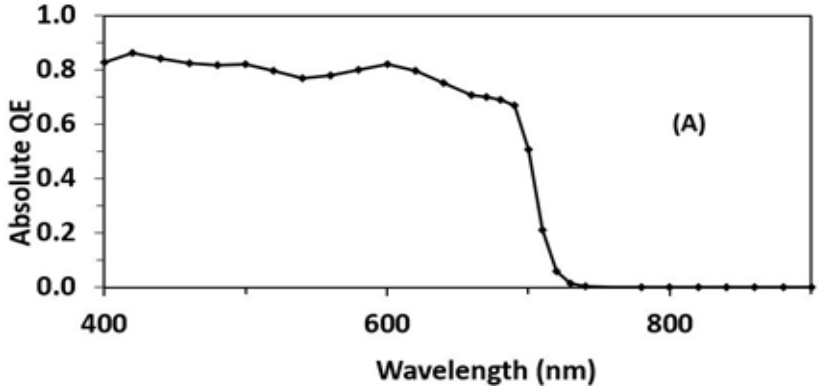

Figure 6.18: EQE of our champion device

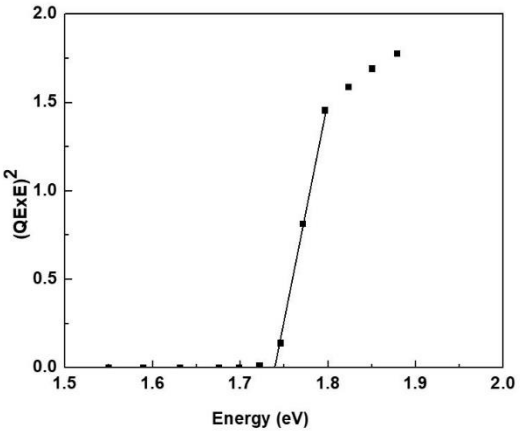

Figure 6.19:Tauc Plot used to calculate band gap

An energy band gap of 1.74eV gives a Shockley-Queisser theoretical limit of 28% for a single junction solar cell [Fig 6.20]. However, $CsPbI_3$ is a great candidate for a tandem solar cell acting

as a top cell with c-Si or CIGS as bottom cell. The theoretical efficiency of such a tandem solar cell could exceed 45% photoconversion efficiency [Fig 6.21]

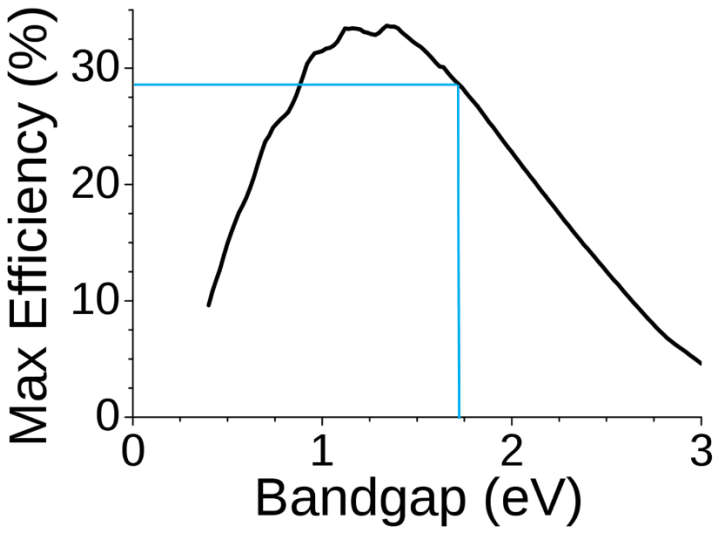

Figure 6.20:Shockley-Queisser limit for theoretical efficiency for a material with band gap of 1.74eV

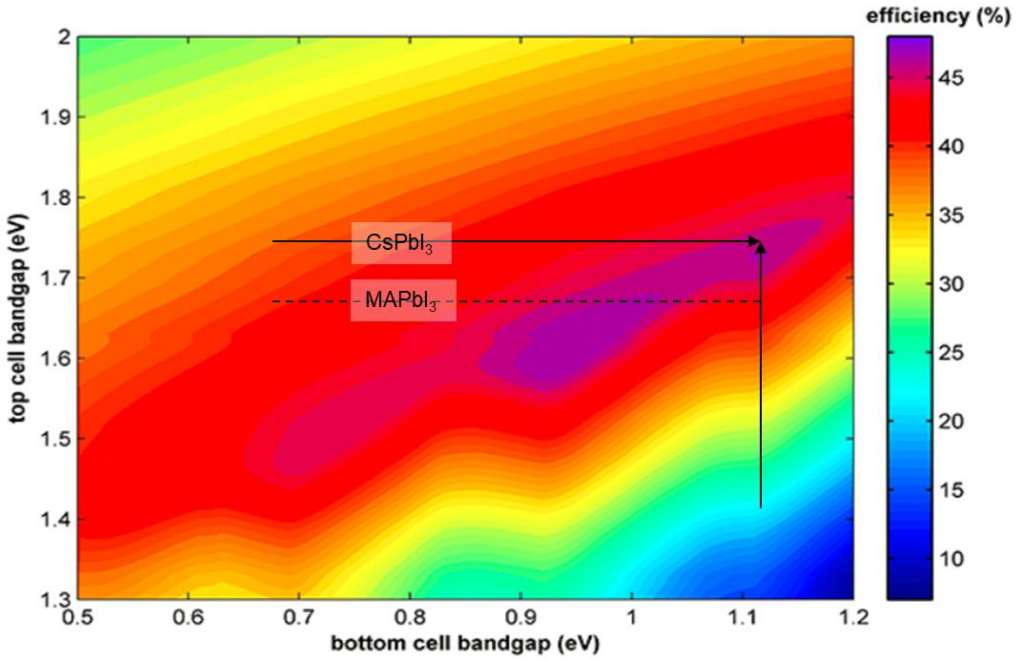

Figure 6.21: Theoretical efficiency for tandem solar cells with $CsPbI_3$ as top cell and c-Si as bottom cell

Problems with $CsPbI_3$

Although the α perovskite phase of the $CsPbI_3$ perovskite is stable at temperatures exceeding 300°C, at room temperatures the perovskite slowly transitions over days and weeks back to its thermodynamically favorable δ non-perovskite phase. The phase transition is understood to occur due to the slightly unstable cubic phase of the perovskite, which has a Goldschmidt Tolerance factor of 0.81. The presence of moisture further hastens this transition into the δ non-perovskite phase. The perovskite films degraded within minutes of exposure to ambient air. This not only makes $CsPbI_3$ unsuited for commercial deployment but also presents a significant challenge in characterization of the device outside the nitrogen ambient in the glovebox.

Closing remarks

This chapter describes the fabrication and characterization of the fully inorganic lead halide perovskite $CsPbI_3$ in search of a thermally stable perovskite composition. Although $CsPbI_3$ is stable at high temperatures, its instability at room temperatures and extreme moisture sensitivity make it an unsuitable candidate for large scale adoption.

The following chapter explores ways to resolve the issues faced with $CsPbI_3$.

CHAPTER 7. CESIUM LEAD MIXED HALIDE PEROVSKITE

7.1 Introduction

The instability of the α-perovskite phase of $CsPbI_3$ perovskite results from the instability of its cubic perovskite crystal structure. The Goldschmidt Tolerance Factor is given by [1,2],

$$\text{Goldschmidt Tolerance Factor}, t = \frac{r_A + r_X}{2\sqrt{(r_B + r_X)}}$$

where r_A, r_B, and r_X are the ionic radii of the A cation, B cation, and the X anion respectively. For a stable cubic perovskite crystal structure, the Goldschmidt Tolerance Factor must lie between 0.81 and 1.11. The Goldschmidt Tolerance Factor of $CsPbI_3$ at 0.80 falls just outside this acceptable range, resulting in the α- phase of $CsPbI_3$ slowly transitioning back into its undesirable δ-non-perovskite phase. To improve the thermodynamic stability of the perovskite material at room temperatures, two strategies can be employed to increase the Goldschmidt Tolerance Factor above the lower limit of 0.81.

1. **Substituting the Cesium ion with a larger cation**

   Cesium has a small ionic radius of 1.67Å[Table 1]. Substituting Cesium with a different cation from the same Group in the periodic table (Group 1) with a larger ionic radius would be able to increase the Goldschmidt Tolerance Factor [Fig 7.1]. As Rubidium and Potassium are higher up on the periodic table, they a smaller ionic radius of 1.52Å and 1.38Å respectively. The only Group 1 element with a larger ionic radius is Francium, an extremely radioactive element.

	Ion type	Ionic Radius (Å)
A-cation	Cs^+	1.67
	Rb^+	1.52
	NH_4^+	1.46
	MA^+	2.17
X-Halide	I^-	2.20
	Br^-	1.96
	Cl^-	1.84

Figure 7.1: Table of ionic radii for common perovskite compositions

Cesium could be replaced with organic cations such as methylammonium (MA) or formamidium (FA), which haver larger ionic radii of 2.17Å and 2.53Å respectively; however, that would be antithetical to our goal of thermal stability with fully inorganic perovskites.

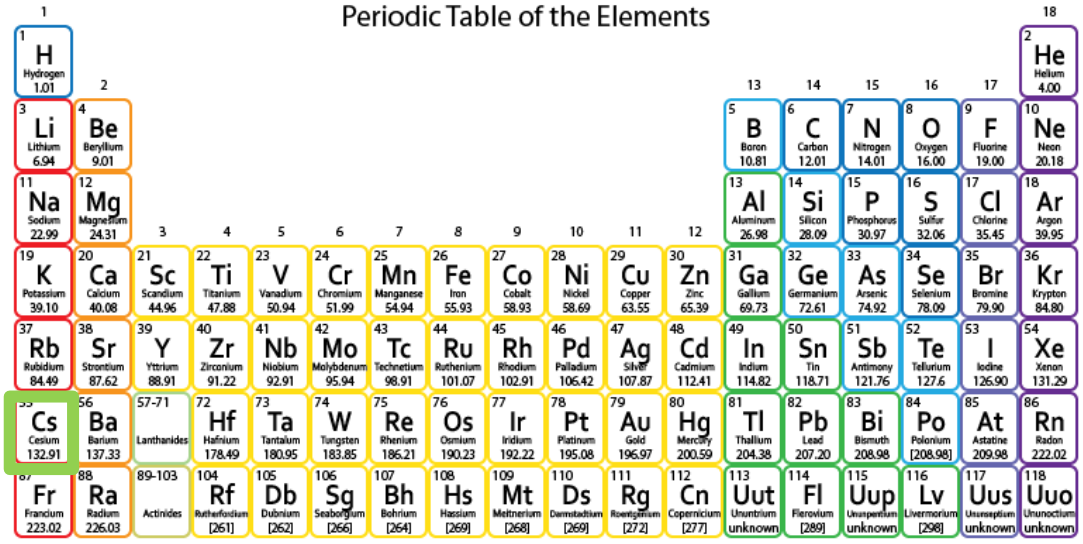

Figure 7.1: Periodic table of elements showing the position of Cesium

2. Substituting the Iodine with a smaller halide

Another strategy to improve the Goldschmidt Tolerance Factor is to reduce the size of the halide octahedra by replacing the bulky Iodine ion with a smaller Bromine or Chloride ion [3,4]. While this substitution would increase the Goldschmidt Tolerance Factor and thus the stability of moisture and temperature, it would come at the cost of the band gap increasing. Fig. 7.2 shows the absorption spectra of mixed halide perovskite compositions, $CsPb(Br_xI_{1-x})_3$. As the bromine content is increased from 0 to 1, the absorption onset shifts from 700 nm for a completely iodide composition all the way to 540nm for a completely bromide composition [5].

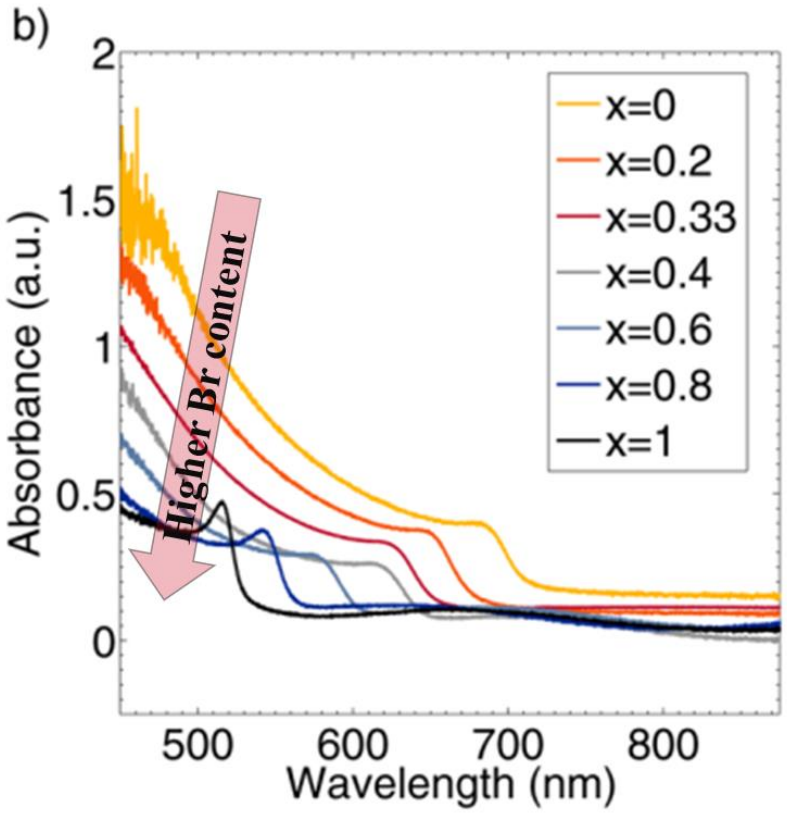

Figure 7.2: Absorption spectra of mixed halide perovskite compositions, $CsPb(Br_xI_{1-x})_3$, showing the absorption onset shifting to lower wavelengths with increasing Br content

CsPbbr3, for example, where all of the iodine is replaced with bromine, is insensitive to moisture and high temperatures. Cspbr3 is both stable at room temperatures and does not undergo thermal degradation up to 500+ °C [6]. However, the energy band of 2.3eV of Cspbbr3 makes it unsuitable for photovoltaic application due to its inability to collect most of the visible and IR spectrum of incident light [7] .

Partial substitution of the iodine with bromine, however, affords us the advantages of both moisture and thermal stability while keeping the energy band gap in the photovoltaically useful range. $CsPbI_2Br$, for example, where only 33% of the I is replaced with Br, has a band gap of ~1.8 - 1.9eV depending on the deposition method and thus showings great potential for a tandem and semi-transparent photovoltaic application. Further, the incorporation of the smaller bromide ion decreases the size of the halide cage structure, PbX6, and increases the effective Goldschmidt Tolerance Factor up to 0.85. The increased effective Goldschmidt Tolerance Factor affords the perovskite crystal with enhanced stability to moisture and thermal degradation.

The several advantages of the fully inorganic mixed halide perovskite, $CsPbI_2Br$, convinced us to further research this composition and fabricate devices with a strong focus on their thermal stability.

7.2 Deposition Chamber Modification

Through our work on $CsPbI_3$, we developed a thorough understanding of the importance of precise thickness control of precursor layers on device performance. We wanted to be able to deposit extremely thin layers of precursors, several nanometers thick, to control stoichiometry and precursor intercalation well. The main issue we faced with our current deposition system was that the two Luxel furnaces with the precursors had to be heated up sequentially rather than at the same time. With the current system, we were able to deposit 20-30nm of each precursor

layer over eight deposition cycles to obtain 400nm thick perovskite layers, which took 2-3 hours. To better control stoichiometry and intercalation of the precursor layers necessitated that we create thinner layers, which, with the older deposition setup, would take 7-8 tedious hours of sequential heating of the two Luxel furnaces. To resolve this issue required that we design and install custom shutters above the Luxel furnaces to control the deposition of precursor layers; with this new deposition setup [Fig 7.3]. With the new source shutters ensuring that the temperature of the Luxel furnaces need not be lowered from its operating temperatures down to its holding temperatures during a deposition process, the entire deposition process took less than 90 minutes. Fig 7.3 shows the interior of the deposition chamber before and after the modifications.

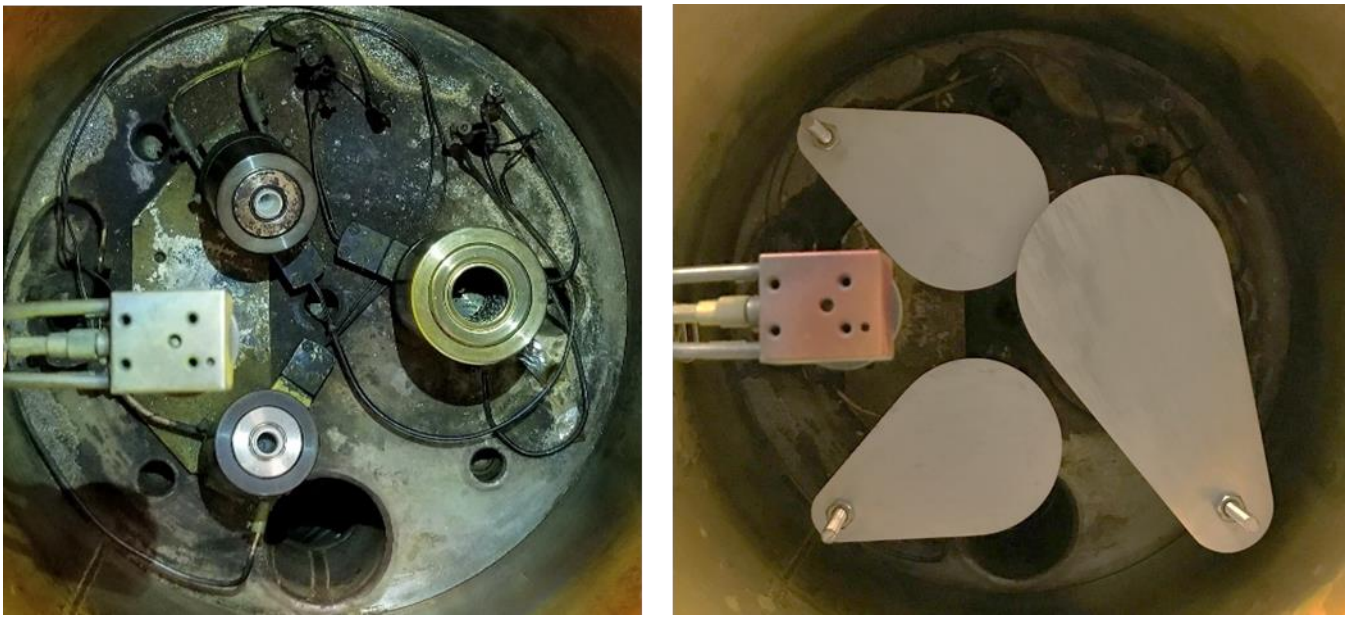

Figure 7.3: Interior of the deposition chamber before (a) and after (b) modifications to install source shutters

7.3 Device Optimization

. 7.3.1 p-i-n Device Architecture

Following our success with p-i-n device architecture for $CsPbI_3$ perovskite devices, we fabricate $CsPbI_2Br$ perovskite devices with the ITO/PTAA/ $CsPbI_2Br$ /PCBM/Al structure. The perovskite layer was grown with PbI_2 and CsBr as our precursor materials. The film was subjected to anneals at 275°C for 5 minutes in a nitrogen glove box to form the perovskite layer. The Electron transport and hole transport layers of PCBM and PTAA were spin-coated using the same recipe as the one used for $CsPbI_3$. Device characteristics are shown in Fig. 6.6. The valence band mismatch with PTAA and perovskite absorber layer is larger for $CsPbI_2Br$ than $CsPbI_3$ and thus the V_{OC} of the device was only 0.89V compared to its energy band gap of 1.8eV [Fig 6.7].

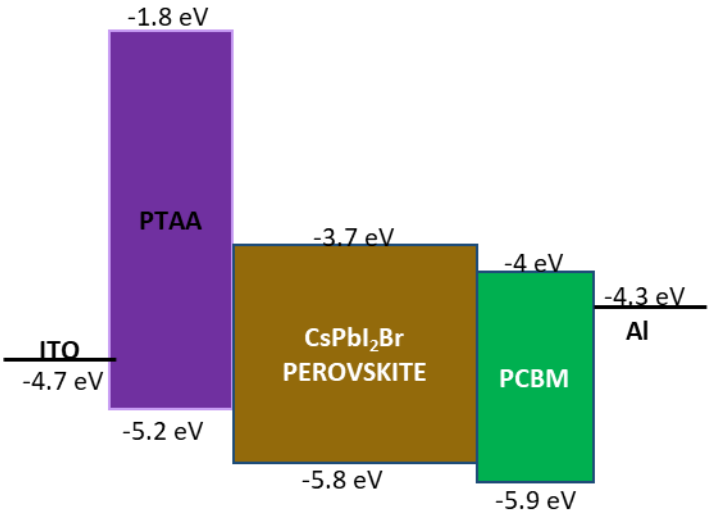

Figure 7.4: Energy band diagrams for p-i-n devices with PTAA as HTL and PCBM as ETL

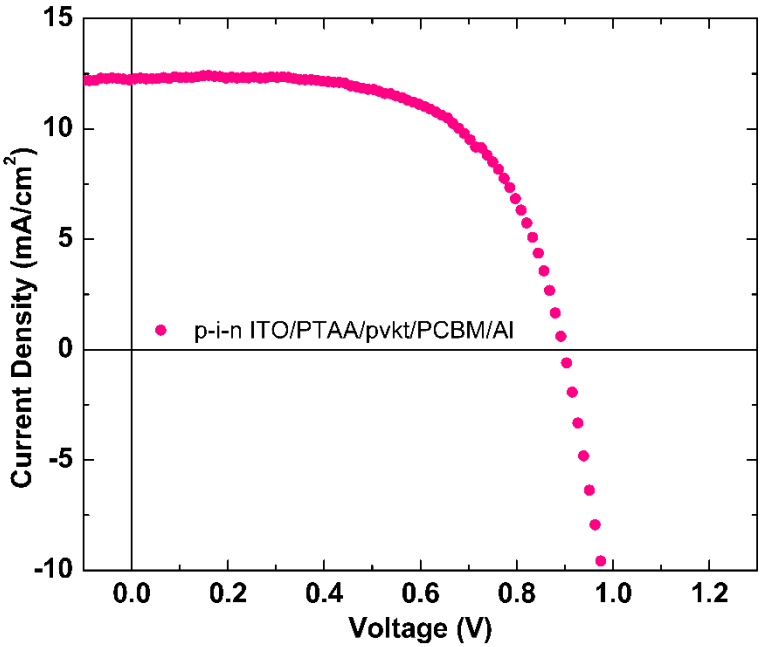

V_{OC} (V)	J_{SC} (mA/cm^2)	FF (%)	PCE (%)
0.89	12.26	63	6.89

Figure 7.5: JV characteristics of p-i-n device

Further, devices with an organic hole transport layer (such as PTAA) were unsuitable for prolonged high temperature anneals as the organic semiconductors degraded at these high temperatures. To study high temperature anneal conditions for the perovskite layers, it was important to switch to an n-i-p device architecture with an inorganic semiconductor Cadmium Selenide as the bottom transport layer.

7.3.2 n-i-p Device Architecture

Devices with the n-i-p device architecture were grown on a FTO coated glass substrate cleaned using a 5% surfactant solution, deionized water, methanol, and acetone. In:CdS is the

preferred electron transport layer due to its low absorption in the visible spectrum and good match with the energy band structure of $CsPbI_2Br$ [Fig 7.6]. Thin layers (35nm) of In:CdS were deposited using the vapor deposition system at rate of 0.5Å/s. The In:CdS was annealed in air at 400°C for 30 minutes to promote grain size enhancement. The FTO/In:CdS substrate was transferred into our perovskite deposition system. Layer-by-layer sequential growth was used to deposit the perovskite precursors, following which the film was annealed at 300°C for 10 minutes in a nitrogen glove box. The hole transport layer of P3HT was spin coated using a 15mg/mL solution in chlorobenzene at 2000RPM for 40s and annealed at 150°C for 10minutes. Gold was evaporated onto the P3HT layer using a substrate mask to define the device area using a physical vapor deposition.

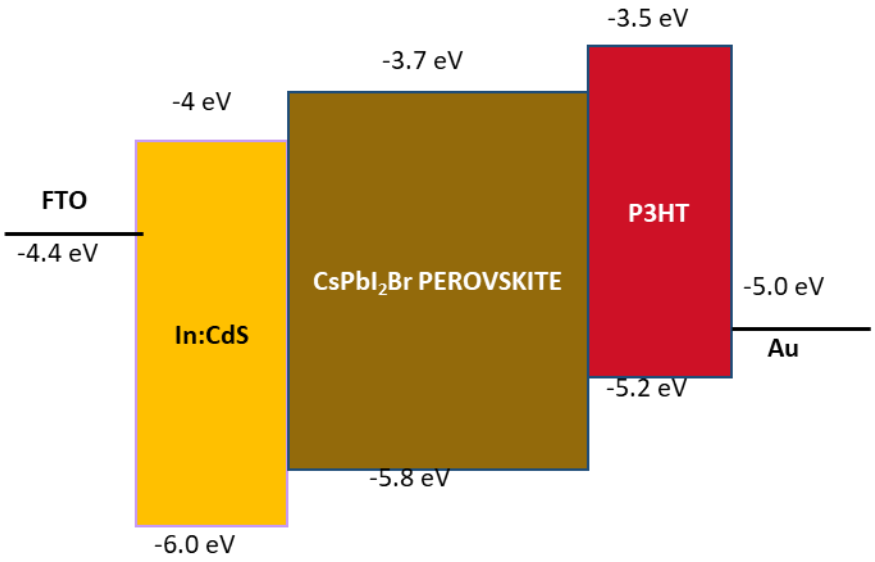

Figure 7.6: Energy band structure of n-i-p devices with FTO/In:CdS/pvkt/P3HT/Au structure

Our initial devices with the new n-i-p device architecture performed poorly compared to our p-i-n devices. Fig. 7.7 shows the comparison of our n-i-p and p-i-n device architecture where

the perovskite layer was deposited using the same exact deposition conditions: 400nm thick perovskite, annealed at 275°C for 10 minutes. Figure 7.7 clearly shows that although the V_{OC} of the n-i-p device was slightly higher owing to the better band gap match of In:CdS with perovskite, both the J_{SC} and FF were significantly worse.

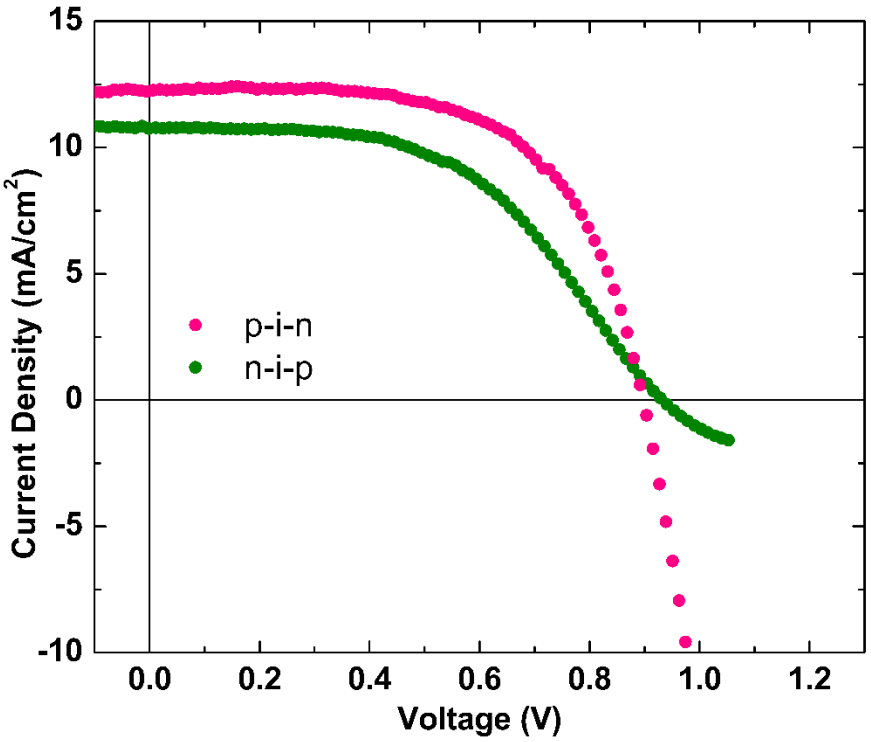

Device Architecture	V_{OC} (V)	J_{SC} (mA/cm^2)	FF (%)	PCE (%)	RSR (Ω)
p-i-n	**0.89**	**12.26**	**63**	**6.89**	**90**
n-i-p	**1.01**	**10.7**	**50**	**5.10**	**2000**

Figure 7.7: JV characteristics of p-i-n and initial n-i-p device

Firstly, to understand the lower J_{SC} we looked at the EQE of our n-i-p and p-i-n devices with the same perovskite layer [Fig 7.8]. The n-i-p devices had a lower EQE between 400 and 500nm as compared to the p-i-n devices. The lower EQE at these wavelengths results from the

absorption of light by the In:CdS layer at these wavelengths as seen by the transmission spectra of In:CdS in Figure 7.8. PTAA, on the other hand, with a large band gap of 3eV, absorbs almost no light in the visible spectrum.

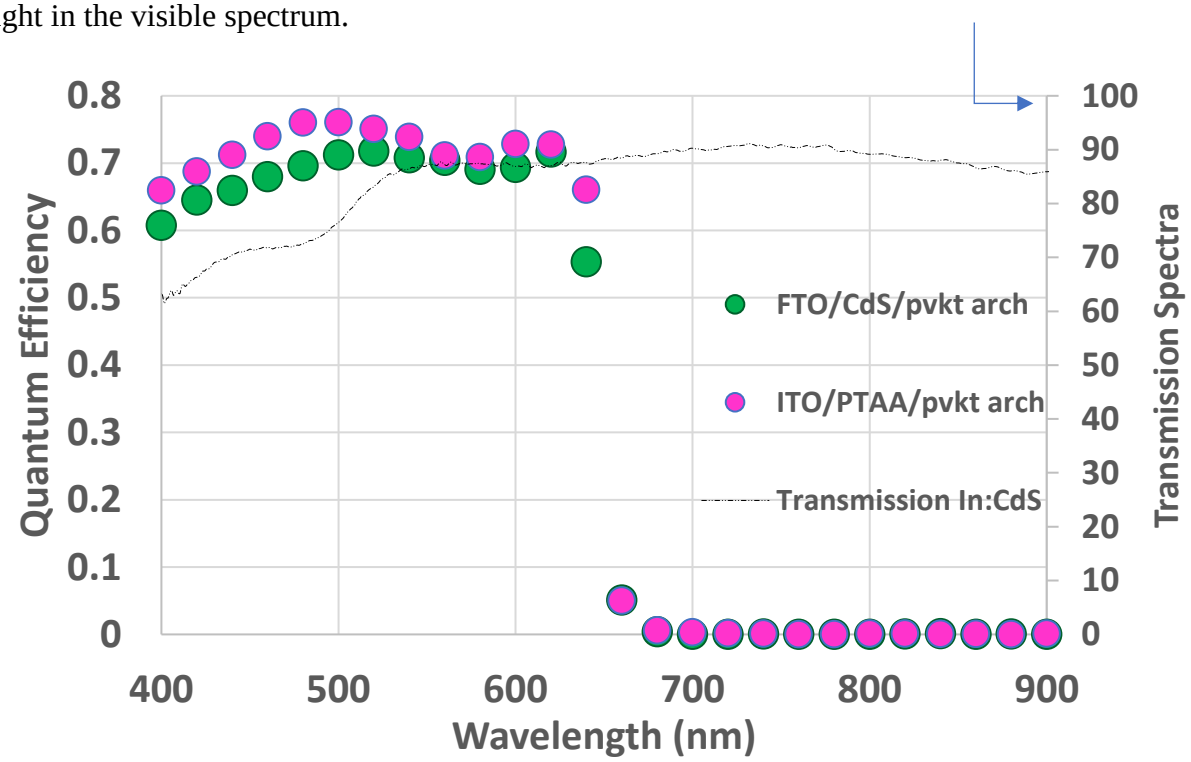

Figure 7.8: EQE of p-i-n and n-i-p device showing lower EQE for n-i-p devices due to low transmission of In:CdS in the 400-500nm range

Secondly, the n-i-p devices had a much higher series resistance that lowered the FF and in turn the photoconversion efficiency of the solar cell. To address the origin of this high resistance, we performed a series of experiments by replacing each of the transport layers and looking at their series resistances.

Replacing In:CdS with aluminum doped Zinc oxide (Al:ZnO) resulted in similar large series resistances as seen in Figure 7.9. This indicated to us that the series resistances were

arising from either the interface between the perovskite and P3HT layer or the interface between the P3HT and gold layer.

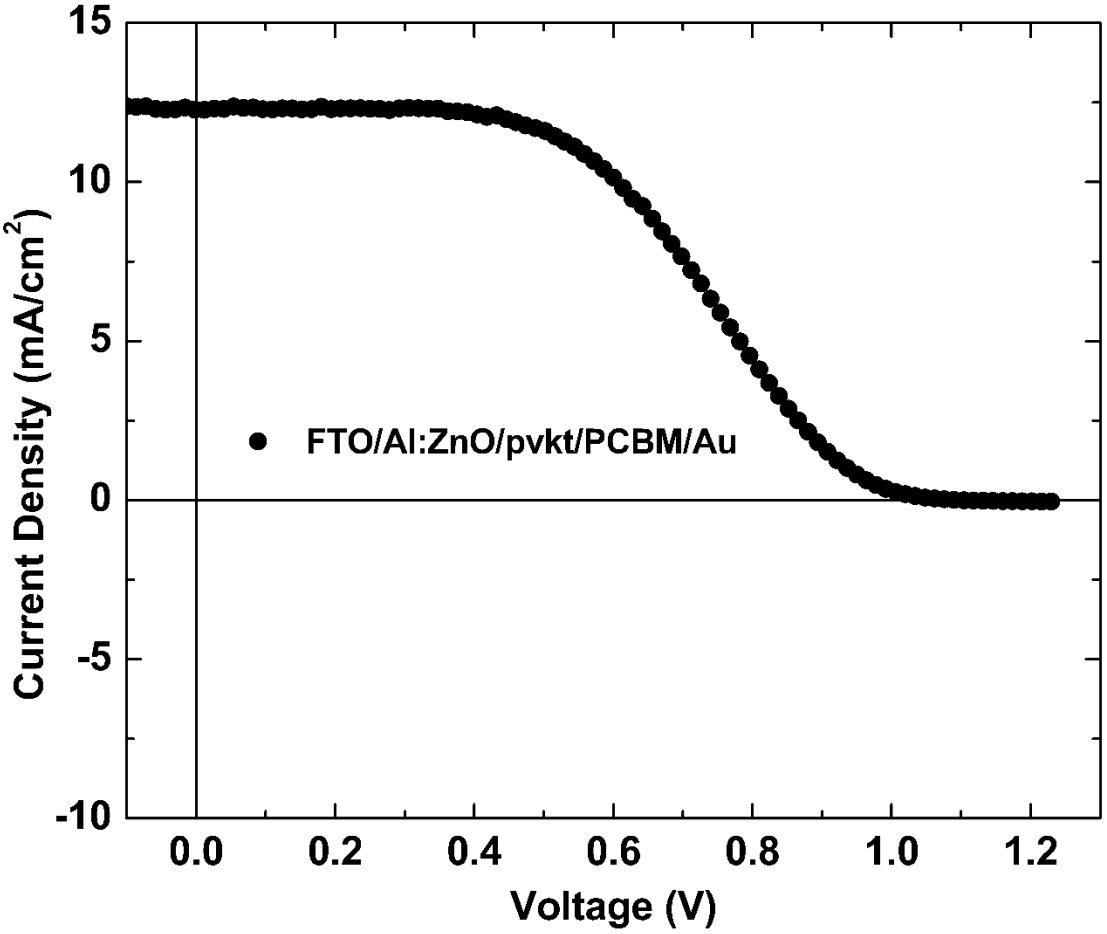

Figure 7.9: JV Characteristic of n-i-p device with Al:ZnO replacing In:CdS as ETL

Annealing the P3HT layer at 250°C instead of the standard 150°C for 10 minutes did not reduce the series resistance issue [Fig 7.10], which suggested that the series resistance issue was emanating from the interface of the P3HT with gold.

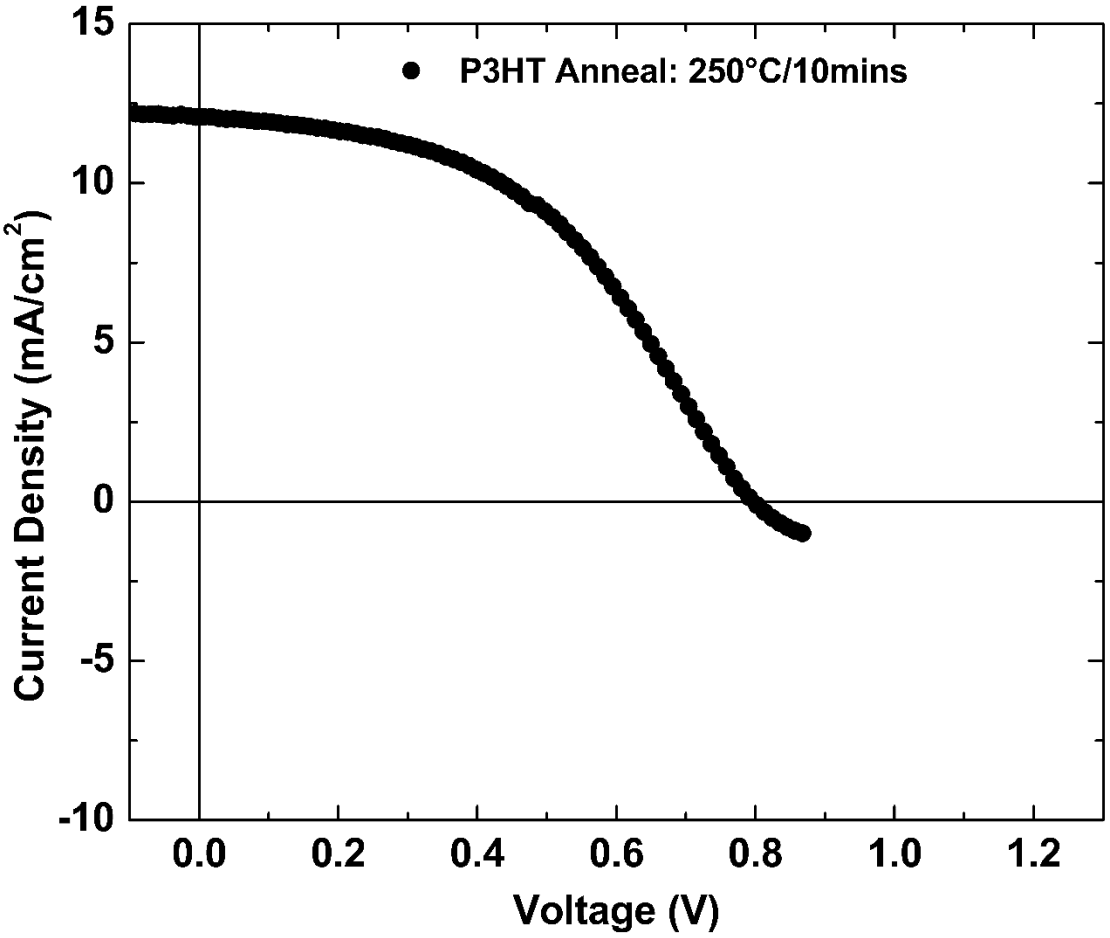

Figure 7.10: JV characteristics of P3HT annealed at 250°C showing high series resistance

Upon annealing the device after the gold deposition at 225°C for 10 minutes, we were able to completely remove the series resistance as seen in Fig 7.11. The reduction of the series resistance massively improves both the FF as well as the PCE of the device and pushes it beyond the PCE of the p-i-n device architecture.

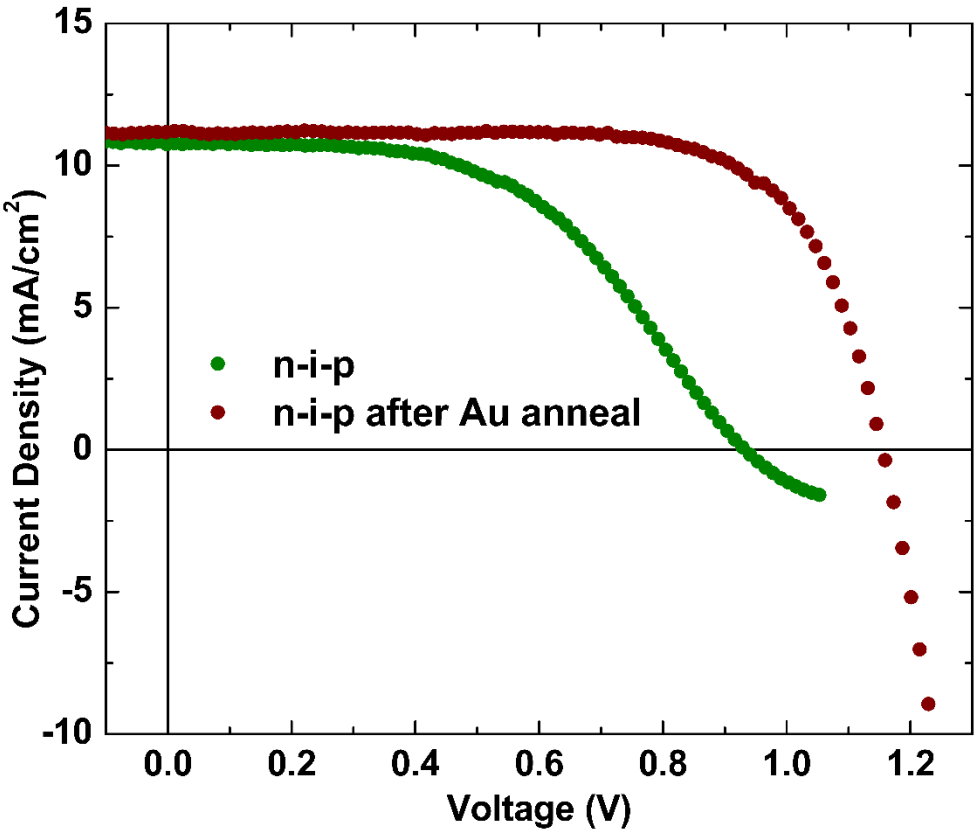

	V_{OC} (V)	J_{SC} (mA/cm^2)	FF (%)	PCE (%)	R_S (Ω)
After Fabrication	**1.01**	**10.7**	**50**	**5.10**	**2036**
Gold Anneal 225°C/15mins	**1.16**	**11.13**	**71**	**9.16**	**92**

Figure 7.11: Comparison of n-i-p device before and after annealing the device showing the massive change in series resistance

7.3.2 Precursor Layer Thickness

The thickness of the precursor layer plays an important role in the crystallization process of the perovskite. Thinner precursor layers improve intermixing and ensure a fully homogenous perovskite layer. Thicker precursor layers, on the other hand, require longer and higher temperature anneal conditions to fully form the perovskite layer. Here, we look at the device performance gains using thinner precursor layers, enabled by the deposition system modification we made discussed in Section7.2. Thick precursor layers, in this case 20nm of CsBr and 30nm of PbI_2, needed higher anneal temperatures of 350°C to completely form the perovskite layer as compared to 300°C for thinner precursor layer with 4nm of CsBr and 6nm of PbI_2. Devices with thick and thin precursors were made with constant overall thickness of 400nm, and their device

characteristics were compared [Fig 7.12]. Thin precursor layer devices had both higher J_{SC} and V_{OC} due to the better intermixing of the precursor materials to form the perovskite layer.

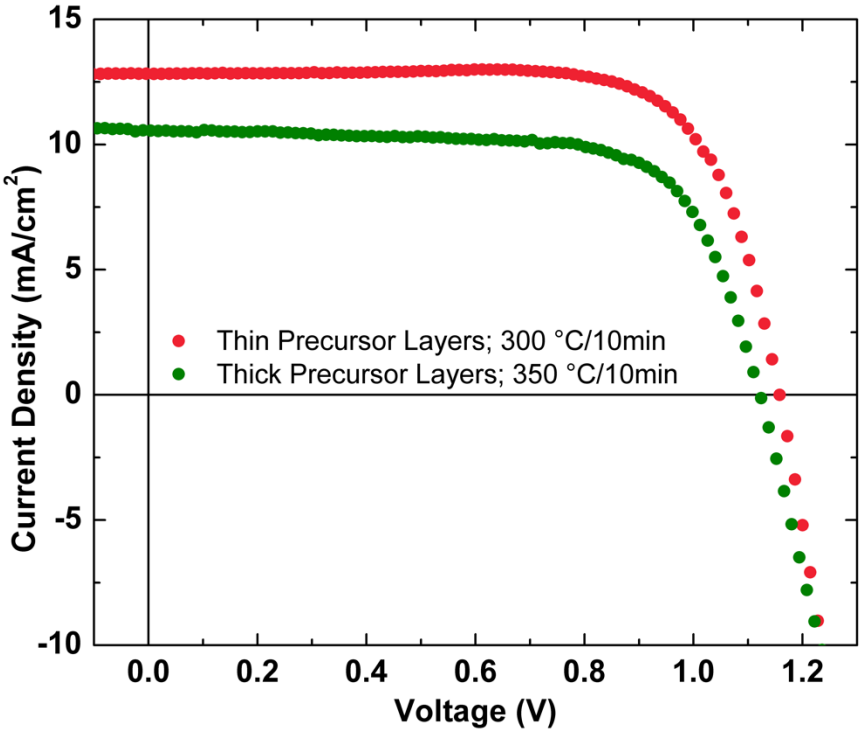

	V_{OC} (V)	J_{SC} (mA/cm^2)	FF (%)	PCE (%)
Thin precursor	**1.16**	**12.83**	**74**	**10.98**
Thick precursor	**1.12**	**10.55**	**70**	**8.34**

Figure 7.12: Device performance improvements with thin precursor layers

7.3.3 Stoichiometry Variations in the Perovskite Layer

The correct stoichiometry of the perovskite layer is even more important in the case of a mixed halide perovskite. Here, we varied the stoichiometry of the perovskite by varying the

thickness of the PbI_2 and CsBr layers. Derives with 5% excess CsBr and 5% excess PbI_2 were compared with the correct stoichiometry devices. The IV characteristics show that for the devices with excess lead iodide, a hump in the JV curve is observed, possibly due to the unreacted PbI_2 component in the active layer [Fig 7.13]. Devices with excess CsBr show a reduced J_{SC} possibly due to the increased band gap of the material as the bromine content increases.

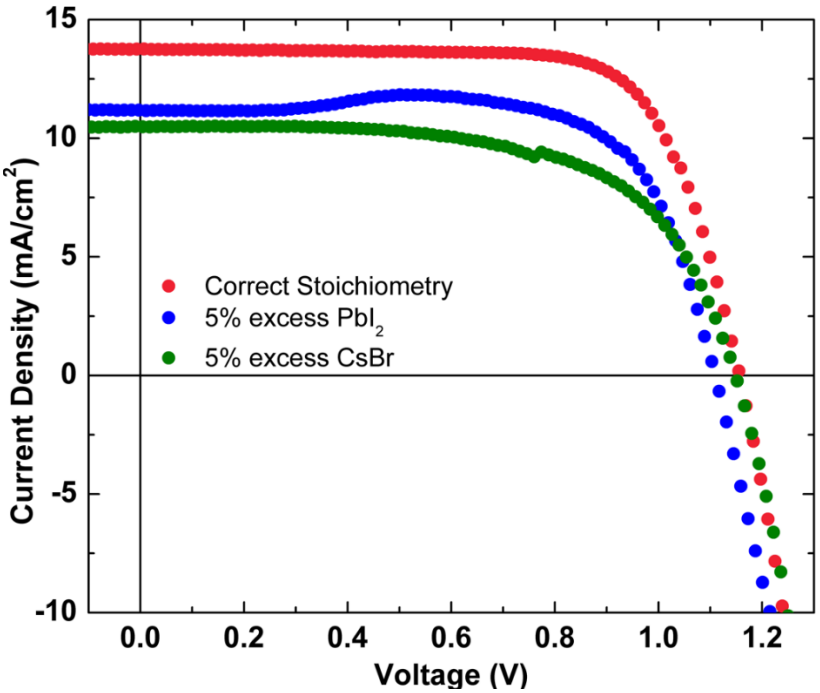

	V_{OC} (V)	J_{SC} (mA/cm^2)	FF (%)	PCE (%)
Correct Stoichiometry	**1.16**	**13.76**	**73**	**11.58**
5% excess PbI_2	**1.10**	**11.19**	**73**	**9.04**
5% excess CsBr	**1.15**	**10.48**	**62**	**7.54**

Figure 7.13: JV characteristics showing the effect of perovskite layer stoichiometry on device performance

7.3.4 Perovskite Layer Thickness

The total thickness of the perovskite layer was varied from 200nm to 400nm. The JV characteristics [Fig 7.14] and EQE of the resultant devices [Fig. 7.15] show clearly the importance of the perovskite layer thickness. Devices with perovskite layers of 200nm and 300nm are unable to collect long wavelength light incident, as seen in the EQE curve at 500-650nm. The EQE of the 400nm device is relatively flat with EQE of >80% over all wavelengths, and the J_{SC} is higher than the thinner devices.

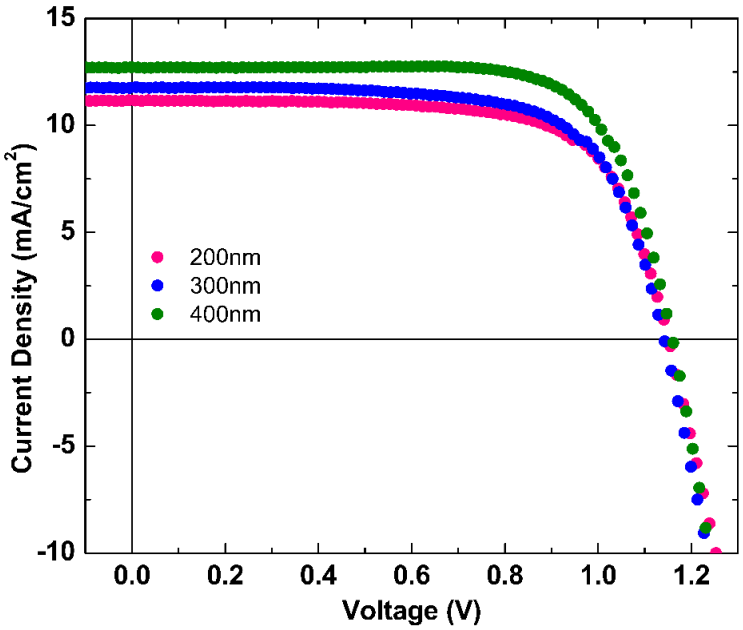

Perovskite layer thickness	J_{SC} (mA/cm^2)
200nm	11.16
300nm	11.79
400nm	12.72

Figure 7.14: JV characteristics of devices with varying perovskite layer thicknesses

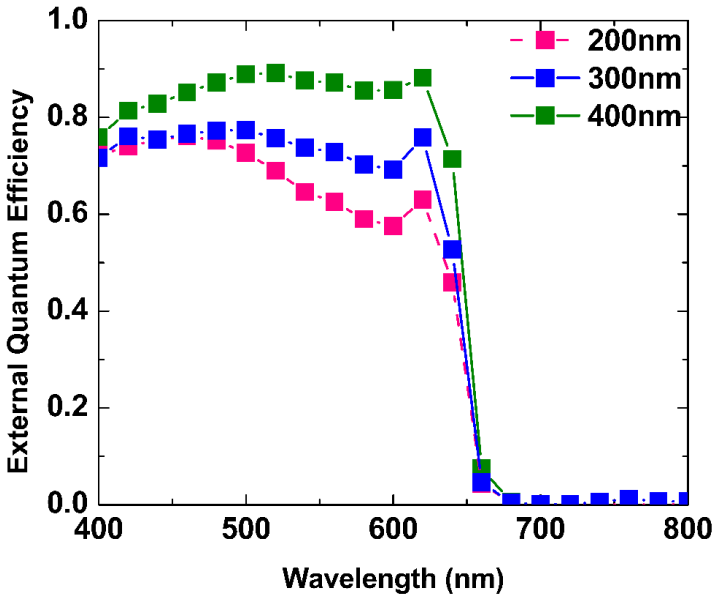

Figure 7.15:EQE of devices with varying perovskite layers

7.3.5 Perovskite Anneal Conditions

Anneal conditions during the perovskite formation play an important role in the crystallization of the perovskite material. Here, we deposited thin precursor layers (4nm: CsBr and 6nm: PbI_2) and experimented with anneal temperatures from 200°C to 350°C. Anneals at 200°C were insufficient for the complete formation of the perovskite layers; these films looked yellow and partially transparent owing to the incomplete phase transition into the α perovskite phase from the δ non-perovskite phase [Fig 7.16]. Anneals at 250°C and higher showed complete phase transition. The JV characteristics of the devices with various anneal conditions are shown in Fig 7.17. Devices with anneals at 200°C showed a significantly smaller J_{SC} owing to the incomplete phase transition into the α phase. 300°C anneals appear to be the

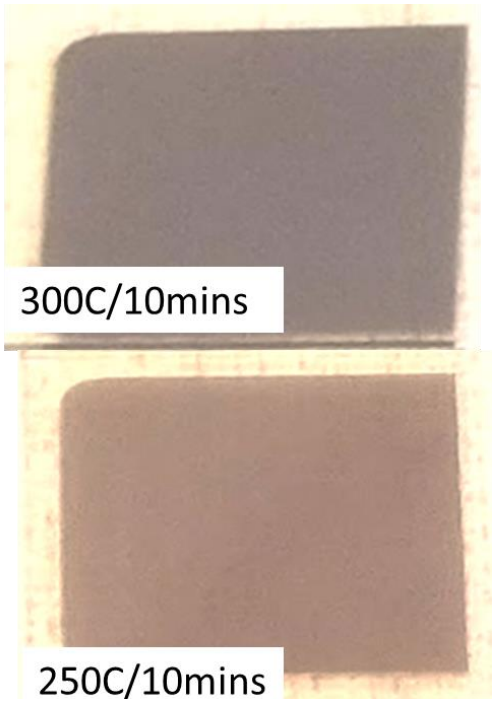

Figure 7.16: Perovskite films annealed at 300°C showing complete transformation and 250°C showing incomplete transformation into perovskite

optimum anneal temperature from the JV characteristics. At even higher temperatures, the films start looking grayish and their V_{OC} drops significantly.

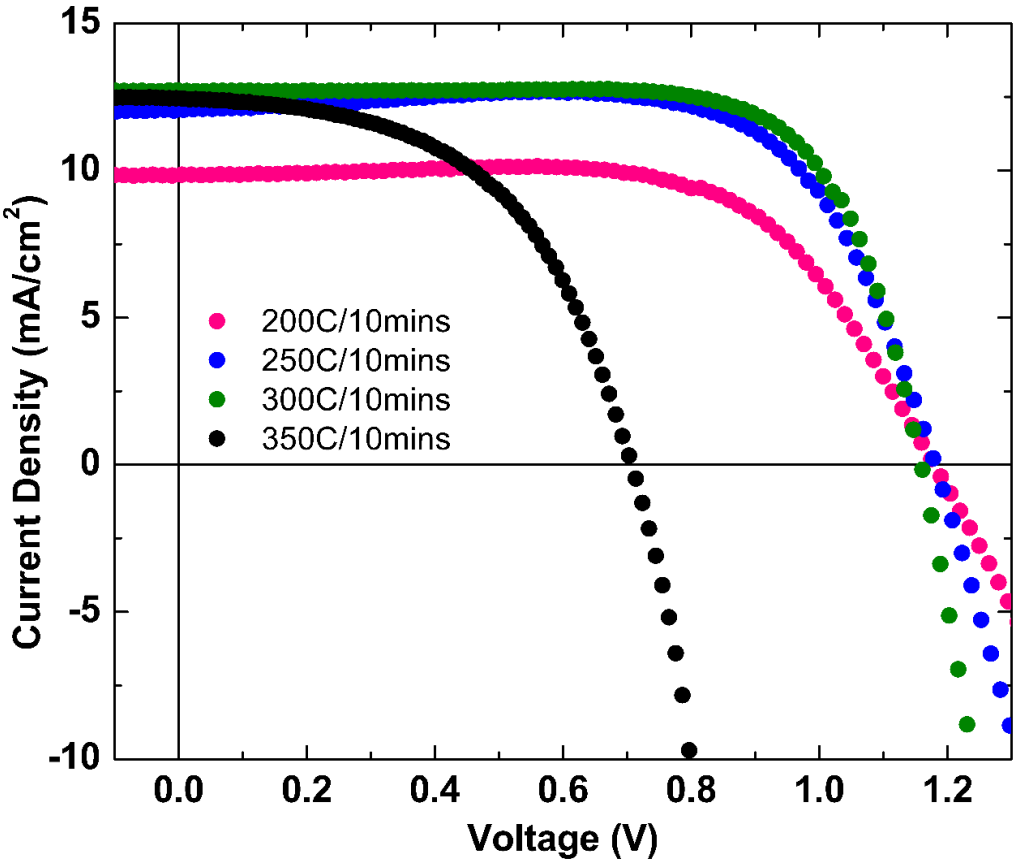

Figure 7.17: JV characteristics of devices with various anneal temperatures

Fig 7.18 shows the hysteresis behaviors of devices with the various anneal conditions. The reverse hysteresis of the devices with anneal temperatures below 300°C show significant hysteresis, with a hysteresis index of 59% for the 200°C devices. The reverse hysteresis reduces as we approach the optimum anneal temperature of 300°C with a much smaller index of 26%. Further, the devices annealed at 200°c and 250°C show a distinct hump in the JV curve, which is

illustrated by the inset in Fig 7.18. The large hysteresis and the humps in the JV curve are due to the poor intermixing of the precursor layers leading to more ionic movement from these unreacted precursor materials.

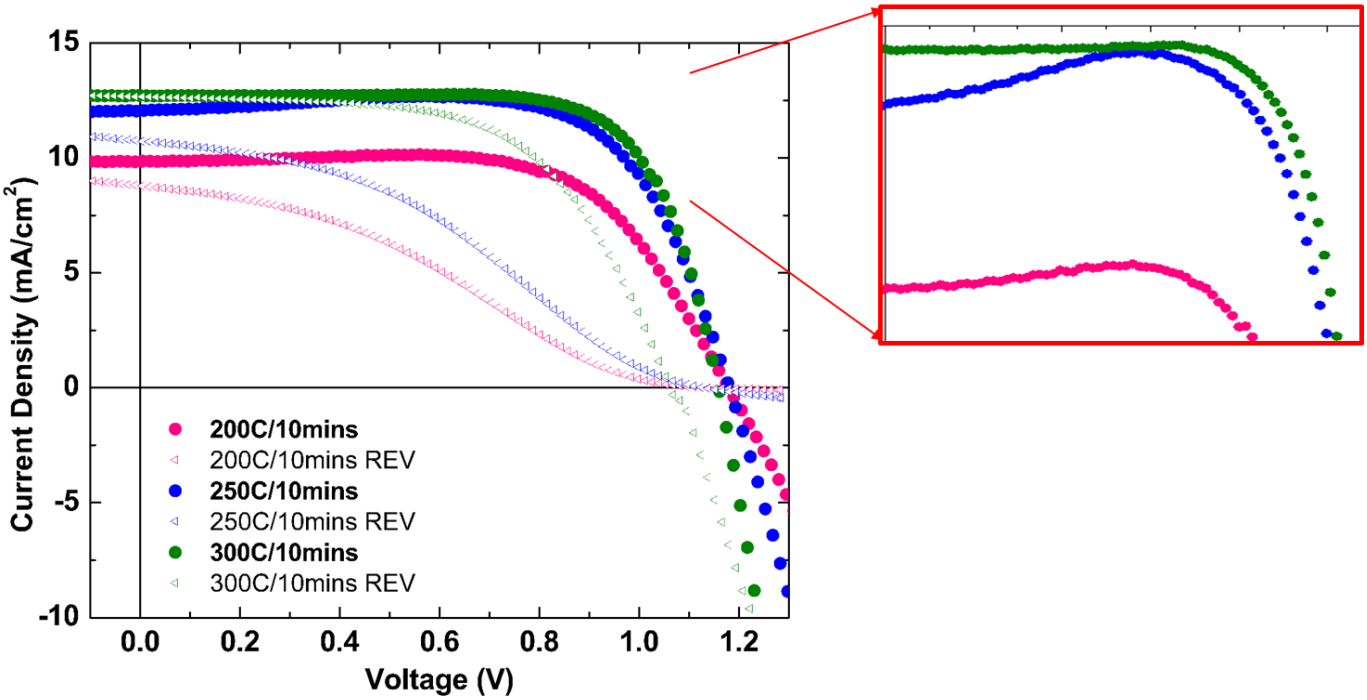

Anneal Condition	V_{OC} (V)	J_{SC} (mA/cm^2)	FF (%)	PCE (%)
200°C/10min	**1.18**	**9.9**	**67**	**7.74**
250°C/10min	**1.18**	**12.1**	**72**	**10.19**
300°C/10min	**1.16**	**12.7**	**73**	**10.76**
350°C/10min	**0.70**	**12.5**	**53**	**4.64**

Figure 7.18: JV curves showing the effect of anneal temperatures on device hysteresis. The inset shows the humps seen in the JV curve for anneals at 200°C and 250°C

To understand the worse device performance of the anneals at 350°C, we looked at the density of deep defects using the CfT technique. The density of deep defects for devices annealed at 350°C shows a marked increase compared to anneals at 300°C [Fig 7.19]. The density of deep defects for anneals at 300°C show a central mid gap state at 0.52eV below the conduction band with a peak density of $1x10^{16}/cm^3/eV$. The device annealed at 350°C shows a distribution of multiple mid gap states with densities in the range of $1.5x10^{16}/cm^3/eV$ and higher.

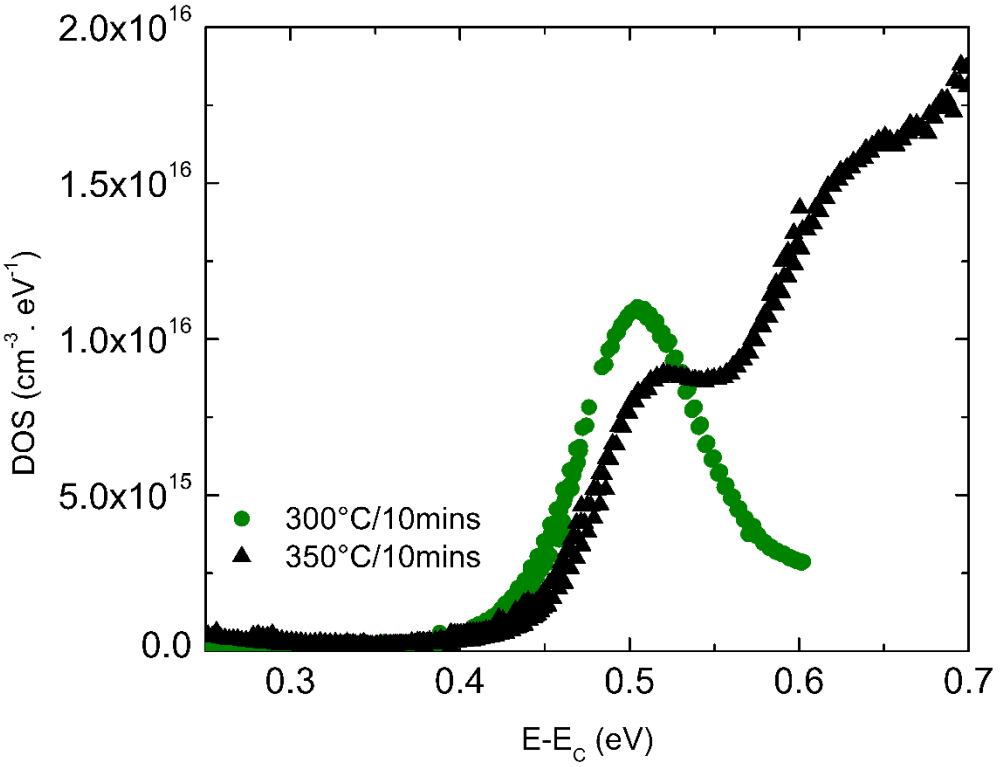

Figure 7.19: Density of deep defects for anneals at 300°C and 350°C. Anneals at 350°C show significantly more defects with a wider distribution

7.3.6 Substrate Temperature

During our previous work on $CsPbI_3$, we learned that substrate temperature plays a key role in device performance. We deposited the perovskite layer at elevated substrate temperatures

of 100°C and 200°C. Fig 7.20 shows the JV characteristics of these devices. We see that the devices deposited at higher substrate temperatures have a higher J_{SC} but also that their reverse hysteresis is much lower.

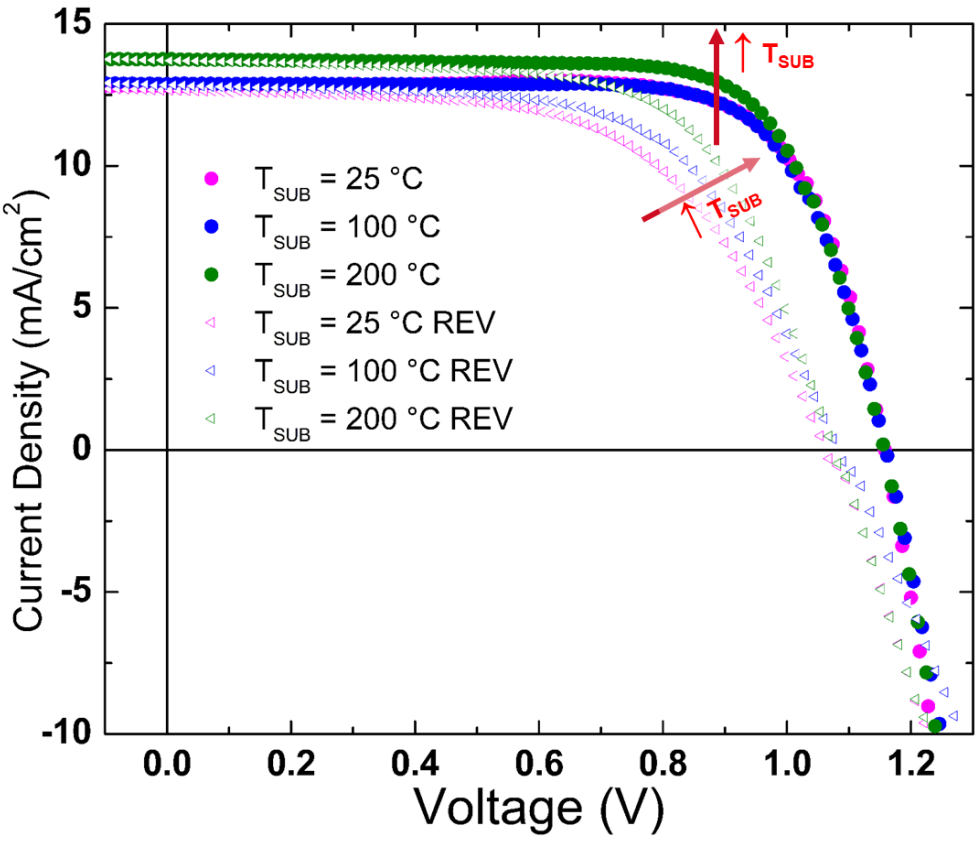

T_{SUB}	V_{OC} (V)	J_{SC} (mA/cm^2)	FF (%)	PCE (%)	Hysteresis Index
RT	**1.16**	**12.73**	**73**	**10.76**	**27**
100°C	**1.16**	**12.92**	**73**	**10.96**	**21**
200°C	**1.16**	**13.77**	**73**	**11.58**	**17**

Figure 7.20: JV characteristics of devices with perovskite layer grown at various substrate temperatures showing that higher substrate temperatures not only lead to higher J_{SC} but also lower hysteresis

The increase in J_{SC} is likely due to the lower density of mid gap states for the devices deposited at 200°C, as seen in Fig 7.21. While both the substrate conditions show devices with mid gap states at 0.52eV below the conduction band, devices deposited at 200°C show a much lower peak mid gap densities of $7x10^{15}/cm^3/eV$.

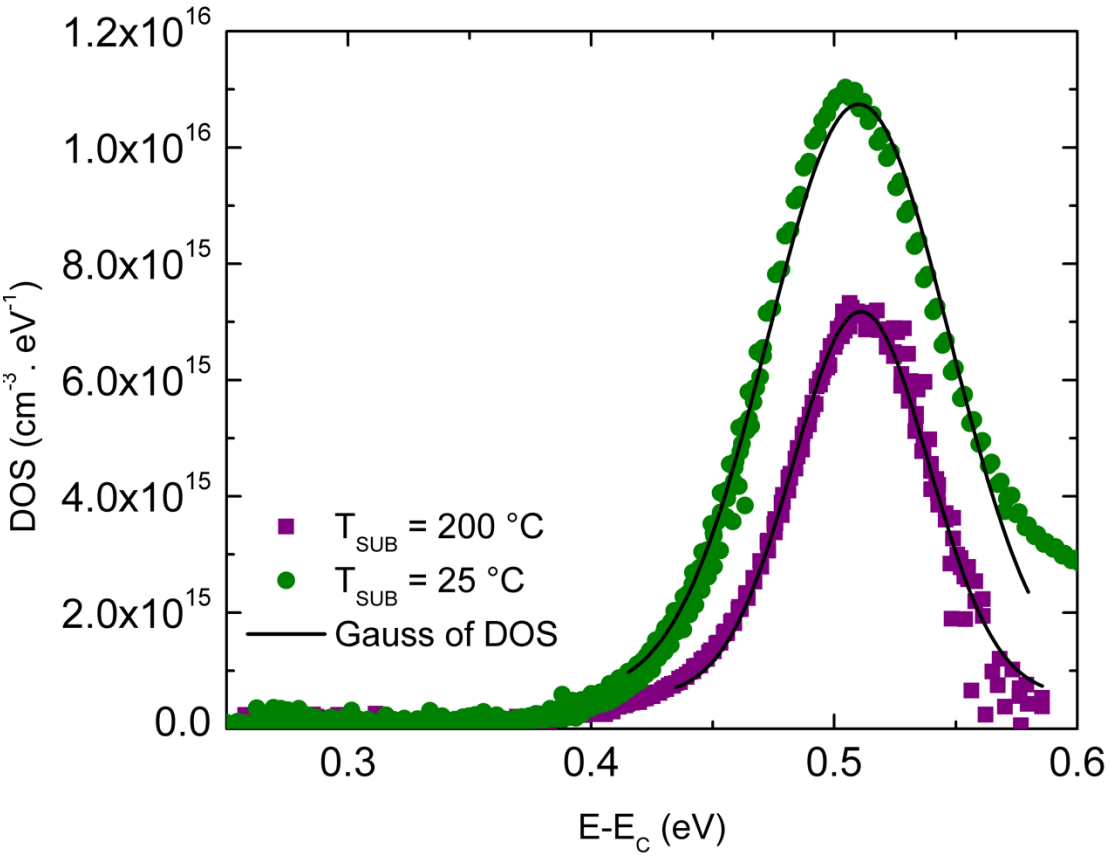

Figure 7.21: Density of deep defects for devices grown at 25°C and 200°C showing lower peak density of deep defects for 200°C

7.3.7 Champion Device

Through the above described process and device optimizations we have engineered our champion device with a J_{SC} of 13.77mA/cm2, V_{OC} of 1.16C, FF of 73%, and PCE of 11.58% [Fig 7.22]. Further, the hysteresis index of the device is low, at 17%

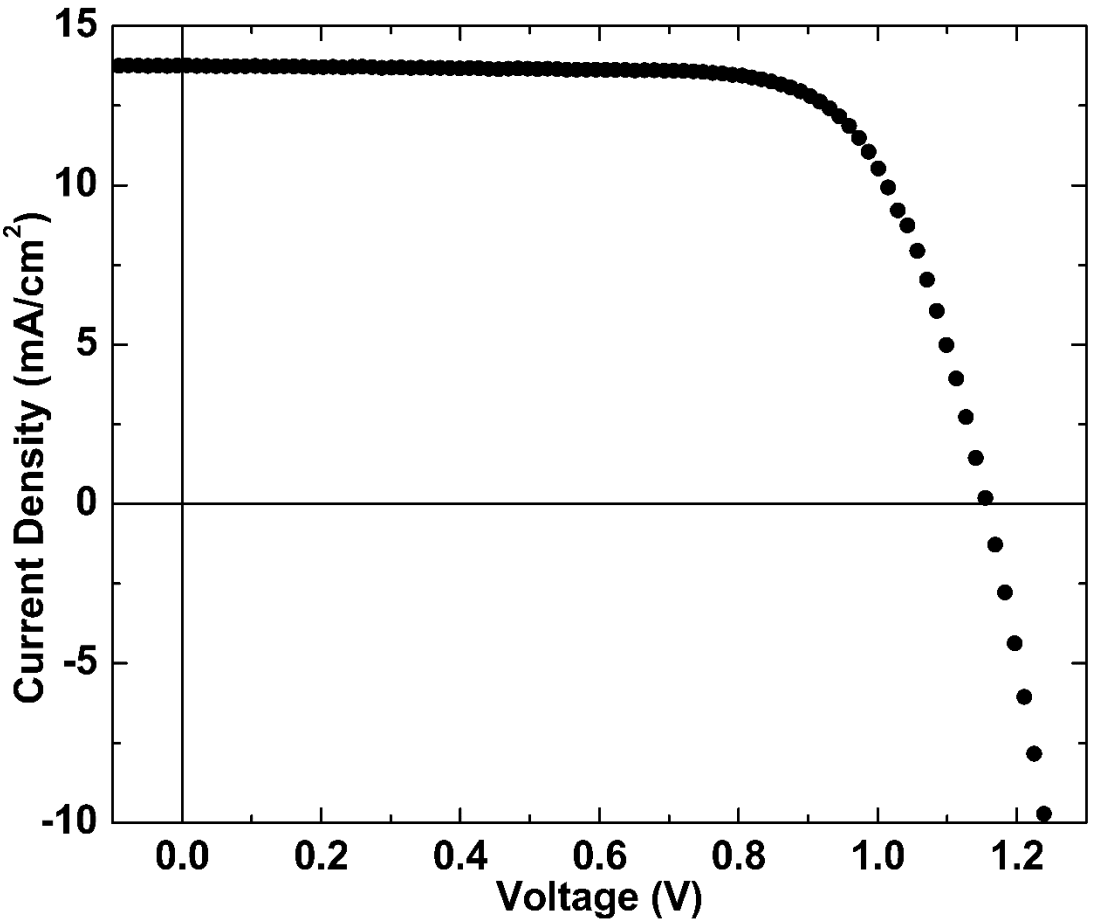

Figure 7.22: Champion $CsPbI_2Br$ device with J_{SC} of 13.77mA/cm2, V_{OC} of 1.16C, FF of 73%, and PCE of 11.58%

7.4 Thermal Stability

To understand the thermal stability of our fully inorganic mixed halide perovskite material, we grew perovskite films on a glass substrate and subjected them to a thermal stability test at 200°C for 24 hours in a nitrogen environment. We used X-Ray Diffraction analysis

(XRD) to understand the crystal structure of the perovskite films under thermal stress. Fig 7.23 shows the XRD analysis of these films before and after the thermal stability test. The peaks at 2-theta = 14.5° and 29°correspond to the (100) and (200) crystal planes of the α phase of the cubic perovskite structure. Most importantly, the XRD spectrogram shows no change in the crystal structure of the perovskite. Of particular interest is the area around 2-theta = 13° where we would expect to see a peak corresponding to PbI_2 if the perovskite film had undergone compositional degradation under the thermal stress. However, we see no such PbI_2 peak in the film after the thermal anneal. . Also, of note, is the fact that the perovskite does not undergo a phase transition from the α phase into the δ non-perovskite phase. Peaks corresponding to the δ non-perovskite phase would be visible at 2-theta = 10°, 18°,28°, and 36° if there was phase degradation of the perovskite material.

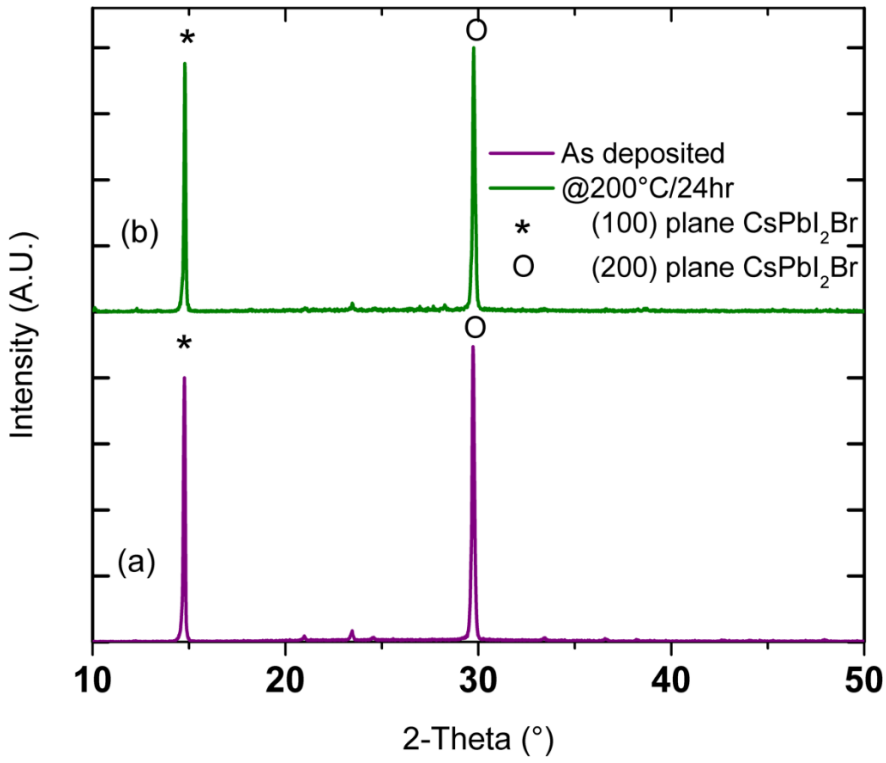

Figure 7.23: XRD analysis of perovskite films before and thermal stability test at 200°C showing no change in the crystal structure

We also subjected our photovoltaic devices with the FTO/In:CdS/pvkt/P3HT/Au structure to the thermal stability test by annealing the device at 200°C for 72 hours. We observed absolutely no change in the device performance as seen by the JV characteristics in Fig 7.24 and the EQE in Fig 7.25. This is critical proof that the perovskite material and the device as a whole are stable at elevated temperatures for an extended period of time. As far as we know, this is the first such result of the thermal stability of perovskite stability over extended periods of time.

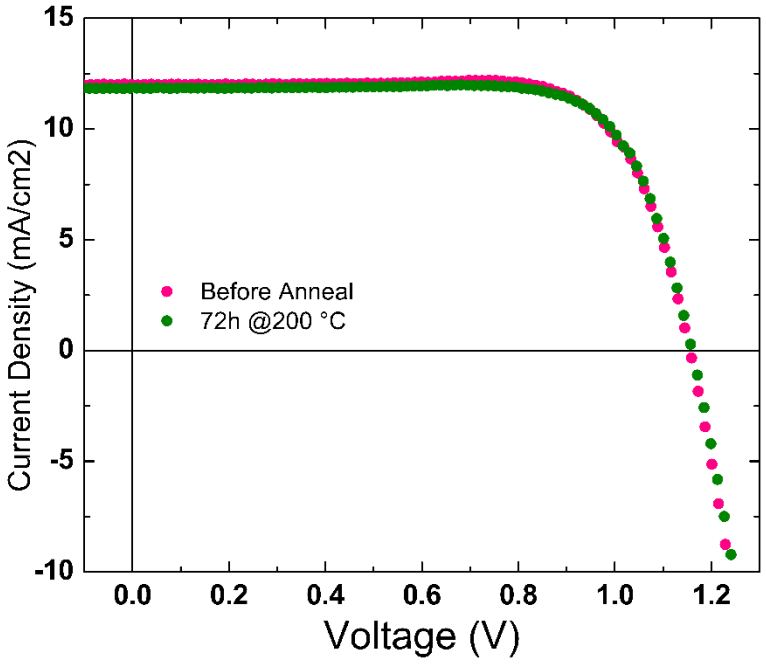

Figure 7.24: JV characteristics of device before and after thermal stability test showing no change in performance

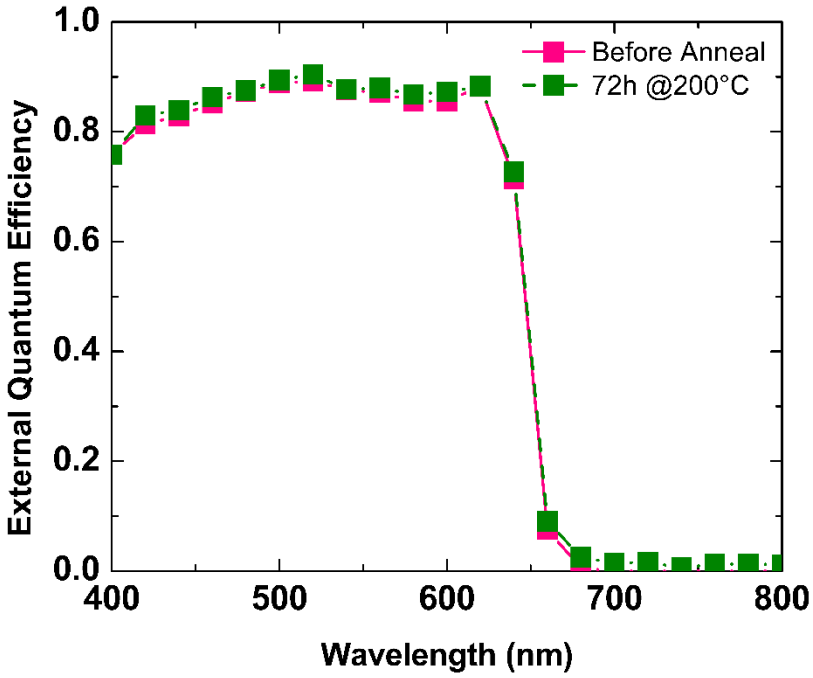

Figure 7.25: EQE of device before and after thermal stability test showing no change in device performance

7.5 Device Characterization

7.5.1 External Quantum Efficiency and Tauc Plot

The EQE of our champion device is shown in Fig 7.26, displaying a flat EQE with most wavelengths of light below the band gap being collected with greater than 80% efficiency. The EQE falls off at 680nm, corresponding to the band gap of the $CsPbI_2Br$ material. The Tauc plot [Fig 7.27] of the material where we plot the $(EQE^* h\vartheta)^2$ vs $h\vartheta$ in the area where the EQE falls off sharply shows an energy band gap of 1.87eV.

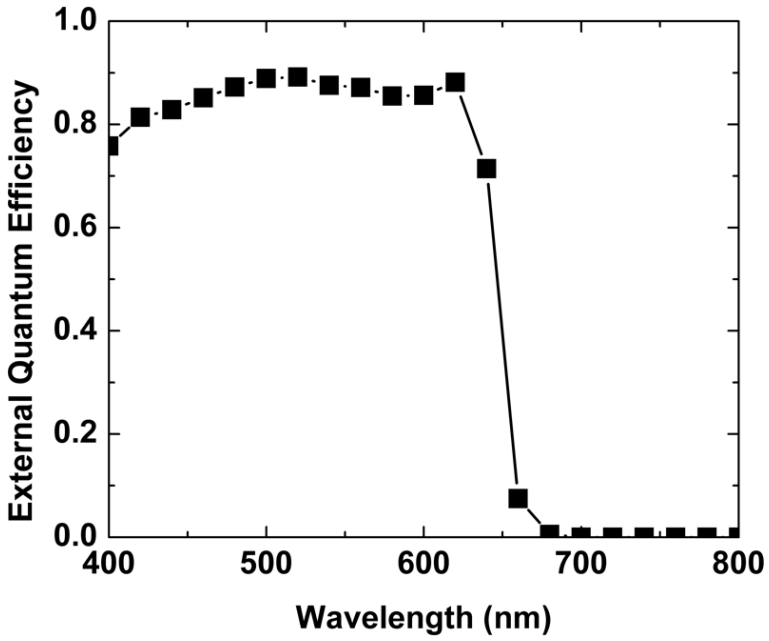

Figure 7.26: EQE of champion device

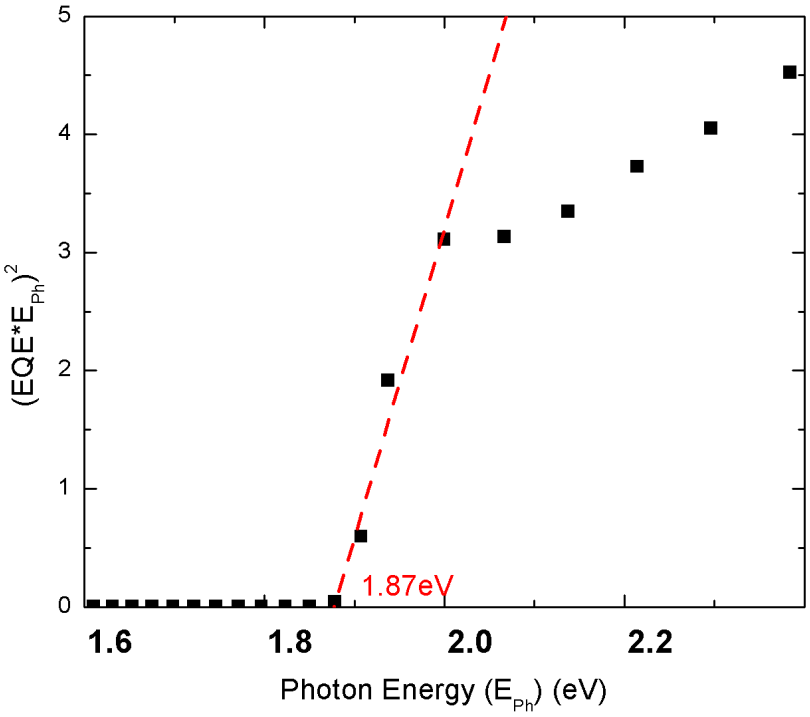

Figure 7.27: Tauc plot showing a band gap of 1.87eV

7.5.2 Urbach Energy

Past the band gap of the absorber material the EQE of the device falls exponentially. The sub-band gap absorption in this region is due to the presence of tail states resulting from the crystal disorder in the perovskite layer. The Urbach energy, which is a measure of the tail state distribution and thus the crystal disorder, can be measured by plotting the sub-band gap QE as function of photon energies. Urbach energies of 0.2 -0.5meV are common for perovskites depending on their growth conditions. The sub band gap QE [Fig 7.28] of the $CsPbI_2Br$ devices show an Urbach energy of 21meV, indicating the high quality of the material grown.

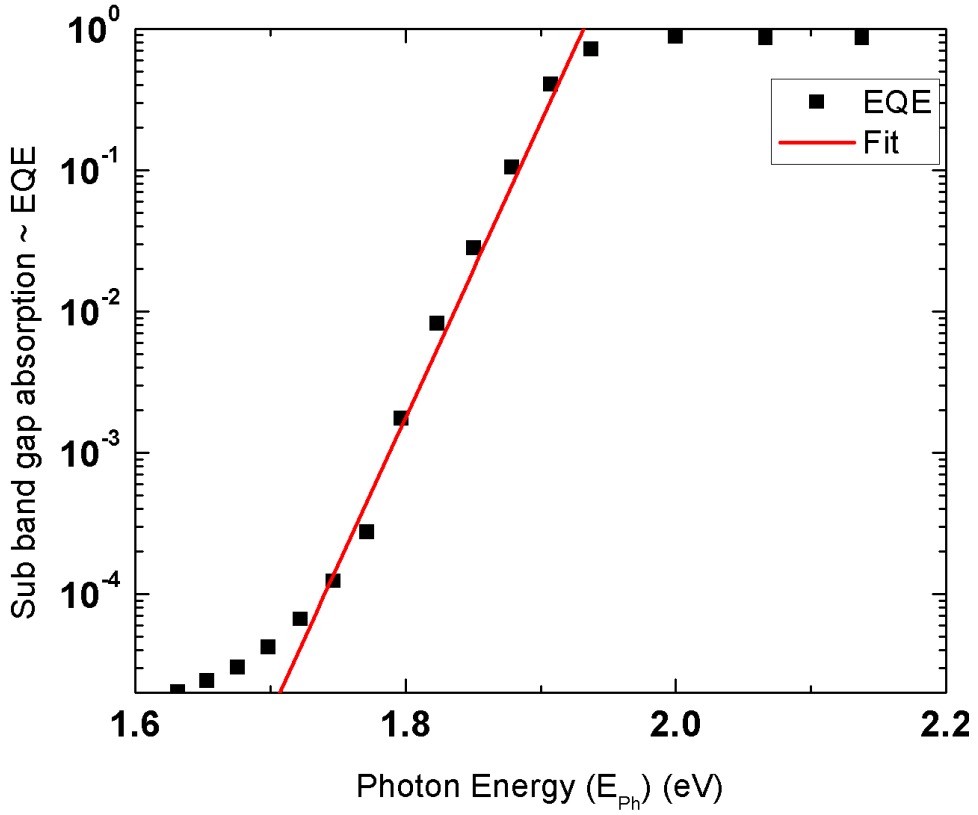

Figure 7.28: sub-band gap absorption vs photon energy showing a Urbach energy of 21meV

7.5.3 Density of Deep Defects

The density of deep defects for our champion device shows a central mid gap defect at 0.52eV below the conduction band. The defect densities form a Gaussian distribution centered at this defect with a peak defect density of $7x10^{15}/cm^3/eV$ [Fig 7.29].

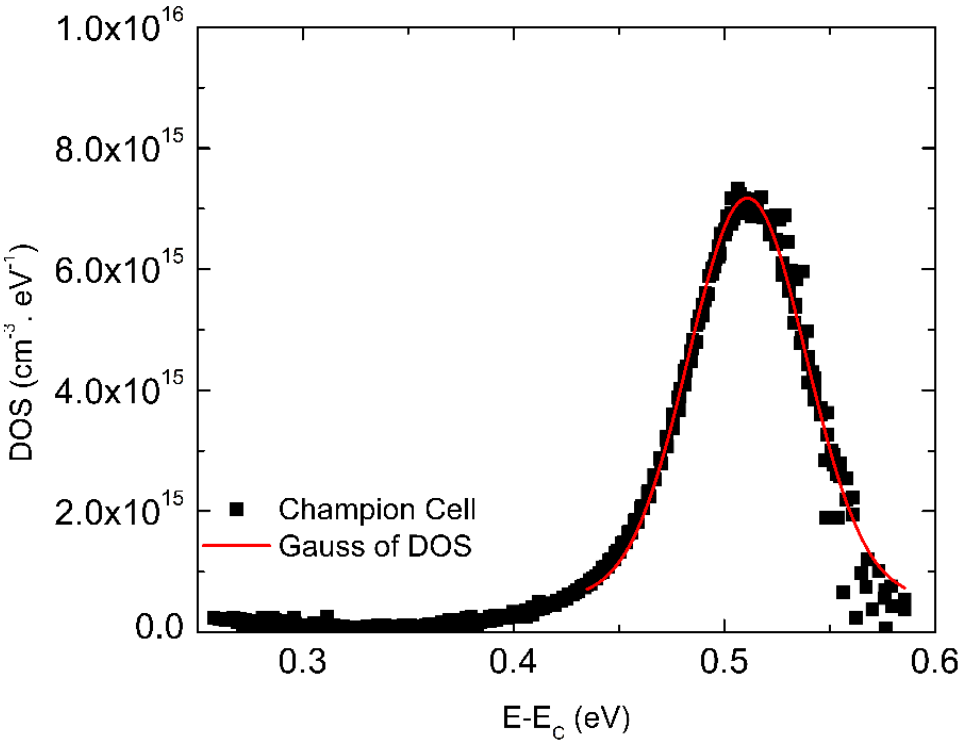

Figure 7.29: Density of deep defects showing a Gaussian distribution of deep defects centered at 0.53eV below the conduction band with a peak density of $7x10^{15}/cm^3/eV$

Capacitance-frequency-Temperature measurements [8-10], where the capacitance is measured as a function of frequency at various temperatures as described in Section 2.8, is used to determine the attempt-to-escape-frequency and the activation energy of the traps. The capacitance-frequency sweeps at multiple temperatures are shown in Fig 7.30. The corresponding plots of $-f\frac{dC}{df}$ vs f and $\ln\frac{f_{peak}}{T^2}$ vs $\frac{1}{kT}$ are shown in Fig 7.31 and 7.32 respectively.

From the linear fit of $\ln\frac{f_{peak}}{T^2}$ vs $\frac{1}{kT}$ we calculate the activation energy of the mid gap trap to be 0.54eV, which conforms with our earlier calculation. The attempt-to-escape-frequency is calculated to be $3x10^{-9}$Hz.

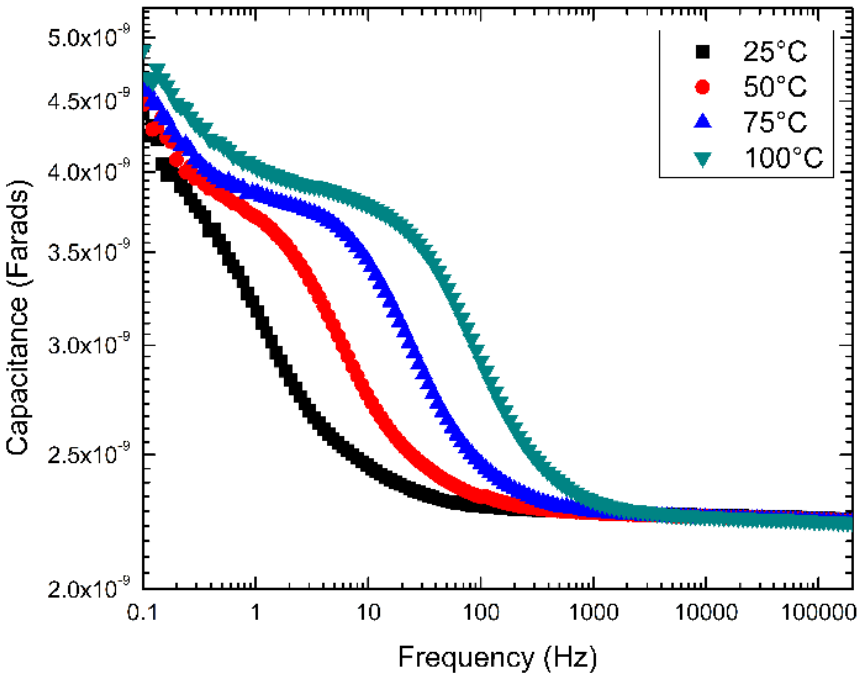

Figure 7.30: Raw capacitance- frequency data measured at multiple temperatures

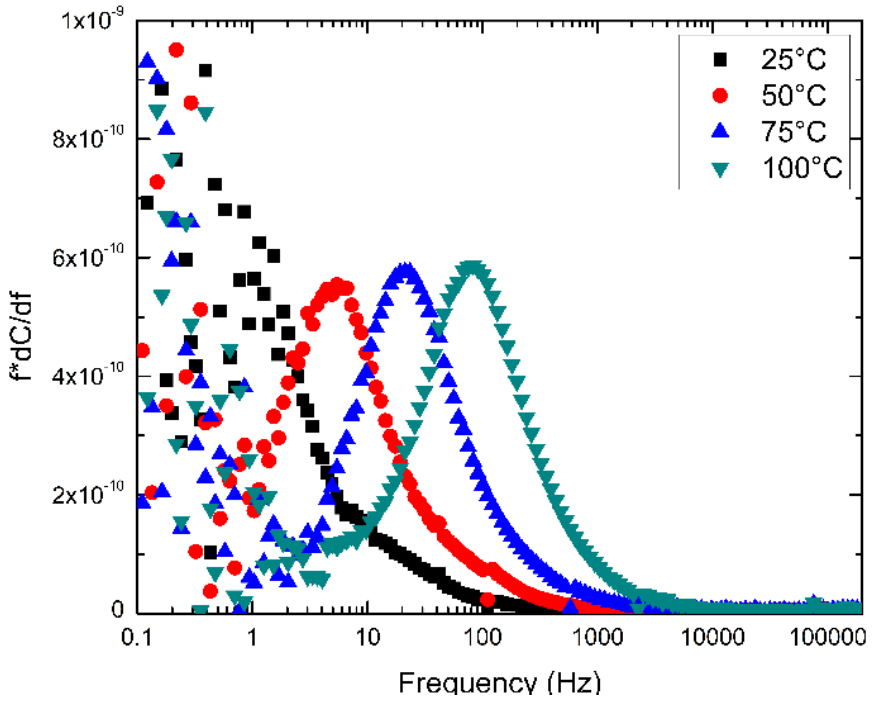

Figure 7.31: -fdC/df versus frequency from the raw capacitance-frequency data

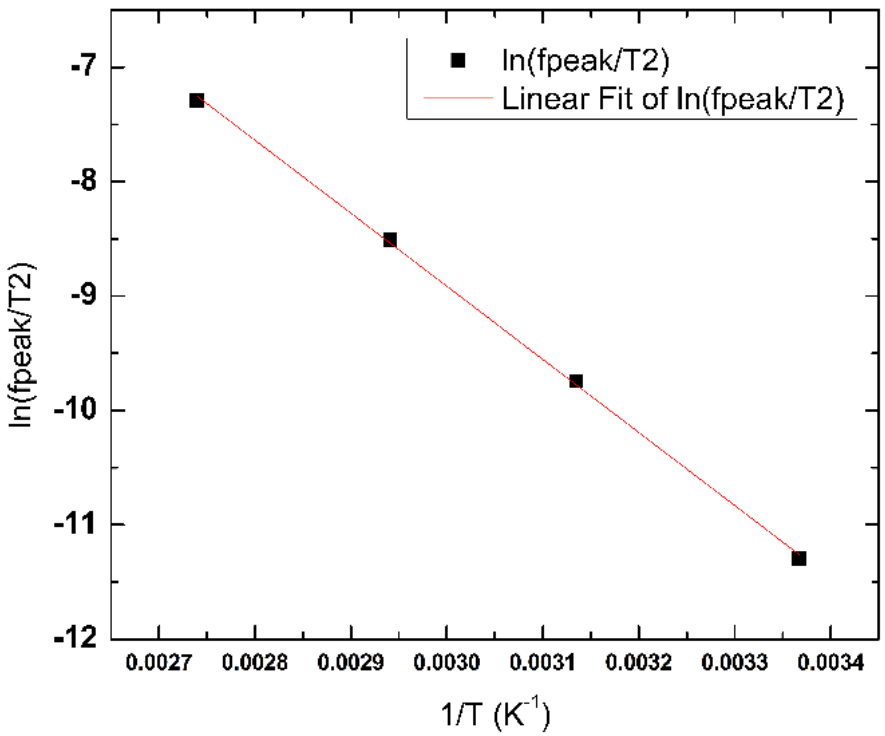

Figure 7.32: Linear fit of $\ln\frac{f_{peak}}{T^2}$ vs $\frac{1}{kT}$ used to calculate activation energy of traps and ATEF

7.5.4 Calculation of Dielectric Constant

The exciton binding energy is dependent on the dielectric constant of the material. To ensure that the photogenerated charge carriers are unbound, the exciton binding energy should be lower than the thermal energy. The dielectric constant is calculated using by modelling the capacitance of the perovskite solar cells as a function of the thickness of the active perovskite layer. The total capacitance (C_{TOTAL}) of the device can be modeled as a simple series capacitance of the transport layers and the perovskite layer [10]. It is given by,

$$\frac{1}{C_{TOTAL}} = \frac{1}{C_{TL}} + \frac{1}{C_{PVKT}}$$

where C_{TL} and C_{PVKT} are the capacitances of the transport layers and the perovskite layer respectively. The capacitance of the perovskite layer is given by,

$$\frac{1}{C_{PVKT}} = \frac{t}{A * \in_0 * \in_r}$$

where t is the thickness of the perovskite layer, A is the active area of the device, and $\in_0$, $\in_r$ are the absolute permittivity of vacuum and the dielectric constant of the perovskite material respectively.

By measuring the capacitance of devices fabricated with multiple different perovskite layer thickness [Fig 7.33] with the same transport layers, we can extract the dielectric constant of the perovskite material using the model. Fig 7.34 shows the fits of several different dielectric constants to the plot of total device capacitances vs perovskite layer thickness. Using this method, we obtain the dielectric constant of the $CsPbI_2Br$ to be ~28. This gives us an excitonic binding energy of ~2meV, which is considerably lower than the thermal energy at room temperature.

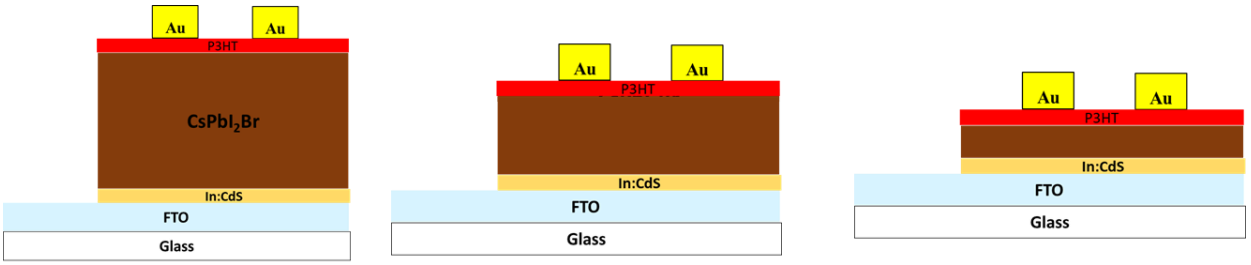

Figure 7.33: devices with multiple different thicknesses of the perovskite layer used to model dielectric constant

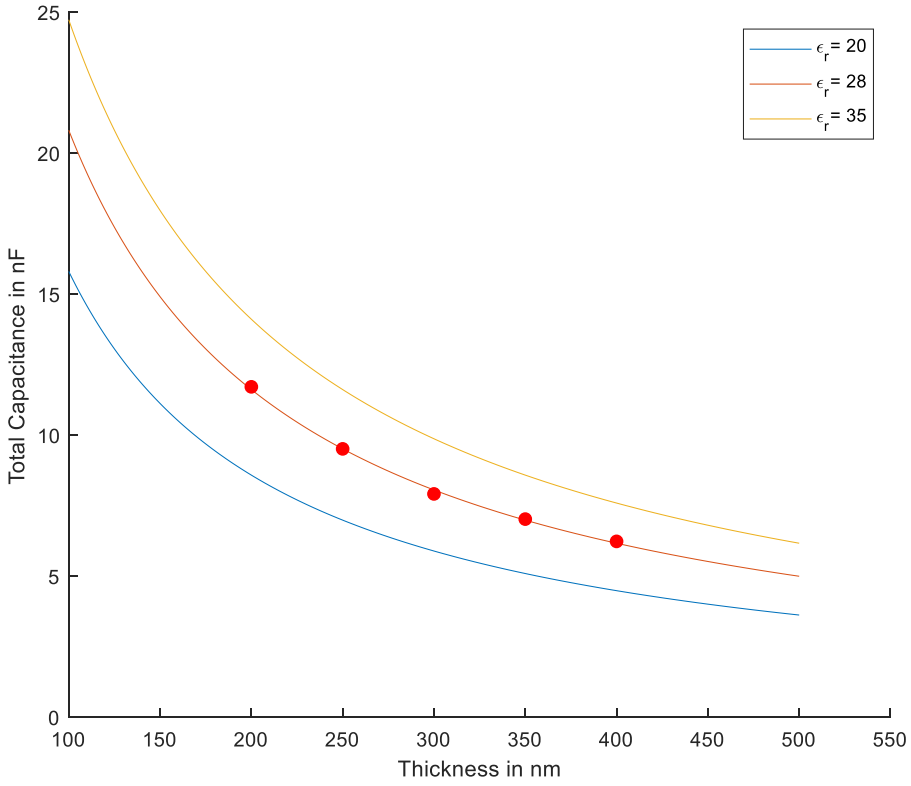

Figure 7.34: Various different dielectric constants fit capacitance of devices with various perovskite layer thicknesses. Best fit for dielectric constant of 28

References

1. John W. Anthony, Richard A. Bideaux, Kenneth W. Bladh, Monte C. Nichols, *Handbook of Mineralogy*, Mineralogical Society of America.

2. M. A. Peña, J. L. Fierro, "Chemical structures and performance of perovskite oxides", Chemical Reviews. 101 (7): 1981–2017. doi:10.1021/cr980129f. PMID 11710238

3. Zarick, Holly F., Naiya Soetan, William R. Erwin, and Rizia Bardhan. "Mixed Halide Hybrid Perovskites: A Paradigm Shift in Photovoltaics." *Journal of Materials Chemistry A* 6, no. 14 (2018): 5507–37. https://doi.org/10.1039/c7ta09122b.

4. Wang, Xi, Yichuan Ling, Xiujun Lian, Yan Xin, Kamal B. Dhungana, Fernando Perez-Orive, Javon Knox, et al. "Suppressed Phase Separation of Mixed-Halide Perovskites Confined in Endotaxial Matrices." *Nature Communications* 10, no. 1 (February 11, 2019). https://doi.org/10.1038/s41467-019-08610-6.

5. Hoke, Eric T., Daniel J. Slotcavage, Emma R. Dohner, Andrea R. Bowring, Hemamala I. Karunadasa, and Michael D. McGehee. "Reversible Photo-Induced Trap Formation in Mixed-Halide Hybrid Perovskites for Photovoltaics." *Chemical Science* 6, no. 1 (2015): 613–17. https://doi.org/10.1039/c4sc03141e.

6. "CsPbBr3 Perovskite Powder, a Robust and Mass-Producible Single-Source Precursor: Synthesis, Characterization, and Optoelectronic Applications." ACS Omega, 2019. https://pubs.acs.org/doi/10.1021/acsomega.9b00385.

7. Zheng, Chao, Chenghao Bi, Fan Huang, David Binks, and Jianjun Tian. "Stable and Strong Emission CsPbBr3 Quantum Dots by Surface Engineering for High-Performance Optoelectronic Films." *ACS Applied Materials & Interfaces* 11, no. 28 (June 25, 2019): 25410–16. https://doi.org/10.1021/acsami.9b07818.

8. Pranav Joshi, Ph.D. dissertation, "Understanding the photostability of perovskite solar cell", Iowa State University (2016)

9. Liang Zhang, Ph.D. dissertation, "Device physics of perovskite solar cells", Iowa State University (2016)

10. S M Istiaque Hossain, Ph.D. dissertation, “Device physics of perovskite solar cells”, Iowa State University (2018)

CHAPTER 8. CONCLUSION

In this report, we sought to understand and resolve the fundamental problem of thermal instability of perovskite materials. In short, we have been successful in this venture. We have optimized and fabricated fully inorganic perovskite devices with a PCE of 11.62%, which show no thermal degradation at 200°C for over 72 hours. The significant findings and steps involved in this process are detailed below:

- We replaced the primary source of thermal instability in hybrid organic-inorganic perovskites, the organic cation (methylammonium, formamidium etc.), with an inorganic cation Cesium.
- We have developed a sequential layer-by-layer vapor deposition technique to deposit perovskite layers with nanometer level accuracy.
- We have used the fully inorganic cesium lead iodide perovskites, $CsPbI_3$, as the active absorber layer to fabricate p-i-n architecture devices with PTAA and PCBM as the transport layers.
- We have enahnced the photoconversion efficiency of $CsPbI_3$ solar cells through careful experimentation and optimization of the tranport layers, perovskite stoichiometry, anneal conditions, total layer thickness, and substrate temperature during growth. We have achieved a PCE of 11.2% for $CsPbI_3$ solar cells, which represents the highest such reported efficiency with an inverted p-i-n structure.
- We have used capacitance spectroscopy studies to show that the sum of dopant and shallow defects for $CsPbI_3$ solar is in the $2x10^{15}/cm^3$ range.

- We have determined the energy band gap of our vapor deposited $CsPbI_3$ to be 1.74eV.
- Due to the thermodynamic instability of $CsPbI_3$ at room temperatures, attributed to its small Goldschmidt Tolerance Factor, we have employed the strategy of partial substitution of iodine with bromine to fabricate a mixed halide perovskite composition.
- We have fabricated highly efficiecnt photovoltaic devices with a n-i-p device architecture using $CsPbI_2Br$, employing various characterization tehcniques such as external quantum efficiency and capcitance spectroscopy to troubleshoot problems and understand the loss mechanisms in the photovoltaic device.
- We have shown that anneal temperatures and substrate temperatures during growth play a critical role in the complete formation of the perovskite materrial. Optimum anneal conditions and substrate temperatures ensured there was complete intermixing of the precursor materials. Smaller hysteresis of the JV curves were observed for higher substrate temperatures.
- We have fabricated a champion device with $CsPbI_2Br$ as the active layer to achieve a PCE of 11.6%, with a high V_{OC} of 1.16V and a small hysteresis index of 16%.
- We have shown, through XRD analysis, the thermal stablity of the perovskite compositon, displaying no compositional or phase degradation at 200°C over extended periods of time.

- Thermal stability tests on our n-i-p devices with $CsPbI_2Br$ with the structure FTO/In:CdS/pvkt/P3HT/Au show no reduction in the device performance at 200°C over 72 hours.
- We have determined the energy band gap of the $CsPbI_2Br$ material to be 1.87eV, which makes it a suitable candidate for tandem cells with c-Si or CIGS.
- We have shown that the vapor deposited $CsPbI_2Br$ material grown posseses a low defect density of mid gap states with a single trap state 0.52eV below the conduction band with a peak density of $7x10^{15}/cm^3/eV$.
- We have also shown the low crystal disorder in the peroivskites grown with our vapor depostion technique that have Urbach energies of 21meV, which is the lower range for perovskite materials.
- We have used capacitance spectroscopy techniques to determine the dielctric constant of $CsPbI_2Br$ to be 28.